Improving Climate Projections Through the

Assessment of Model Uncertainty and Bias in the

Global Water Cycle

by

Noel C. Baker

A Dissertation Presented in Partial Fulfillment
of the Requirements for the Degree
Doctor of Philosophy

Approved July 2013 by the
Graduate Supervisory Committee:

Huei-Ping Huang, Chair
James Anderson
Amanda Clarke
Steven Trimble
Ronald Calhoun

ARIZONA STATE UNIVERSITY

August 2013

ABSTRACT

The implications of a changing climate have a profound impact on human life, society, and policy making. The need for accurate climate prediction becomes increasingly important as we better understand these implications. Currently, the most widely used climate prediction relies on the synthesis of climate model simulations organized by the Coupled Model Intercomparison Project (CMIP); these simulations are ensemble-averaged to construct projections for the 21st century climate. However, a significant degree of bias and variability in the model simulations for the 20th century climate is well-known at both global and regional scales. Based on that insight, this study provides an alternative approach for constructing climate projections that incorporates knowledge of model bias. This approach is demonstrated to be a viable alternative which can be easily implemented by water resource managers for potentially more accurate projections. Tests of the new approach are provided on a global scale with an emphasis on semiarid regional studies for their particular vulnerability to water resource changes, using both the former CMIP Phase 3 (CMIP3) and current Phase 5 (CMIP5) model archives. This investigation is accompanied by a detailed analysis of the dynamical processes and water budget to understand the behaviors and sources of model biases. Sensitivity studies of selected CMIP5 models are also performed with an atmospheric component model by testing the relationship between climate change forcings and model simulated response. The information derived from each study is used to determine the progressive quality of coupled climate models in simulating the global water cycle by rigorously investigating sources of model bias related to the moisture budget. As such,

the conclusions of this project are highly relevant to model development and potentially

may be used to further improve climate projections.

ACKNOWLEDGMENTS

TABLE OF CONTENTS

LIST OF TABLES

LIST OF FIGURES

CHAPTER 1

INTRODUCTION

Evidence of recent changes in the climate system and concerns regarding subsequent effects on human society have led to concerted efforts to understand the sources of change and predict future conditions. Observed increasingly frequent occurrences of extreme hydrological events such as flooding and droughts (Solomon et al. 2007, sec. 3.8) and the security of the water supply are matters of critical importance to human life, making an understanding of the influence of climate change on precipitation and the hydrological cycle an urgent goal. The need to predict and quantify such change has led to the organization of numerous research institutions throughout the world with the same objective: to develop models which can be used to simulate and forecast climate processes. Information produced by these climate models now forms the basis of our predictions of the future.

The fundamental issue of climate science is the fact that we only have one global system for reference; we cannot replicate this system or perform experiments on the system as a whole. Until the development of climate models, our methods for numerical weather prediction and long-term climate approximations had been exclusively based on little more than a century of firsthand observations and several thousand years of limited proxy data for a small number of variables. Now we have built complex, process-based models of the climate system with which we can test a hypothesis on a global scale. These models serve as artificial laboratories for examining climate dynamics, the sensitivity of the system to perturbations, and individual small and large-scale phenomena. The models have basic limitations, however; they are constrained by the

technological capabilities of the computers which run the simulations, compromising the model's space-time detail and the length of time over which the simulation can be run. As such, the models are defined as "quasi-realistic" in the sense that the governing processes cannot be fully described within the model. These models are able to reproduce many of the physical processes of climate; however, due to their inherent technical limitations, models contain unavoidable sources of bias.

A climate model is a mathematical representation of the interactions between and within the ocean, land, sea ice, and atmosphere. How each of these components is defined and coupled to the other components is particular to each model. The types of models can range from very simple, such as a single-point Earth system used to average the incoming and outgoing solar radiation, to the more complex fully-coupled ocean-atmosphere models which discretize and solve the full equations for energy, momentum, and mass transfer. In order to test quality, the model is used to simulate past climate conditions. The results are then compared with recorded observational data. Global climate models show a significant and increasingly accurate ability to recreate many large-scale climate features such as the distribution of land and sea surface temperatures, precipitation coverage and intensity, and sea ice cover (Meehl et al. 2007, Taylor et al. 2012). The models are continually being refined and improved with the intention of producing more accurate projections of possible future conditions of a changing climate.

The overarching goal of the project described herein is to provide a valuable contribution to the model refinement process. From a broad perspective, the project incorporates several stages of analysis, with each stage examining specific sources of model bias associated with the simulation of precipitation. Chapters 2 and 3 provide the

scientific background and motivation for the project with relevant information leading to the formulated solutions in the subsequent chapters. Chapter 4 introduces an alternative method for constructing ensemble averaged climate projections of precipitation; Chapter 5 details the further application of this alternate method to additional hydrological variables in the updated CMIP5 archive. Chapter 6 contains an extensive comparison of the seasonal and regional water budget quality between the CMIP3 and CMIP5 archives for selected quantities. Chapter 7 presents the rigorous analysis of the detailed global water budget and contrasts skill of selected CMIP5 models in reproducing associated quantities, and Chapter 8 provides sensitivity studies with the NCAR CAM 3.1 atmospheric model to quantify precipitation response to climate change using CMIP5 simulated data. Each study uncovers particular issues in model ability to generate precipitation and provides a pertinent starting point for the formulation of solutions these issues. The overall analysis employs rigorous methods for better evaluating and utilizing climate models for long-term prediction, potentially leading to improvements of IPCC-type climate projection. Such improvements are valuable not only to climate research but also to policy making and all facets of the society that are directly affected by the implications of a changing climate.

CHAPTER 2

BACKGROUND

2.1   The hydrological cycle

The hydrological cycle, also known as the water cycle, is a conceptual model describing the continuum of water movement along various pathways on the Earth. Water plays a crucial role both in regulating global weather and in providing for societal needs. Solar radiation serves as the driving force for the hydrological cycle, evaporating water from the oceans and land surfaces (Holton 2004). Wind advects the water vapor through the atmosphere until it condenses into clouds and precipitation, which falls back onto the land and ocean (Fig. 2.1). This water vapor is the dominant greenhouse gas in the atmosphere and, like other greenhouse gases, is responsible for the feedback of warming in the climate system (Solomon et al. 2007, Ch.1). As the warming of the atmosphere increases, the capacity for air to hold water vapor also increases (governed by the Clausius-Clapyron relation). This process further intensifies the concentration of atmospheric water vapor which in turn generates moisture convergence in clouds and increases the intensity of precipitation in storms (e.g. Held and Soden 2006). However, total precipitation is controlled by the available energy in the atmosphere, namely the ability of the troposphere to radiate latent heat released by precipitation. An enhanced water cycle is shown to produce a positive trend of increased precipitation in the high latitudes which is balanced by a negative trend of net precipitation in the subtropics (Wu et al. 2005), leading to increased occurrences of droughts in these regions. Understanding the feedback of warming and its effects on the climate system is crucial for water
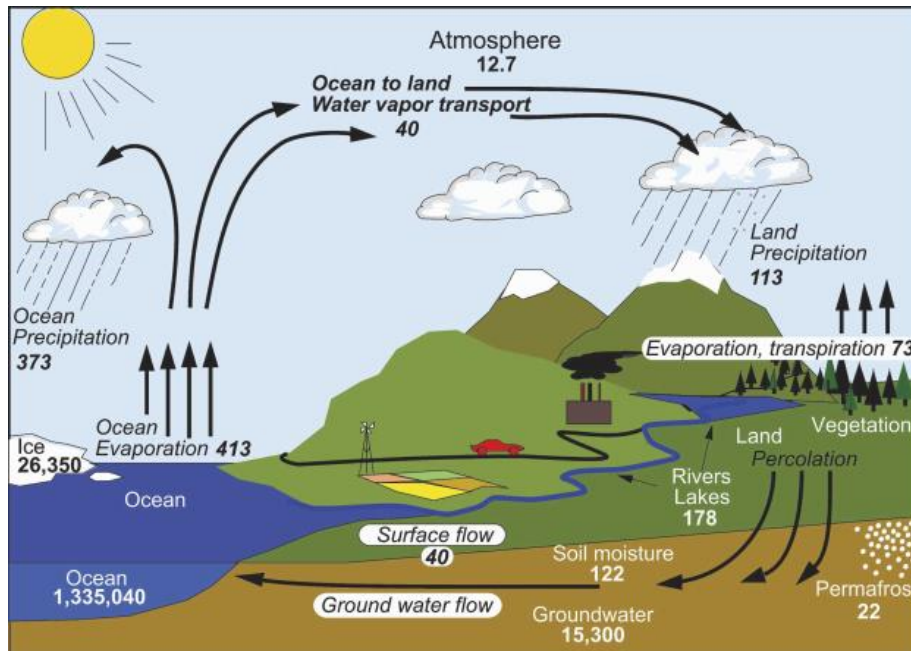
Fig. 2.1 The hydrological cycle estimates of storage values for the main water reservoirs (103 km3) and the flow of moisture between the reservoirs (italicized, 103 km3/year) (Trenberth et al. 2007).

resource management, especially for regions which are particularly vulnerable to drought, such as Arizona.

Recent efforts have been made (especially rigorous in the last two decades) to understand and quantify the various physical, thermodynamic, and moisture processes of the hydrological cycle through each realm of the Earth system (e.g. Solomon et al. 2007). This chapter will introduce the fundamental principles and tools which climate scientists utilize to provide our most current knowledge of the present and future climate.

2.2   Observational data sets

Our understanding of the complex system of climate begins with the examination of its physical, chemical, and dynamical structure based on a combination of *in situ* observations and, in the last several decades, a growing number of new technologies. A

network of land-based surface meteorological stations combined with upper-air rawinsonde soundings and aircraft readings provides atmospheric measurements of pressure, temperature, specific humidity, and precipitation (Reynolds 2000). Ocean observations are taken by commercial ships and research vessels which provide both atmospheric and ocean measurements (sea surface temperature, salinity) as well as subsurface measurements (concentrations of CO_2 and other chemicals) (Diamond and Lief 2009). As a supplement to the *in situ* observations, certain climate data may also be measured by an array of new technologies such as satellites, remote sensing, LIDAR, laser, and acoustics.

The use of satellites in meteorological measurements has expanded greatly in the last 50 years, and we are now able to measure a broad spectrum of incoming and outgoing radiation fluxes to further our understanding of the present state of the climate system (Wallace and Hobbs 2006). Geosynchronous orbiters, among other types of satellites, provide daily global coverage with information supplying measurements of the visible spectrum (cloud cover), infrared radiation (temperature), and additional wavelengths which can detect water vapor profiles (humidity).

Certain limitations exist in our ability to gather observational data. Ocean current velocities are very difficult to measure from ships; this issue severely limits our present knowledge of the dynamical structure of oceans. Furthermore, one of the most significant obstacles in understanding oceanic heat storage and its effects on long-term climate change stems from our inability to monitor the temporal variability in subsurface ocean temperature (Trenberth et al. 2002). In addition to the limited subsurface ocean measurements, a significant lack of upper air data exists over certain regions such as the

6

southern oceans. Fig. 2.2 depicts the incomplete global distribution of land-based stations and ocean surface ship reports. Satellite observations can be used to fill in the gaps both spatially and temporally. Global coverage is achieved by converting the information provided by the various datasets into a standard three-dimensional grid. This conversion is performed through interpolation or extrapolation techniques or by using alternative methods based on numerical weather prediction models (Kalnay et al. 1996, Xie and Arkin 1997, Adler et al. 2003). Several examples of datasets which incorporate these methods are described in the following sections; these datasets are utilized in all references to, or analyses involving, observational data within this project.
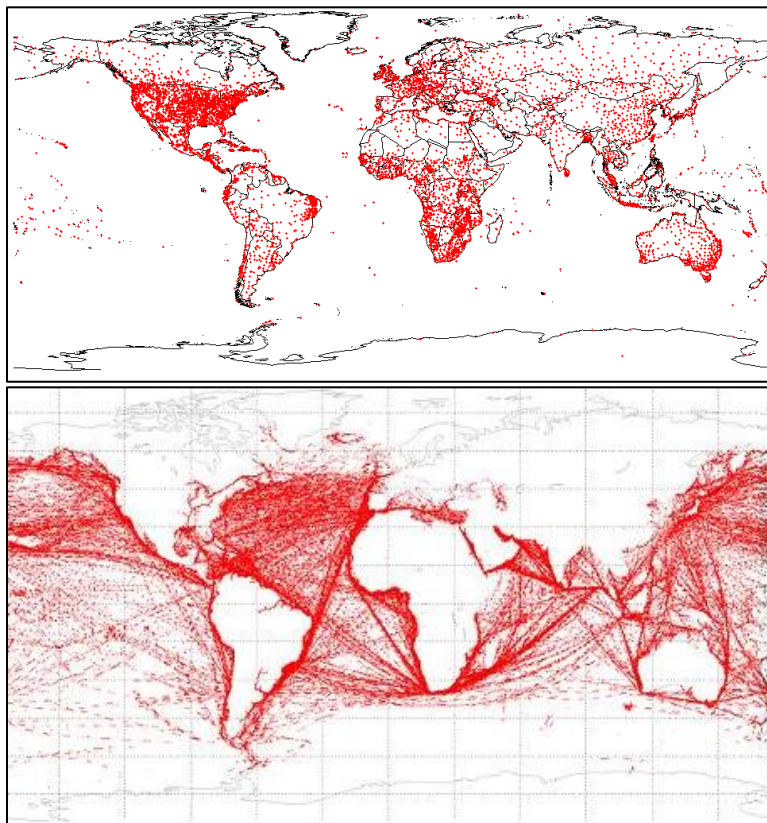
Fig. 2.2 Global distribution of land precipitation data stations (top) and ship reports (bottom) from the Global Observing Systems Information Center (GOSIC) operated by the U.S. National Oceanic and Atmospheric Administration's National Climatic Data Center (NCDC) (Diamond and Lief 2009).

2.2.1   NCEP/NCAR Reanalysis data

The NCEP/NCAR Reanalysis I Project is a joint project between the National Centers for Environmental Prediction (NCEP) and the National Center for Atmospheric Research (NCAR) with the goal of producing complete records using historical atmospheric data. The dataset includes readings taken from land surface stations, ships, rawinsonde, pibal, aircraft, satellite, and other sources, which are then quality controlled and integrated with a data assimilation system (Kalnay et al. 1996). Through this process, the reanalysis project fills in the gaps in the historical data records caused by missing, erroneous, or incomplete measurements. The model used for NCEP Reanalysis is the medium-range forecast (MRF) T62 model with an equivalent resolution of 210 km. This version of the model contains 28 pressure levels in the vertical which provide detailed resolution at both the planetary boundary layer and at upper atmospheric layers.

For the NCEP Reanalysis model, the analysis scheme is the spectral statistical interpolation (SSI) without initialization. In this scheme, the analysis variables are spectral coefficients, which are evaluated using the same basic equations as statistical interpolation (Parish and Derber 1992). The NCEP model uses the Pan-Grell scheme (Pan and Wu 1994) for parameterization of convection. More detailed information about the model may be acquired from Kalnay et al. (1996).

2.2.2   GPCP precipitation data

The World Climate Research Programme (WCRP) established the Global Precipitation Climatology Project (GPCP) to formulate a dataset which would provide a more complete understanding of the spatial and temporal patterns of global precipitation

by merging data from multiple sources. The most recent version of the dataset combines data from over 6000 rain gauge stations, satellite geosynchronous and low-orbit infrared and microwave readings, and sounding observations onto a 2.5-degree grid (Adler et al. 2003). The GPCP dataset provides monthly precipitation estimates from 1979 to the present. The project provides improvements over other precipitation datasets by using satellite-based rainfall estimates to provide a more complete analysis of rainfall over oceans, and adds additional spatial detail to rainfall estimates over land. A complete description can be obtained from Adler et al. (2003).
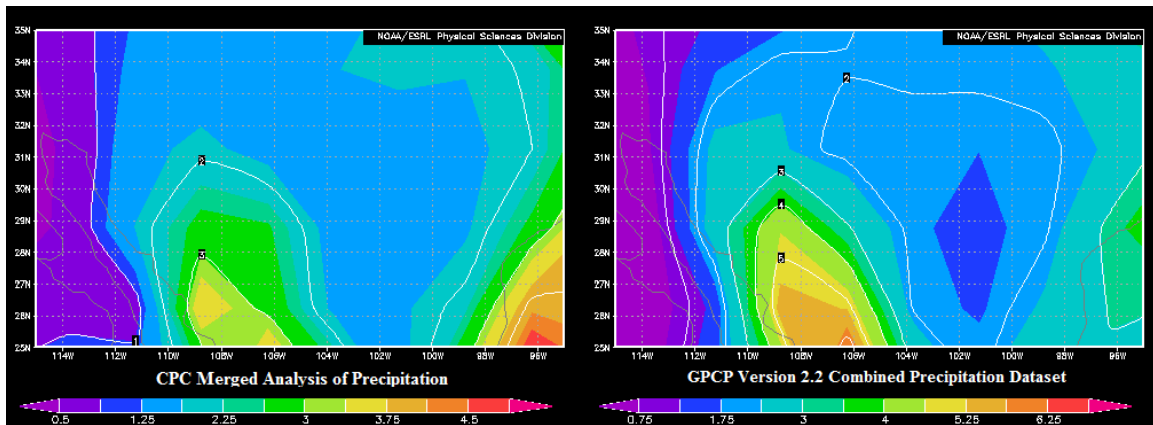
Fig. 2.3 Comparison of average precipitation produced for summertime (July-September) long term average (1979-2000) precipitation using CMAP (left) and GPCP (right) precipitation datasets for the southwestern US region. Generated using mean standard monthly data from the NOAA Earth System Research Laboratory website (http://www.esrl.noaa.gov/psd/data/gridded/).

2.2.3   CMAP precipitation data

The CPC Merged Analysis of Precipitation (CMAP) was constructed due to the inherent limitations of other large-scale precipitation dataset sources, including incomplete global coverage and non-negligible bias (Xie and Arkin 1995). This analysis has been created by merging several precipitation data sources, including satellite observations and the NCEP/NCAR Reanalysis data. CMAP consists of gridded fields of

global monthly precipitation constructed on a 2.5-degree grid for the years 1979-2000, and the dataset features precipitation distributions with full global coverage and improved quality compared to the individual data sources. The dataset has been successfully used to reproduce and investigate the annual and interannual variability of large-scale precipitation. For a complete account of the construction of the dataset and comparison with observational precipitation data, see Xie and Arkin (1997).

2.2.4   Selection of observational datasets

When selecting a particular observational dataset for use in validation and verification of climate model simulations, it is important to consider the strengths and limitations of each dataset. The usefulness of a dataset for employment with the construction of climate projections which rely on model bias (such as the introduced alternative approach in Chapters 4 and 5) can be highly sensitive to the methods used for regridding or reanalyzing the in-situ measurements. For example, the GPCP dataset combines station observations with satellite measurements for full global coverage, but it has a known weakness of low precipitation estimates over ocean and water regions. The CMAP dataset, by contrast, blends five different satellite estimates and does not suffer from the same bias issue over ocean regions, but the satellite records used for the dataset are inhomogenous, and data from the NCEP Reanalysis 1 dataset is used to fill in gaps at high latitudes. Studies which rely on the choice of observational dataset for verification of model data should consider a particular dataset's strengths, especially for regional construction of climate projections.

2.3 Introduction to numerical climate modeling

Modern climate models contain three-dimensional fully-coupled routines with separate model components for the atmosphere, ocean, land, and sea ice realms of the Earth system. Although specific models vary in their particular parameterizations of various climate processes, all models incorporate the same full set of basic equations (Peixoto and Oort 1992). This section presents the basic "primitive" equations used in climate models and discusses the common numerical methods used to solve these equations. Finally, this section introduces model parameterization schemes related to moisture and precipitation.

2.3.1 Basic model equations

Climate models utilize systems of differential equations derived from the basic principles of physics, fluid motion, and chemistry. The fundamental equations which govern the motions and processes of the atmosphere, oceans, and sea ice have been developed from the conservation laws for momentum, mass, and energy. An equation of state is also used in order to close the system of equations produced by the conservation laws. These equations will be described in their "primitive" forms (prior to simplifications) following the derivations by Washington and Parkinson (2005).

Conservation of momentum

The motions of the climate system can be derived from the fundamental equation of classical mechanics in its vector form, expressed as

$$\boldsymbol{F} = \frac{d(m\boldsymbol{v})}{dt}. \qquad (2.1)$$

This expression is applied to a particle of air, water, or ice in which the particle retains its original mass, so we can assume that m is constant. For large-scale models in three dimensions, we will consider a spherical coordinate system in which the longitude is defined by λ (increasing to the east), latitude by ϕ (increasing to the north), and the radial distance r measured from the center of the Earth. This radial distance equals the radius of the Earth a plus the height z above the Earth's surface such that $r = a + z$ (the value of a is given as constant in modeling applications). The linear wind velocities in the three primary directions are labeled as u, v, and w, respectively. Based on plane geometry, we may define these velocities along a latitude circle, along a meridian, and local vertical velocity as

$$u = r \cos \phi \frac{d\lambda}{dt}, \qquad v = r \frac{d\phi}{dt}, \qquad w = \frac{dz}{dt}. \qquad (2.2 - 2.4)$$

Next, we may rewrite (2.1) in spherical coordinates in the λ-direction,

$$a_\lambda = \frac{du}{dt} = \sum forces_\lambda, \qquad (2.5)$$

We may further expand (2.5) into partial derivatives using the chain rule. Using the λ-direction as an example, and combining (2.2-2.4), we obtain

$$\frac{du}{dt} = \frac{\partial u}{\partial t} + \frac{u}{r \cos \phi} \frac{\partial u}{\partial \lambda} + \frac{v}{r} \frac{\partial u}{\partial \phi} + w \frac{\partial u}{\partial z}. \qquad (2.6)$$

Corresponding equations for ϕ and z may be derived similarly. The forces in (2.5) are expressed as forces per unit mass; these are the major forces of motion acting on the climate system. These include the gravitational force, the centripetal and Coriolis forces due to the rotation of the Earth, pressure forces, and frictional forces. Considering a

12

volume of air on the Earth's surface as depicted in Fig. 2.4, the net forces per unit mass acting on the volume are,

$$-\frac{1}{\rho\, r \cos\phi}\frac{\partial p}{\partial\lambda}, \qquad -\frac{1}{\rho\, r}\frac{\partial p}{\partial\phi}, \qquad and\; -\frac{1}{\rho}\frac{\partial p}{\partial z} \qquad (2.7-2.9)$$

for the λ-, ϕ-, and z-components respectively, where density $\rho = m/$volume and volume $= r^2 \cos\phi\, \Delta\lambda$. Since all climate and weather models use a rotating frame of reference, the Coriolis force represents the deflection caused by the rotational acceleration of the Earth on an object given an initial velocity and the resulting force per unit mass acting on that object. If Ω is the angular velocity of the Earth, then the Coriolis parameter is defined as $f = 2\Omega \sin\phi$. The frictional force terms are expressed as F_λ, F_ϕ, and F_z. Combining these forces and (2.7-2.9), (2.5) in each direction becomes,

$$\frac{du}{dt} - \left(f + u\frac{\tan\phi}{a}\right)v = -\frac{1}{a\cos\phi}\frac{1}{\rho}\frac{\partial p}{\partial\lambda} + F_\lambda \qquad (2.10)$$

$$\frac{dv}{dt} + \left(f + u\frac{\tan\phi}{a}\right)u = -\frac{1}{\rho a}\frac{\partial p}{\partial\phi} + F_\phi \qquad (2.11)$$

$$\frac{dw}{dt} = -\frac{1}{\rho}\frac{\partial p}{\partial z} - g + F_z \qquad (2.12)$$

where g is the acceleration of gravity. It should be noted that (2.10-2.12) are essentially the Navier-Stokes equations of fluid dynamics, with the addition of the Coriolis and friction terms due to the rotating frame of reference. These equations are often simplified for large-scale atmospheric motions. In such cases, the pressure gradient, Coriolis, and gravity terms become the dominant components, and we obtain the *geostrophic* equations. The geostrophic assumption is often used for the oceans where the large-scale motions are generally slow. However, the geostrophic approximation becomes invalid

13

near the equator where the Coriolis term equals 0. The z-direction geostrophic equation is termed the hydrostatic balance which consists only of a balance between the gravity and vertical gradient of pressure. The hydrostatic approximation is invalid for small-scale (<10 km) motions such as the convective processes which generate the storms inherent to monsoon precipitation.
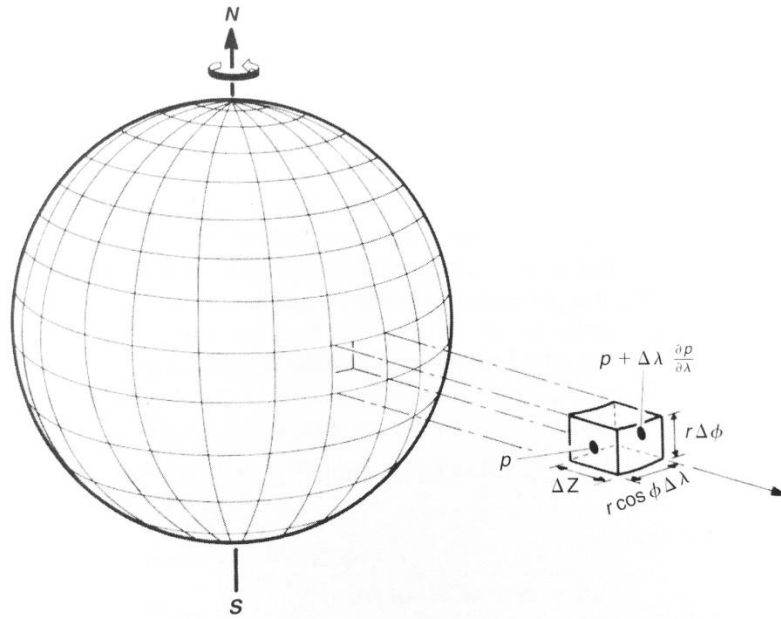
Fig. 2.4 Schematic of pressure forces on a volume of air in spherical coordinates (Washington and Parkinson 2005).

Conservation of mass

Considering the same volume of air in Fig. 2.4, the total mass flux difference across the faces is equal to the time change of the mass of the volume. Assuming the volume remains constant, the mass continuity becomes,

$$\frac{d\rho}{dt} + \frac{\rho}{a \cos \phi} \left[\frac{\partial u}{\partial \lambda} + \frac{\partial}{\partial \phi} (v \cos \phi) \right] + \rho \frac{\partial w}{\partial z} = 0. \qquad (2.13)$$

The time derivative term is very important for atmosphere applications where air is compressible; however, this term may be neglected in ocean or sea ice modeling. If ρ is

14

replaced with the concentration of water vapor ρ_v, then (2.13) becomes the equation for the conservation of water, which is used to obtain the vertically integrated mass conservation equation for water vapor in section 7.4.

First law of thermodynamics

Also called the law of the conservation of energy, the first law of thermodynamics is a statement of how the thermal energy of a system is related to the work done by compression or expansion of a volume of gas. It can be written as

$$C_v \frac{dT}{dt} + p \frac{d}{dt}\left(\frac{1}{\rho}\right) = Q. \qquad (2.14)$$

For atmospheric models, this system is considered to be a small volume of gas. In the ocean, the $(d/dt)(1/\rho)$ term is usually neglected because water is considered incompressible. The Q term is called the nonadiabatic term because it represents an external gain or loss of heat. When $Q = 0$, the process is called adiabatic. For short-term atmospheric and ocean studies, the assumption of adiabatic motion is frequently used; however, this term becomes important when considering long-term climate processes as the net gain or loss of heat can be significant. For climate model simulations which incorporate emissions scenarios, the forcings of the greenhouse gases (GHGs) and other atmospheric forcings enter the system through the nonadiabatic term (see Fig. 2.5). The radiative forcing associated with a particular emission or source is imposed on the system through a forcing term ΔQ, and the net radiative forcing of all n forcings on a system becomes the sum of their respective forcings such that $Q \rightarrow Q + \sum \Delta Q_n$.

Equation of state

Finally, the equation of state relates the density, pressure, and temperature of a gas. For the atmosphere, this equation is the ideal gas law:

$$p = \rho r t. \qquad (2.15)$$

This system of six equations (2.10 – 2.15) represents the full set of basic equations used in atmospheric science prior to simplifications and numerical approximations. For modern climate models such as those evaluated in this project, no approximations are made to simplify these primitive equations; the full set of Navier-Stokes equations, in the forms presented in (2.10-2.12), are used in both the atmospheric and ocean model components. This system contains six unknown variables (u, v, w, ρ, p, and T) as well as the frictional terms F_λ and F_ϕ and the nonadiabatic term Q. These last three terms provide the boundary conditions for the individual model components which are calculated based on interactions with the other components (such as the ocean-atmosphere surface boundary). More information regarding model components may be found in section 2.4.1.

Instead of attempting to provide solutions to fully resolved flows within the three-dimensional field, climate models employ numerical approximations to aid in the discretization of the continuous domain. Some basic equations may be solved analytically, but many equations encountered in climate modeling do not have exact solutions, so numerical solutions become crucial. Some models are based on finite difference methods, while others are based on finite element techniques (Washington and Parkinson 2005). Many modern climate models also incorporate spectral techniques in their numerical approximations of the basic equations.

2.3.2   Vertical coordinate system

Because the atmosphere exhibits a hydrostatic nature in large scales, early approximations set the vertical coordinate system at levels of pressure. However, this system experiences issues near the Earth's surface where these pressure levels can intersect mountains. To avoid computational errors related to orography, the sigma-coordinate system was developed in which the vertical sigma coordinate is a ratio of the level pressure to the surface pressure:

$$\sigma = \frac{p}{p_s}. \qquad (2.16)$$

The sigma-coordinate system follows the land surface since it is a function of the local pressure. Many models use a hybrid vertical coordinate system which incorporates the sigma levels near the surface and pure pressure levels near the top of the atmosphere.

2.3.3   Physical atmospheric processes

Since radiation is the driving source of energy for the atmosphere, the thermodynamic and moisture processes are related through the energy cycle. Radiation can be used as a forcing in the atmosphere by modifying the solar radiation flux on the Earth in the climate model. The consideration of the concentrations of radiation-absorbing chemicals in the atmospheric column as well as the terrestrial radiation produced by the warming from greenhouse gases is a critical step in climate modeling, especially when formulating future climate scenarios (discussed in detail in section 2.4.2). An enhanced hydrological cycle can have a positive feedback on trapping terrestrial radiation, while land albedo and suspended aerosols can have a negative effect

17

by reflecting incoming solar radiation (Solomon et al. 2007, TS.2.5; see Fig. 2.5). As such, the parameters controlling radiation within climate models involve multiple modeling components.

Climate models do not contain explicit equations for generating precipitation. Instead, climate models parameterize precipitation through the description of moisture and thermodynamic processes on a sub-grid scale. The models "generate" precipitation by determining whether latent heat is released in a process. This latent heat is computed in atmospheric models when the atmosphere is supersaturated (when the mixing ratio exceeds the saturated mixing ratio, or when relative humidity exceeds 100%) (Washington and Parkinson 2005). The saturated mixing ratio is only a function of pressure and the saturated pressure due to water vapor, which are both functions of temperature (from the Clausius-Clapyron relation). However, since precipitation can occur on smaller scales than model resolution can represent, some models assume latent heating occurs at lower percentages of relative humidity. Many models now also incorporate more complex parameterization schemes for producing different types of precipitation.

RF Terms		Radiative Forcing (W/m²)	RF values (W/m²)	Spatial scale	LOSU
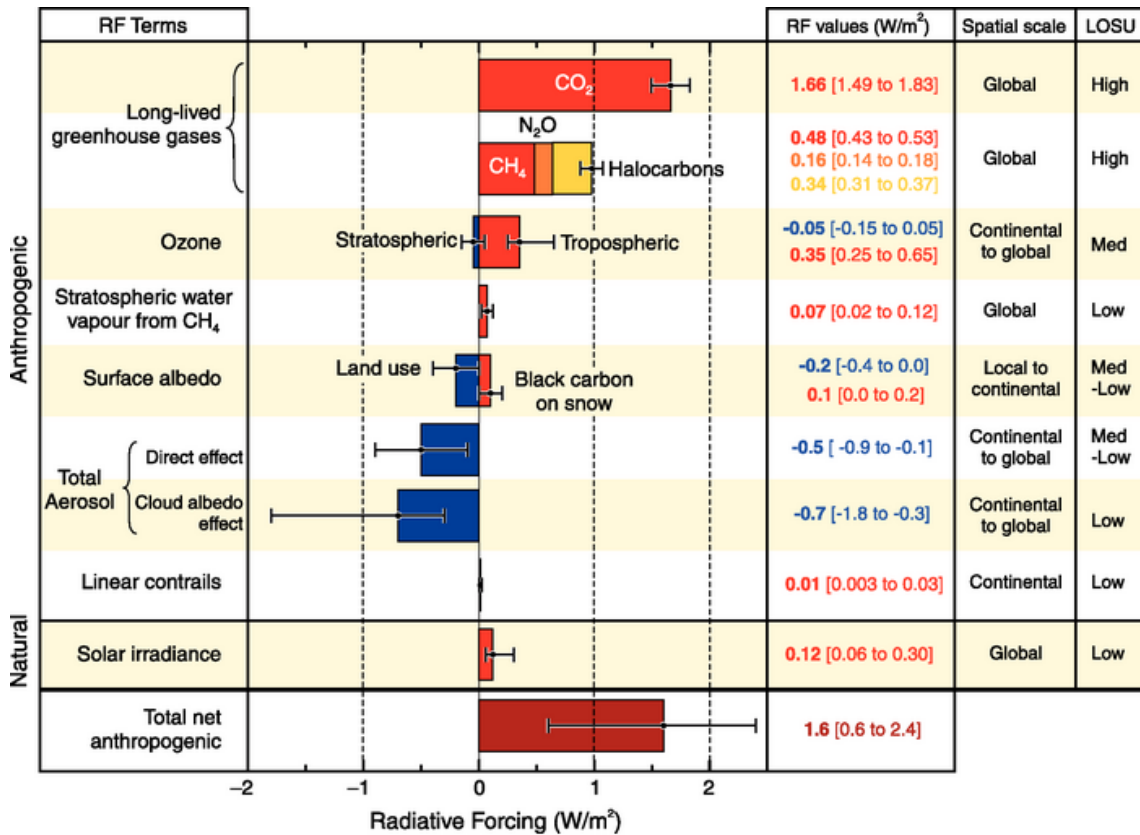
Fig. 2.5 Global mean radiative forcings and their 90% confidence intervals based on 2005 values. Columns on the right-hand side specify best estimates and confidence intervals, typical geographical extent of the forcing, and level of scientific understanding (Solomon et al. 2007).

The latent heating which occurs specifically as a result of convective precipitation is governed in models by the *cumulus parameterization*. This scheme allows for the quantitative expression of location, frequency, and intensity of processes in the model which occur at a subgrid-scale. Cumulus parameterization can be expressed as a function of potential temperature and water vapor mixing ratio, although other schemes have been developed which parameterize convection based on vertical mass flux. Table 2.1 illustrates the variety of schemes used for both large-scale (stratiform) and convective precipitation. Information regarding model issues associated with the application of the various convective schemes can be found in section 3.2.3.

19

Model	Stratiform precipitation	Convective precipitation
CCSM3, CCSM2	Prognostic condensate and precipitation parameterization (Zhang et al. 2003)	Simplified Arakawa and Schubert (1974) (cumulus ensemble) scheme developed by Zhang and McFarlane (1995)
CGCM3.1	Precipitation occurs whenever the local relative humidity is supersaturated	Zhang and McFarlane (1995) scheme
CSIRO-Mk3.0	Statistical cloud scheme of Ricard and Royer (1993)	Mass flux convection scheme with Kuo-type closure
CNRM-CM3	Stratiform cloud condensate scheme from Rotstayn (2000)	Bulk mass flux convection scheme with stability-dependent closure (Gregory and Rowntree 1990)
ECHAM5/MPI-OM	Prognostic equations for the water phases, bulk cloud microphysics (Lohmann and Roeckner 1996)	Bulk mass flux scheme (Tiedtke 1989) with modifications for deep convection according to Nordeng (1994)
FGOALS-g1.0	Precipitation occurs whenever the local relative humidity is supersaturated	Zhang and McFarlane (1995) scheme
GFDL-CM2.0, GFDLCM2.1	Cloud microphysics from Rotstayn (2000) and macrophysics from Tiedtke (1993)	Relaxed Arakawa–Schubert scheme from Moorthi and Suarez (1992)
GISS-AOM	Subgrid-relative humidity-based scheme	Subgrid plume and buoyancy-based scheme (online at http://aom.giss.nasa.gov/DOC4X3/ATMOC4X3.TXT)
GISS-ER	Prognostic stratiform cloud based on moisture convergence (Del Genio et al. 1996)	Bulk mass flux scheme by Del Genio and Yao (1993)
HadCM3	Large-scale precipitation is calculated based on cloud water and ice contents (similar to Smith 1990)	Bulk mass flux scheme (Gregory and Rowntree 1990), with the improvement by Gregory et al. (1997)
HadGEM1	Mixed phase cloud scheme (Wilson and Ballard 1999)	Revised bulk mass flux scheme
INM-CM3.0	Stratiform cloud fraction is calculated as linear function of relative humidity	Lagged convective adjustment after Betts (1986), but with changed referenced profile for deep convection
IPSL-CM4	Cloud cover and in-cloud water are deduced from the large-scale total water and moisture at saturation (Bony and Emmanuel 2001)	Moist convection is treated using a modified version (Grandpeix et al. 2004) of the Emanuel (1991) scheme
MIROC3.2-medres, hires	Prognostic cloud water scheme based on Le Treut and Li (1991)	Prognostic closure of Arakawa–Schubert based on Pan and Randall (1998) with relative humidity–based suppression (Emori et al. 2001)
MRI-CGCM2.3.2a	Precipitation occurs whenever the local relative humidity is supersaturated	Prognostic Arakawa–Schubert based on Pan and Randall (1998)
PCM	Precipitation occurs whenever the local relative humidity is supersaturated	Zhang and McFarlane (1995) scheme

Table 2.1 Description of CMIP3 climate model parameterization schemes for stratiform and convective precipitation (Dai 2006).

2.4   Background of the IPCC and CMIP

Climate model simulations currently provide the most important knowledge basis for the projection of future climate on multidecadal to centennial time scales. The most comprehensive collection of peer reviewed and published scientific/technical literature in climate science has been compiled into four assessment reports since 1990 by the Intergovernmental Panel on Climate Change (IPCC), the most recent of which is the AR4 Report (Solomon et al. 2007). The IPCC does not carry out research or monitor climate

data; rather, the authors of the reports assess and compile the most current information available.

In order to provide controlled conditions for model evaluation and aid the IPCC in their task, the WCRP formed model intercomparison projects (CMIPs) which collect output data contributed by leading modeling centers around the world. The output data is made available freely to enable scientists outside the major modeling centers to perform research of relevance to the IPCC in preparation for their assessment reports.

2.4.1   Details of the CMIP model ensembles

The WCRP prepared the third Coupled Model Intercomparison Project (CMIP3) for the most recent AR4 report. Over 20 coupled general circulation models (GCMs) comprise the CMIP3 archive, and their simulation data has been used to produce the AR4 projections (Meehl et al. 2005). Table 2.2 contains a list of the CMIP3 models and their respective modeling centers which are used in this project. Since many of these models have been developed independently of each other, some of the individual components differ from model to model, as do their respective horizontal resolutions. However, the models must follow certain guidelines for inclusion in the CMIP3 archive. The models are required to produce a basic output variable list from simulations based on a set of standardized conditions (more information concerning these conditions will be discussed in section 2.4.2 regarding climate scenarios).

The Coupled Model Intercomparison Project phase 5 (CMIP5) is currently in the process of releasing simulation data. It contains the most recent ensemble of models to improve upon its predecessor (CMIP3) with the formulation of new long-term

simulations using experiments performed with additional types of models which were not present in the previous archives (Taylor et al. 2012). Table 2.3 provides a list of the models from the CMIP5 archive which are used within this project for analysis. This list is not exhaustive since over 30 models are included in the archive; however, only the selected models have been used based on the most current availability of data. In addition to containing a set of more refined model resolutions, the CMIP5 archive features a broader variety of experiments. Along with the most recent conventional climate models (Atmospheric-Ocean General Circulation Models – AOGCMs), CMIP5 includes experiments from the newest Earth system models (ESMs). Many of the climate model centers have provided both a general circulation model and an ESM version of their model for use in the archive.

ESMs contain several features which are not present in their GCM counterparts. For example, ESMs contain a closed carbon cycle with the addition of biogeochemistry routines to the land and ocean components of the models. Several of the ESM model versions also have parameters which simulate changes in the atmospheric chemistry; these models are able to explicitly predict and calculate the formation and decay of atmospheric aerosols (Taylor et al. 2012).

All models in the CMIP3 and CMIP5 archives are fully-coupled models in which the ocean, atmosphere, land, and sea ice components are each distinct models which mutually interact and exchange information through surface boundaries. The component models are stand-alone climate models themselves; for example, the atmospheric component of the CMIP3 fully-coupled NCAR CCM3 model is the NCAR CAM 3.1 atmospheric model which is operated using ocean and land surfaces as constant boundary

conditions which are provided as inputs of the simulations. The CAM 3.1 atmospheric model is used to perform certain analyses in this project; Chapter 8 provides more details regarding these simulations.

Institution	Model	Horizontal Resolution
Bjerknes Centre for Climate Research (Norway)	BCCR-BCM2.0	128x64
National Center for Atmospheric Research (USA)	CCSM3	256x128
Canadian Centre for Climate Modelling & Analysis (Canada)	CGCM3.1(T47)	96x48
	CGCM3.1(T63)	128x64
Météo-France / Centre National de Recherches Météorologiques (France)	CNRM-CM3	128x64
CSIRO Atmospheric Research (Australia)	CSIRO-Mk3.0	192x96
Max Planck Institute for Meteorology (Germany)	ECHAM5/MPI-OM	192x96
Meteorological Institute of the University of Bonn, Meteorological Research Institute of KMA, and Model and Data group. (Germany/Korea)	ECHO-G	96x48
LASG / Institute of Atmospheric Physics (China)	FGOALS-g1.0	128x60
US Dept. of Commerce / NOAA / Geophysical Fluid Dynamics Laboratory (USA)	GFDL-CM2.0	144x90
	GFDL-CM2.1	144x90
NASA / Goddard Institute for Space Studies (USA)	GISS-AOM	90x60
	GISS-EH	72x46
	GISS-ER	72x46
Institute for Numerical Mathematics (Russia)	INM-CM3.0	72x45
Institut Pierre Simon Laplace (France)	IPSL-CM4	96x72
Center for Climate System Research (The University of Tokyo), National Institute for Environmental Studies, and Frontier Research Center for Global Change (JAMSTEC) (Japan)	MIROC3.2(hires)	320x160
	MIROC3.2(medres)	128x62
Meteorological Research Institute (Japan)	MRI-CGCM2.3.2	128x64
National Center for Atmospheric Research (USA)	PCM	128x64
Hadley Centre for Climate Prediction and Research / Met Office (UK)	UKMO-HadCM3	96x73
	UKMO-HadGEM1	192x145

Table 2.2 CMIP3 climate models which are analyzed in this project, shown with their respective modeling centers and horizontal resolutions (Meehl et al. 2005).

Institution and Country	Model	Horizontal Resolution
Beijing Climate Center, China Meteorological Administration (China)	BCC-CSM1.1	128x64L26(T42)
	BCC-CSM1.1.m	128x64L26(T42)
College of Global Change and Earth System Science, Beijing Normal University (China)	BNU-ESM	128x64L26(T42)
Canadian Centre for Climate Modelling and Analysis (Canada)	CanCM4	128x64L35(T63)
	CanESM2	128x64L35(T63)
National Center for Atmospheric Research (USA)	CCSM4	288x192L26
Centro Euro-Mediterraneo per I Cambiamenti Climatici (Italy)	CMCC-CESM	288x192L26
	CMCC-CM	480x240L31(T159)
	CMCC-CMS	480x240L31(T159)
Centre National de Recherches Meteorologiques / Centre Europeen de Recherche et Formation Avancees en Calcul Scientifique (France)	CNRM-CM5	256x128L31(T127)
CSIRO (Commonwealth Scientific and Industrial Research Organisation, Australia), and Bureau of Meteorology (Australia)	ACCESS1.0	192x145L38
	ACCESS1.3	192x145L38
Commonwealth Scientific and Industrial Research Organisation in collaboration with the Queensland Climate Change Centre of Excellence (Australia)	CSIRO-Mk3.6.0	192x96L18(T63)
EC-EARTH consortium (multiple)	EC-EARTH	320x160L62(T159)
LASG, Institute of Atmospheric Physics, Chinese Academy of Sciences; and CESS, Tsinghua University (China)	FGOALS-g2	128x108L26
LASG, Institute of Atmospheric Physics, Chinese Academy of Sciences (China)	FGOALS-s2	128x108L26
The First Institute of Oceanography (China)	FIO-ESM	128x108L26
Geophysical Fluid Dynamics Laboratory (USA)	GFDL-CM3	144x90L48
	GFDL-ESM2G	144x90L24
	GFDL-ESM2M	144x90L24
NASA Goddard Institute for Space Studies (USA)	GISS-E2-H	144x90L40
	GISS-E2-H-CC	144x90L40
	GISS-E2-R	144x90L40
	GISS-E2-R-CC	144x90L40
Met Office Hadley Centre (UK)	HadCM3	96x73L19
National Institute of Meteorological Research (South Korea)	HadGEM2-AO	192x145L40
Met Office Hadley Centre (UK)	HadGEM2-CC	192x145L40
	HadGEM2-ES	192x145L40
Institute for Numerical Mathematics (Russia)	INM-CM4	180x120L21
Institut Pierre-Simon Laplace (France)	IPSL-CM5A-LR	96x96L39
	IPSL-CM5A-MR	144x142L39
	IPSL-CM5B-LR	96x96L39
Atmosphere and Ocean Research Institute (The University of Tokyo), National Institute for Environmental Studies, and Japan Agency for Marine-Earth Science and Technology (Japan)	MIROC4h	640x320L56(T213)
	MIROC5	256x128L40(T85)
Japan Agency for Marine-Earth Science and Technology, Atmosphere and Ocean Research Institute (The University of Tokyo), and National Institute for Environmental Studies (Japan)	MIROC-ESM	128x62L80(T42)
	MIROC-ESM-CHEM	128x62L80(T42)
Max Planck Institute for Meteorology (Germany)	MPI-ESM-LR	192x96L47(T63)
	MPI-ESM-MR	192x96L95(T63)
	MPI-ESM-P	192x96L47(T63)
Meteorological Research Institute (Japan)	MRI-CGCM3	320x160L48(T159)
Norwegian Climate Centre (Norway)	NorESM1-M	144x96L26
	NorESM1-ME	144x96L26

Table 2.3 CMIP5 climate models which are analyzed in this project, shown with their respective modeling centers and horizontal resolutions (Taylor et al. 2012).

The individual model simulations are ensemble-averaged with equal weight to construct the IPCC projection for the 21st century climate. However, a significant degree of variability in the errors of the model simulations for the 20th century climate is well-known at both global and regional scales (e.g. Taylor 2001, Solomon et al. 2007, Lin et al. 2008, Reichler and Kim 2008). As a compelling example of model discrepancy, Fig. 2.6 compares the North American monsoon precipitation from the 20th century simulations (the 20C3M case in CMIP3: more information regarding model scenarios may be found in section 2.4.2) with 22 climate models from the CMIP3 ensemble and the observed counterpart (top left) based on the CMAP dataset. It shows the ratio of summertime (July-September) precipitation to annual precipitation. The large value of this ratio in the subtropical region over Mexico and the Southwest U.S. is a unique signature of the North American summer monsoon. Such a contrast in the quality of the CMIP3 model simulations of present-day climate has also been demonstrated in recent studies for various regions and variables (Reichler and Kim 2008, Lin et al. 2008). This project incorporates such information in a detailed analysis of the major dynamical processes and water balance which will further help us understand the nature of the model bias and assess the integrity of the climate models, especially concerning the simulations for semi-arid regions.
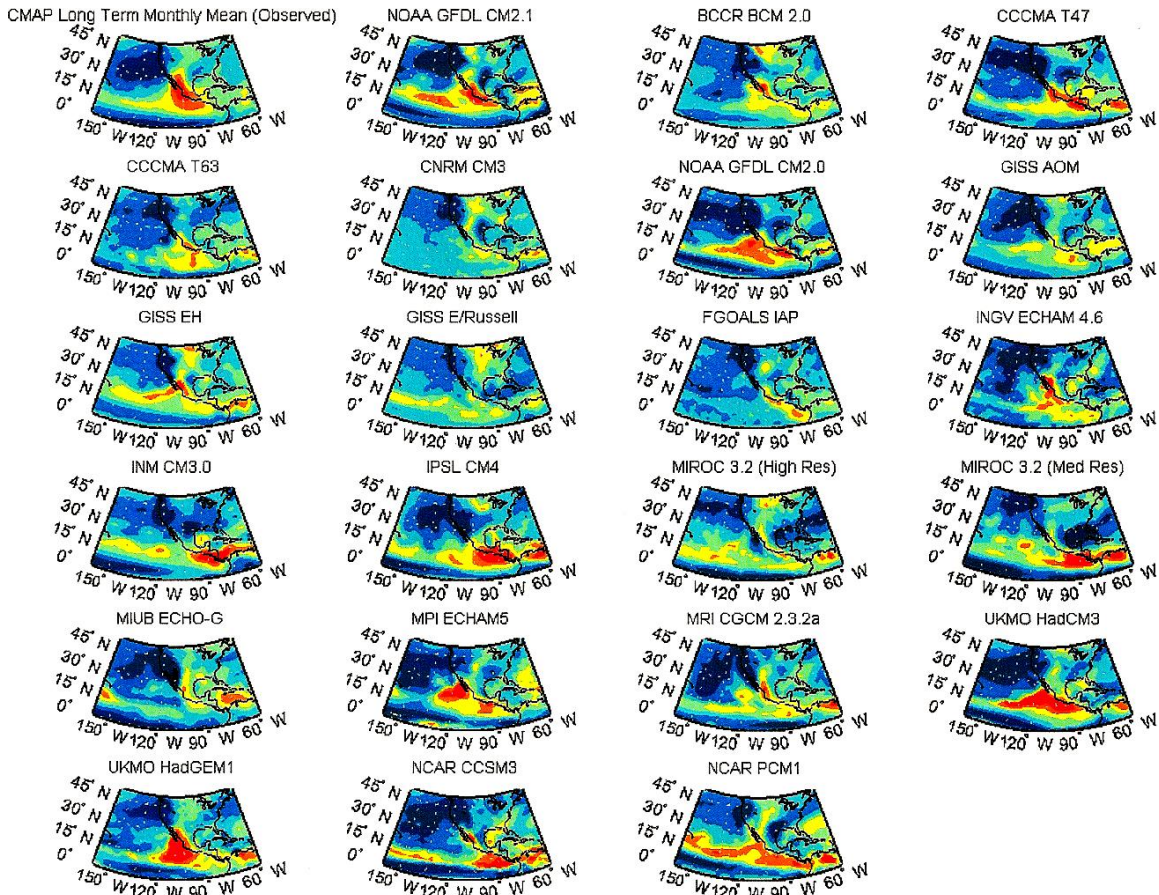
Fig. 2.6 North American Monsoon phenomenon from observation (top left, using CMAP data for 1979-2000) and climate model simulations for present-day climate (based on the 20C3M runs for CMIP3). Shown is the ratio of summertime precipitation to annual precipitation. The color interval is 0.1. Regions filled with deepest blue color are where the ratio is between 0 and 0.1; those filled with red/orange colors have the highest values of the ratio.

2.4.2   Scenarios for climate change research

The long-term and uncertain nature of climate change and its driving forces require the development of a standard set of scenarios that include the range of emissions of all relevant types of greenhouse gases. The accepted set of scenarios are generated and used by different types of models and analytic frameworks, including various types of climate models as well as approaches to assess impacts, adaptation, and vulnerability. These future projections are comprised of the Special Report on Emissions Scenarios

(SRES) scenarios used in CMIP3 climate model experiments (Nakićenović et al. 2000), while the newer CMIP5 archive uses emission scenarios determined by "representative concentration pathways" (RPCs) (Moss et al. 2008). This section highlights relevant details of the two scenario sets and their essential relevance to this project.

Future greenhouse gas and aerosol emission levels will be determined by the result of a complex set of interactions, including energy use, economic growth of developing countries, and sustainability efforts. How those factors will unfold and thus affect the future concentration levels of atmospheric greenhouse gases is highly uncertain; however, a representation of a possible range of outcomes for assessing the potential impacts of anthropogenic climate change has been developed as an established set of scenarios. These scenarios are originally based on the 1990 IPCC released (SA90) emission pathways, later developed into the 1992 IPCC scenarios (IS92) which provide estimates for the full range of greenhouse gases and aerosol concentrations (Solomon et al. 2007, section 1.4). A supplemental report was released in 1996 as the SRES, which incorporated the emission scenarios of IS92 into a standard four sets of scenarios and 40 individual scenarios (Nakićenović et al. 2000). The SRES includes a more comprehensive set of factors, including energy usage and the impacts of possible societal adaptation to the effects of climate and mitigation of greenhouse gas emissions. Fig. 2.7 illustrates the range of future projected CO_2 emissions corresponding to each of the four SRES scenario families. The A1 scenario family depicts the range of CO_2 emissions corresponding to rapid economic growth, global population that peaks in mid-century and declines thereafter, and future energy usage divided into three groups: fossil intensive (A1FI), non-fossil energy (A1T), or a balance energy usage from all sources (A1B).
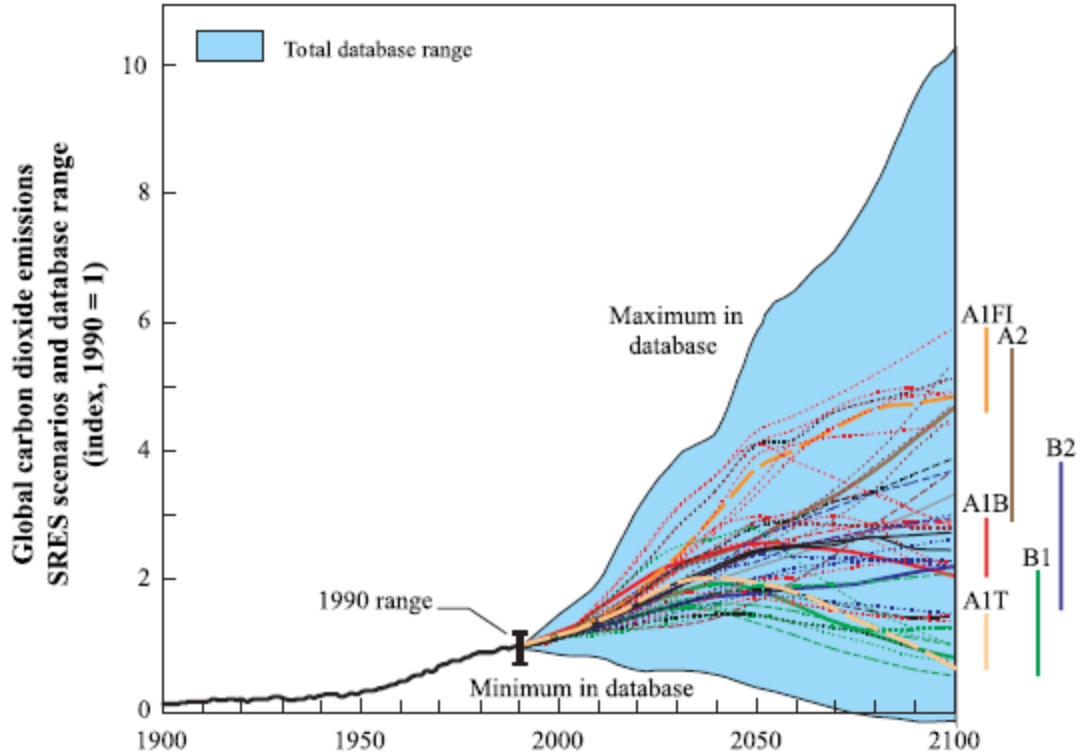
Fig. 2.7 Total global annual CO2 emissions normalized to 1990 values projected by the CMIP3 SRES scenario groups (Nakićenović et al. 2000).

Similarly, Fig. 2.7 depicts the projected range of CO2 emissions based on continuously increasing population (A2), a peaking population and improved sustainability (B1), and a continuously increasing population with regional sustainability efforts (B2).

Four new scenario groups have been formulated for use in CMIP5. Unlike their SRES predecessors, these scenarios incorporate a range of socioeconomic and technological development projections in a parallel process which allows for the inclusion of the most recent climate observations, and also unlike the SRES scenarios, they assume that policy actions will be implemented to mitigate greenhouse gas emissions (Moss et al. 2008, 2010). The new model simulations are forced using predefined scenarios determined by "representative concentration pathways" (RPCs). The
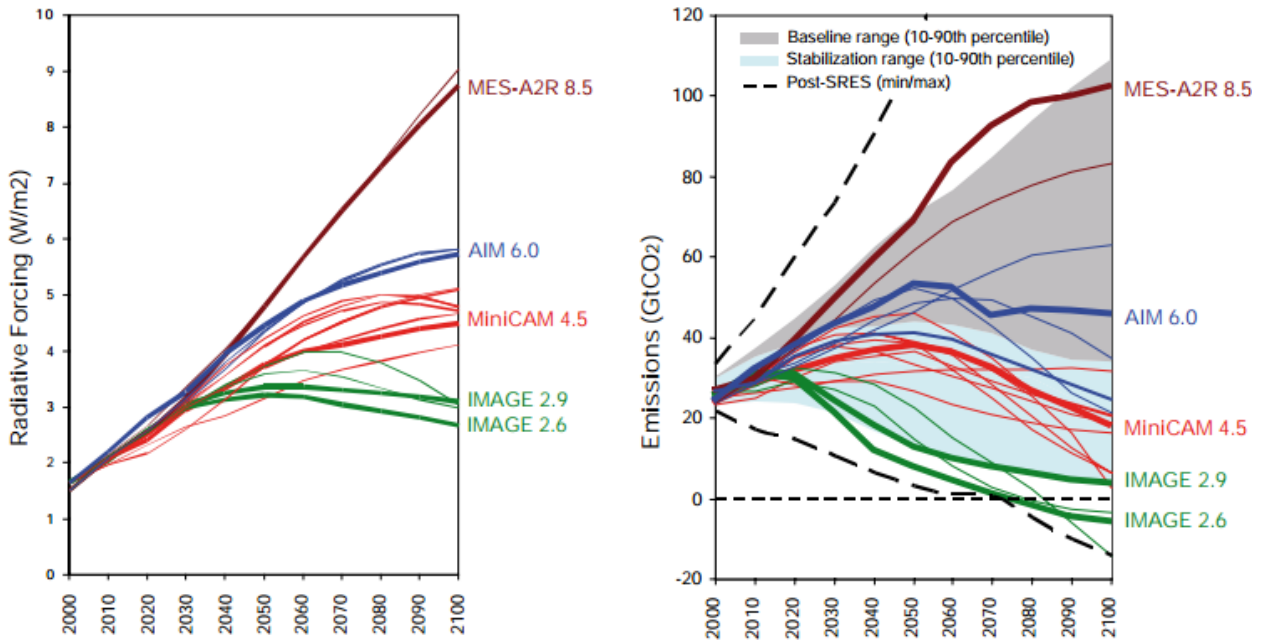
Fig. 2.8 Average global radiative forcing projected by the four RCP scenario groups based on projected emissions of the corresponding development teams: MESSAGE (RCP 8.5), AIM (RCP 6.0), MiniCAM (RCP 4.5), and IMAGE (RCP 2.6 and 2.9) (Moss et al. 2008).

RCP labels are based on a rough estimate for the corresponding radiative forcing (in W/m2) in the year 2100 for the particular scenario, as shown in Fig. 2.8.

The radiative forcing level is estimated based on the greenhouse gas forcings particular to each scenario. The forcing does not include the direct impacts of land albedo or mineral dust aerosols. As such, the RCP scenarios are not standalone, fully-integrated scenarios; rather, they are a set of projections which consist only of the components of radiative forcing needed to serve as inputs for climate modeling. The scenario groups formulate their forcing value based on contrasting scenarios: a "peaked" forcing with substantially reduced greenhouse gas concentrations (RCP 2.6), a stabilized forcing with reduced greenhouse gas emissions (RCP 4.5), a rising but gradually stabilizing forcing with some sustainability actions (RCP 6.0), and a rising forcing caused by continuously

29

increasing emissions (RCP 8.5) (Moss et al. 2010). The RCP data components include historical (1850 - 2000) emissions data and aerosols data as well as the projected emissions for each of the RCP scenarios (2000-2100) for the following gases: CH_4, SO_2, NO_x, CO, NH_3, BC, OC and VOC. Also included are the historical and RCP land-use projections and associated land-use transitions. These components are provided by the scenario groups specifically for use in CMIP5 model simulations at www.iiasa.ac.at/web-apps/tnt/RcpDb/.

The selection of a scenario when obtaining model simulation data is crucial for evaluating the climate change effects present in future simulations; each scenario will produce a different range of future projections, which can result in dramatically different conclusions. The CMIP3 analyses performed for this project use data from the model simulations forced with the SRES A1B scenario because it stands as a more conservative projection relative to the other scenarios. In this case, "conservative" refers to the scenario's projected storyline of a plausible future homogenous world with continued rapid economic growth and a peaking global population, in which CO_2 emissions increase until mid-21st century and decline thereafter to 720 parts per million in 2100. As such, the SRES A1B scenario has been consistently used in other analyses of future climate projections (e.g. Mariotti et al. (2008) and Seager et al. (2007), among others). Similarly, the CMIP5 analyses in the majority of this project use data from model simulations forced with the RCP 4.5 scenario for its correspondingly conservative projections; simulations utilizing this scenario have already been used in a number of recent preliminary analyses of the CMIP5 ensemble, such as efforts by Kim and Yu (2012) and Kitoh (2012).

In addition to the future scenario pathways presented for the CMIP3 and CMIP5 archives, this project also uses model simulation data which is not forced based on a particular scenario. This simulation data comes from historical runs of the 20th century in which the experiments are run with greenhouse gas concentrations increasing as observed. For the CMIP3 archive, the non-SRES historical scenario used is 20C3M; for CMIP5, the equivalent scenario ('historical') is used. As intended for this project, any analyses involving 20th century model simulated data utilize the 20C3M scenario for CMIP3 and 'historical' scenario for CMIP5.

CHAPTER 3

SCIENTIFIC ISSUES AND GOALS

3.1   Relevance of the water cycle and precipitation

The ability to predict climate changes becomes increasingly important as we better understand the implications: according to the IPCC 4th Assessment (AR4) Report (Solomon et al. 2007) and updated recent studies (Seager et al. 2007, Karl et al. 2009), a moderate change in global temperature will accelerate the hydrological cycle. Areas in high latitudes and the wet tropics are projected to have increased precipitation, while semi-arid regions in midlatitudes and subtropics are projected to become even drier through decreased precipitation and increased evaporation. This scenario, if true, has critical consequences for semi-arid regions such as the Southwest U.S., where over-development has already led to projected shortage of water but climate change will exacerbate the local water imbalance. Considering the case study of Lake Mead, a major water resource which is part of the Colorado River system, water management has become an urgent concern for the communities dependent on this water supply. Increased temperature and evaporation and decreased precipitation have already contributed to runoff reduction to the river system, and if no water management strategies are implemented, the water storage levels of this resource will become depleted (Barnett and Pierce 2008). How fast this process will unfold depends on the detail of the projected climate change for the region. Such a case is not unusual in the region; projections show that more areas in the Southwestern U.S. will exhibit signs of water resource depletion and droughts as the climate becomes increasingly arid (Seager et al. 2007, Karl et al.

2009). Should no actions be taken to implement sustainable practices for managing on the water supply, substantially less water providing for the needs of an increasing population in the region will likely have disastrous consequences.

By understanding the impacts of even small changes in the projected trend of precipitation, our ability to assess the future of water resource management improves dramatically. This information communicates the threat of continued unsustainable water usage, especially in highly vulnerable areas and communities, in order to encourage and promote sustainable practices. The results of this study will prove invaluable in assessing future needs for adaptation to climate change. The distribution of vulnerability is highly imbalanced; the groups most vulnerable to the impacts of a changing climate tend to be impoverished or developing countries and communities, minorities, and women (Turner et al. 2003, Solomon et al. 2007). Need-based science is becoming increasingly significant for scientists in the climatology field, and identifying the areas and communities most in need of rigorous efforts in water resource planning is a task that involves the cooperation of both physical and social scientists. The wide scope of the issue makes water resource planning both incredibly challenging and highly relevant at this critical point transitioning to an uncertain future.

3.2   Sources of model bias

Climate models provide the basis for projections of future climate change, and the accurate prediction of precipitation patterns and variability is a primary concern for water management. However, models still face challenges in their ability to realistically simulate precipitation. Understanding these challenges and how they affect model output

is essential to improving the reliability of predictions using the model ensemble. This section will introduce known sources of model bias associated with the simulation of precipitation and provide a starting point for a deeper, critical inspection of the quality of the hydrological cycle in climate model simulations.

3.2.1   Quantifying uncertainty: internal versus model variability

Uncertainties in climate projections may be due to a number of factors which can vary not only with the variable, but also with the time projection and particular emissions scenario. It is important to be able to differentiate specific causes of uncertainty. There are three main types of uncertainties: internal variability (product of the natural fluctuations which occur in the absence of external forcing), the variability between models (with the same forcing, each model simulates different climate changes) and finally the variability among emission scenarios. Numerous studies have shown that these uncertainties can arise from uncertainties in initial conditions, observational data, model parameters and structural uncertainties resulting from the fact that certain climate processes are still not fully understood (i.e. Lin et al. 2008, Reichler and Kim 2008, Dominguez et al. 2010, Schaller et al. 2011, Blázquez and Nuñez 2012). Developing model quality metrics to handle the various types of uncertainty has been a topic of interest for the modeling community. Chapter 4 explores the application of weighting schemes to model ensembles and presents the results of applying an alternate method of calculating trends in precipitation.

3.2.2   Flux corrections

Early on, models faced difficulties in their development which causes their simulations to produce unrealistic data at the interface between atmospheric and ocean model components: the introduction of a surface flux imbalance can cause coupled GCM simulated variables to increase exponentially. In order to adjust the simulated state to one of realism, modelers introduced 'flux corrections' to the simulations (Solomon et al. 2007, section 1.5.3). These adjustments are essentially empirical corrections which cannot be justified on physical principles, and that consist of arbitrary additions of surface fluxes to heat and momentum in order to prevent the drift of the simulated climate away from a realistic state. The artificial nature of these corrections has raised concern in measures of model performance since they have been demonstrated to increase systematic biases by propagating errors to other climate fields (e.g Reichler and Kim 2008). While most models now apply parameterizations to perform necessary adjustments, certain models still employ the use of flux corrections at the air-sea interface (Dai 2006).

3.2.3   Parameterization schemes of moisture processes

There are a number of issues with the parameterization of precipitation within climate atmospheric models, specifically with convective precipitation and the cumulus parameterization scheme. Convective precipitation can occur in a number of different types of cumulus convective clouds, such as the deep cumulus cells which form near the ITCZ, the stratocumulus clouds in the subtropics, and the shallow cumulus clouds produced by trade winds (Wallace and Hobbs 2006). Each form of convective cloud has a unique structure and properties which are not fully described by a single parameterization

scheme. A range of different convective adjustment schemes have been developed, each based on an altered set of conditions for the formation of cumulus clouds. For example, the GFDL CM2.1 model parameterizes convection using the Relaxed Arakawa Schubert (Moorthi and Suarez 1992) in which cloud tracers detrain from convective updrafts to stratiform clouds, and the updraft detrainment scheme for the lower bound (Tokioka et al. 1988) in which convective momentum transport is represented by diffusion proportional to cumulus mass flux. Every method of parameterization has certain disadvantages; the schemes chosen by a particular model to parameterize precipitation will contribute to sources of bias in the simulations based on the set of assumptions and simplifications used in the parameterization.

3.3   Goals of the study

This chapter concludes the general background information regarding climate model simulation and the CMIP model ensembles. The following chapters will apply this knowledge to specific approaches for quantifying and improving climate model biases in simulated precipitation. Two methods are employed for testing model quality: the first uses simulation data produced from CMIP3 and CMIP5 model runs (obtained through the model data archives at the Program for Climate Model Diagnosis and Intercomparison (PCMDI) website, http://www-pcmdi.llnl.gov/) to calculate model output based on scenario simulations. This examination encompasses all relevant output variables which comprise the water budget within global climate models. The second uses simulation data produced by in-house runs of at atmospheric component climate model which is forced using output data from selected CMIP5 models. Since this project focuses on semiarid

36

regions, the analysis concentrates on the climate processes which are associated with these regions. The results of the study are applied in the formulation of a novel approach for ensemble averaging with bias correction with the intentions of improving the future projections of precipitation using global climate models.

CHAPTER 4

EXPLORING TECHNIQUES FOR CONSTRUCTING

CLIMATE PROJECTIONS

This chapter presents a proposed scheme for climate model ensemble averaging which has been developed as a bias correction for potentially improving the accuracy of future projections of precipitation. The study compares two methods of multimodel averaging based on the classically defined absolute and relative climate changes for the future projection of precipitation used in climate model prediction. The classical equal weight scheme estimates the trend by the simple arithmetic mean of the trends produced by the individual models. In the relative change scheme, the multimodel average of the percentage changes in precipitation is multiplied by the observed present climate to form the future projection; this method is equivalent to applying unequal weighting to the absolute change scheme which acts as a bias correction. Unlike other recently developed unequal weight schemes, the alternative scheme does not penalize a model with a greater bias by reducing the weight applied to it. Instead, the underlying philosophy is that a model that has a greater bias is as useful as other models except that it needs a greater bias correction which is facilitated by the unequal weighting. The feasibility of the alternative scheme is tested on the CMIP3 prediction of precipitation. It is found that the new scheme and the equal weight scheme do not produce radically different large-scale patterns of the trend. Nevertheless, notable differences emerge in the regional scales that may be large enough to have implications for local stake holders.

4.1   Introduction

The IPCC AR4 has adopted a simple scheme of "equal weighting" in producing the multi-model projection. Some attempts have recently been made to explore alternative schemes for multi-model averaging beyond equal weighting (e.g., Giorgi and Mearns 2002, Knutti 2010, Knutti et al. 2010), although a clear agreement has yet to emerge on the optimal scheme and its justifications. In general, these existing schemes construct the trend from the multi-model averaging of the absolute change, defined as "future minus present" in the model simulation. A lesser-used alternative is the relative change, defined as the absolute change divided by the present climate from the model simulation. This study aims to assess the feasibility of multi-model averaging of the projected precipitation based on the relative change. It will be shown that the adaptation of relative change is equivalent to a specific unequal weight scheme for the absolute change. The potential benefit of this type of unequal weighting will be discussed. The two schemes are tested on CMIP3 simulations of precipitation, chosen both for its importance to societal needs and for technical ease in computing the relative change.

4.2   Absolute change: discussion of equal and unequal weighting

4.2.1   The classical scheme

In the classical multi-model averaging used in most key assessments in IPCC AR4, equal weighting was applied to the trend produced by each model, defined by the absolute change,

$$T_j = C_{MOD21,j} - C_{MOD20,j}, \quad (4.1)$$

39

where the subscript "j" indicates the j-th model, and "MOD21" and "MOD20" indicate the simulated future and present climate. (The "21" and "20" nominally indicate 21st and 20th century. In our later analysis they correspond to 2080-2099 and 1980-1999, respectively.) Averaging was then performed over all N models to establish the multi-model mean of the trend,

$$T = \sum_{j=1}^{N} W_j T_j \ , \qquad\qquad (4.2)$$

where $W_j = 1/N$ for all j. The trend T is understood as a function of space and season but those additional indices are omitted for brevity. For example, the T for annual precipitation from CMIP3 can be found in Fig. 10.12 in Solomon et al. (2007). Since climate models represent the long-term net response of many scales of processes on a large-scale output, the most useful information can be gained by taking long-term averages of the data. This practice helps to minimize the uncertainty caused by sources of variability such as periodic cycles (e.g. diurnal or seasonal cycles), quasiperiodic patterns (e.g. the El Niño Southern Oscillation), and internal or model variability (details in section 3.2.1). Fig. 4.1 demonstrates how the long-term mean is utilized to calculate the trend in (4.1) for a particular variable. Using precipitation as an example, this trend represents the predicted change in precipitation attributed to the model forcing and not variability, given that the long-term means span adequate lengths of time. All long-term means calculated for this project use 20-year periods separated by 100 years (such as 1980-1999 and 2080-2099 for present and future means, respectively), which is a sufficient length of time for determining precipitation trends due to forcings in climate model simulations.
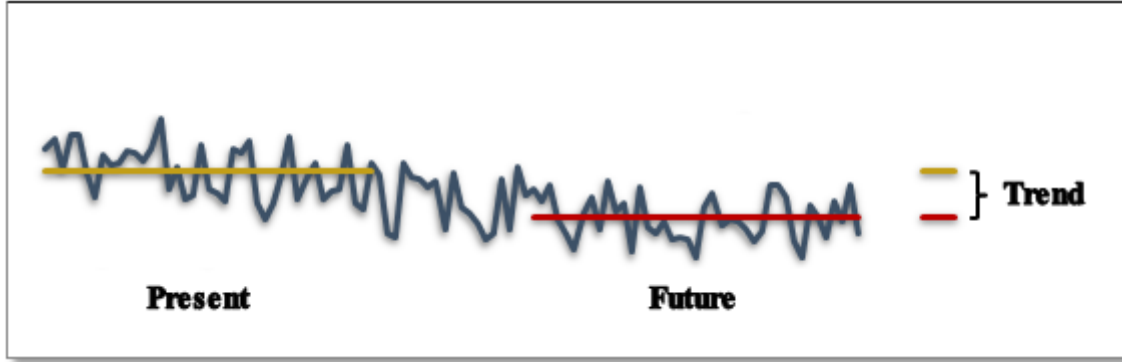
Fig. 4.1 An example of how the trend of a climate model variable is calculated using long-term means. The blue line represents the simulated output from a climate model. The gold and red lines represent the long-term averages calculated for a mean present (or past) state and a future state, respectively. The trend represents the difference (future minus present) between these two long-term averages.

By taking the sum of the trend given in (4.1) and (4.2) and the observed climate of the 20th century, the projected total climatology for the future is defined as,

$$C_{21} = C_{OBS20} + T . \qquad (4.3)$$

Keeping (4.3), one may consider two alternatives of C_{21} by (i) replacing the equal weight in (4.2) with $W_j = R_j/N$ where R_j depends on both T_j and the observed climate of the 20th century (and possibly the ranking of T_j in the multi-model ensemble, Giorgi and Mearns 2002), or (ii) replacing the T_j in (4.1) by a *relative change* to reconstruct T. The second case will be explored and shown that it is related to an unequal weight scheme in (i).

4.2.2   Unequal weighting and further motivation

For multi-model averaging of the absolute change, the simplest unequal weight scheme is to use only a subset of all available climate models (for instance, those in CMIP3) to construct the multi-model mean, essentially assigning a "zero" weight to the discarded models. This has been adopted by the recent USGCRP Report (Karl et al. 2008), in which only 15 of 21 CMIP3 models were used, based loosely on the reason that

the excluded models have lower resolution (footnote 93 in Karl et al. (2008)). One might also attempt to discard the outliers in the multi-model ensemble in order to reduce its spread, as there is evidence that it is too wide for CMIP3 models (Annan and Hargreaves 2010). However, recent hindcast experiments indicate that the mean of the entire multi-model ensemble generally outperforms that of a smaller subset (Reifen and Toumi 2009, Weigel et al. 2010). More generally, one can retain all models but assign a smaller weight to a model that produces a greater bias for present climate or a model that produces an outlier for the trend (Giorgi and Mearns 2002). The existing unequal weight schemes adopt the philosophy that a model which produces a greater bias is penalized with a reduced representation in the multi-model ensemble. As an alternative, the proposed method for ensemble averaging can function as bias correction which applies a heavier correction (instead of a smaller weight) to a model that has a greater bias. In that manner, democracy (word of Knutti 2010) is preserved even with unequal weighting. (The subtlety here is that the bias is estimated by the simulated *present climate* while for climate prediction the bias correction must be applied to the simulated *trend*.) This idea sets the tone for our later discussion on the adaptation of relative changes.

As previously discussed in Chapter 2, the North American summer monsoon exhibits diverse behavior in CMIP3; the region affected by this monsoon precipitation is of particular interest for our efforts. Fig. 4.2 illustrates the difference in model quality between two selected CMIP3 models. While the major features of monsoon rainfall was reproduced by the GFDL CM2.1 model (middle panel), the summer monsoon structure is almost non-existent in the IAP model simulation (bottom panel). For another example of

42
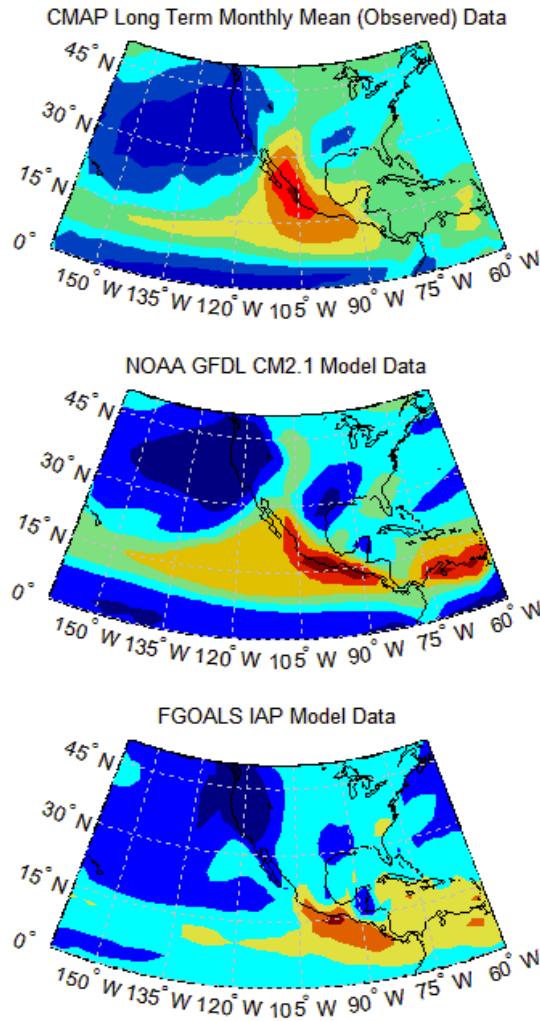
Fig. 4.2 North American Monsoon phenomenon from observation (top, using CMAP data for 1979-2000) and climate model simulations for present-day climate (middle: GFDL CM2.1 model; bottom: IAP model, both based on the 20C3M runs for CMIP3). Shown is the ratio of summertime precipitation to annual precipitation. The color interval is 0.1. Regions filled with deepest blue color are where the ratio is between 0 and 0.1; those filled with red/orange colors have the highest values of the ratio.

model disparity, Fig. 4.3a shows the area-averaged summer (July-September) precipitation versus the ratio of summer to annual precipitation for a box in the same region representing the Southwest U.S. (indicated in Fig. 4.5a) as simulated by CMIP3 models. The symbols with a black border are the 1980-1999 average from the 20C3M runs, and their counterparts with a gray border are 2080-2099 average from the SRES

43
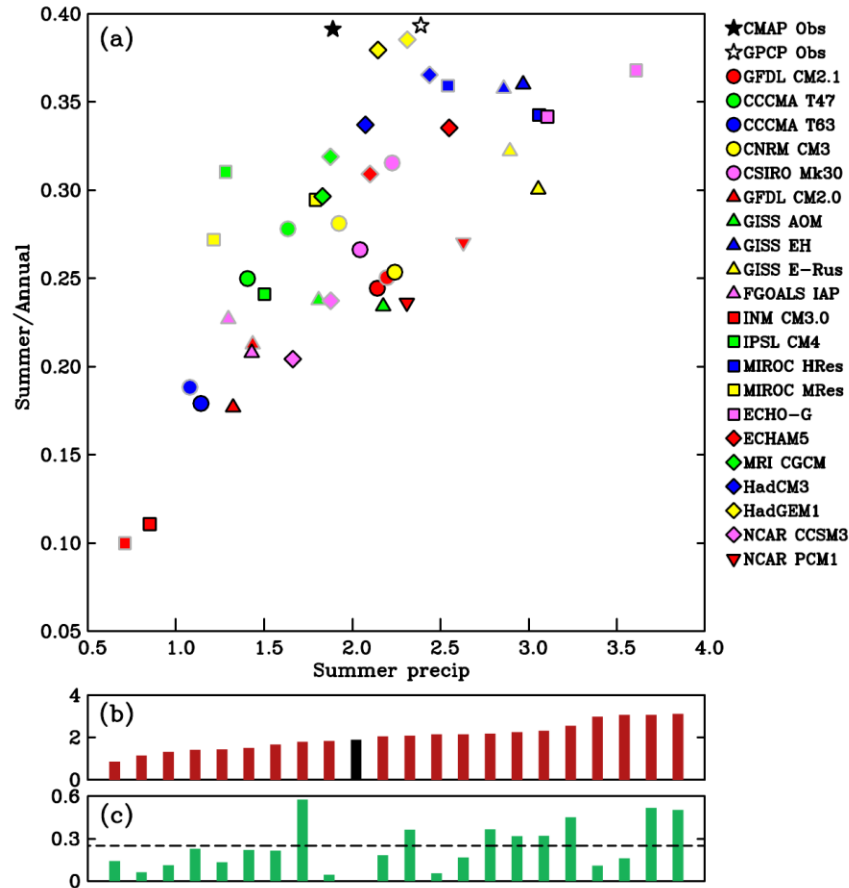
Fig. 4.3 (a) The summer (July-September) precipitation (abscissa, in mm/day) versus summer-to-annual ratio of precipitation (ordinate) simulated by the CMIP3 models listed at right. The symbols with a black border are the 1980-1999 mean from 20C3M runs, and their counterparts with a gray border are the 2080-2099 mean from SRES A1B runs. The observation for 1980-1999 from two data sets is shown: CMAP data is shown as the black star, and GPCP data is shown as the black hexagram. (b) The CMIP3 simulations of the 1980-1999 summer precipitation arranged with the driest model to the far left and wettest model to the far right. The length of each red bar indicates the amount of precipitation (in mm/day) simulated by a model. The black bar is CMAP observation. (c) The length of each green bar indicates the absolute value of the summer precipitation trend simulated by a CMIP3 model, corresponding to the red bar in Fig. 4.3b immediately above it. The dashed line indicates the multi-model mean of all green bars.

A1B runs. Also shown is the observation for 1980-1999 from two datasets: CMAP (Xie and Arkin 1997) as a filled black star, GPCP (Adler et al. 2003) as a black hexagram, for comparison purposes. The difference between CMAP and GPCP is small compared to the spread of the multi-model ensemble. CMAP is used for the ensuing analysis but the

conclusions are not sensitive to the choice of the observational dataset. For the summer precipitation, the multi-model distribution for the 20th century simulations is more centered around the observation; 9 models are drier and 12 models wetter than observation. For the summer-to-annual ratio, all CMIP3 models are biased to one side of observation (all models underestimate the ratio), which renders multi-model averaging less meaningful. Considering the better-behaved variable of seasonal precipitation, in Fig. 4.3b the models (length of red bar indicates amount of rainfall) are arranged from the driest at far left to the wettest at far right, with the black bar being the observation. The green bar in Fig. 4.3c indicates the magnitude (absolute value) of the trend in summer precipitation simulated by the model that is directly above it in Fig. 4.3b. The dashed line indicates equal weight multi-model ensemble mean of all green bars. Interestingly, the models that are too dry (those to the left of the black bar in Fig. 4.3b) in the 20th century also tend to produce a smaller trend in precipitation in the 21st century: 8 out of 9 of those models produce a green bar shorter than the ensemble average, in contrast to 5 out of 12 for the models that are too wet in the 20th century. Effectively, a model which produces too little rainfall for the 20th century also tends to predict a more muted response to greenhouse gas forcing in the 21st century. Assuming that the model predicted trends are as centered around the truth as their simulated 20th century climatology, a useful bias correction would be to amplify the trend produced by a model that is too dry, and tone down the trend produced by a model that is too wet in the 20th century.

4.3 Relative change and relation to unequal weighting

In the spirit of the discussion in section 4.2.2, it follows that the simplest scheme which uses relative change will replace the T in (4.3) by

$$T_{NEW} \equiv C_{OBS20} \times P , \qquad (4.4)$$

where

$$P \equiv \frac{1}{N} \sum_{j=1}^{N} P_j , \qquad (4.5)$$

$$P_j \equiv \frac{T_j}{C_{MOD20,j}} \qquad (4.6)$$

is the *relative change* of a climatic variable predicted by the j-th model. That is, the multi-model trend is defined as the observed present climate times the averaged percentage change predicted by the models. To compare this method to the weighted average of absolute changes, by expanding (4.4) we obtain

$$T_{NEW} \equiv \sum_{j=1}^{N} W_{NEW,j} T_j , \qquad (4.7)$$

where

$$W_{NEW,j} = \frac{1}{N} \left(\frac{C_{OBS20}}{C_{MOD20,j}} \right). \qquad (4.8)$$

Thus, by considering the multi-model average of relative changes, we essentially modify the equal weight $1/N$ commonly used in literature by multiplying it by a factor of $R_j = C_{OBS20}/C_{MOD20, j}$. Using Fig. 4.3b as an example, R_j is the ratio of the length of the black bar (the observation) to the length of the red bar for a given model. A perfect model has $R_j = 1$. If a model is too dry, i.e., it produced too little rain for the 20th century climate, it has $R_j > 1$, while a model that is too wet has $R_j < 1$. This design is meaningful

since, as demonstrated by Fig. 4.3c, the models which are too dry in 20th century also tend to predict a muted response (can be an increase or decrease) in precipitation to greenhouse gas forcing in the 21st century. The factor R_j serves to enhance the predicted trend for those models. For the models which are too wet, R_j acts the opposite way to tone down the predicted trend. Thus, the unequal weighting potentially serves the purpose of bias correction for the simulated trend as envisioned in section 4.2.2.

Our formula has restrictions. It is applicable only to a positive definite quantity like precipitation. Moreover, not every climatic variable possesses the relation shown in Figs. 4.3b and 4.3c between the magnitude of the simulated present climatology and that of the simulated trend. The presence of $C_{MOD20, j}$ in the denominator of the unequal weight might raise the concern that the scheme will become more singular over the regions where some models produce a very small amount of climatological precipitation. The examples which immediately follow should help ease this concern.

4.4   Results and discussions

Fig. 4.4 shows the projected trend, defined as the multi-model average of 2080-2099 minus 1980-1999 climatology, of annual precipitation from CMIP3 models based on the equal weight scheme (Fig. 4.4a) and the scheme using relative change (hereafter called the "unequal weight scheme") (Fig. 4.4b). Fig. 4.4a is constructed entirely from CMIP3 model simulations while Fig. 4.4b incorporated the observation (needed for constructing the unequal weight) for 1980-1999, which is based on the gridded 2.5° x 2.5° CMAP data. The CMIP3 simulations are interpolated to the same grid as observation. (A linear interpolation is used to ensure that no spurious negative values of

precipitation are created at this step.) The ratio, $R_j = C_{OBS20}/C_{MOD20, j}$, is then calculated at each grid point for each model. Fig. 4.4a can be readily verified with Fig. 10.12 of IPCC AR4 (Solomon et al. 2007), which shows the familiar pattern of an intense increase of rainfall in the tropics, subtropical drying, and increased wetness in high latitudes. This large-scale pattern proves to be robust as it is also preserved in Fig. 4.4b, which confirms that the unequal weight scheme does not produce a radically different projection for global precipitation.
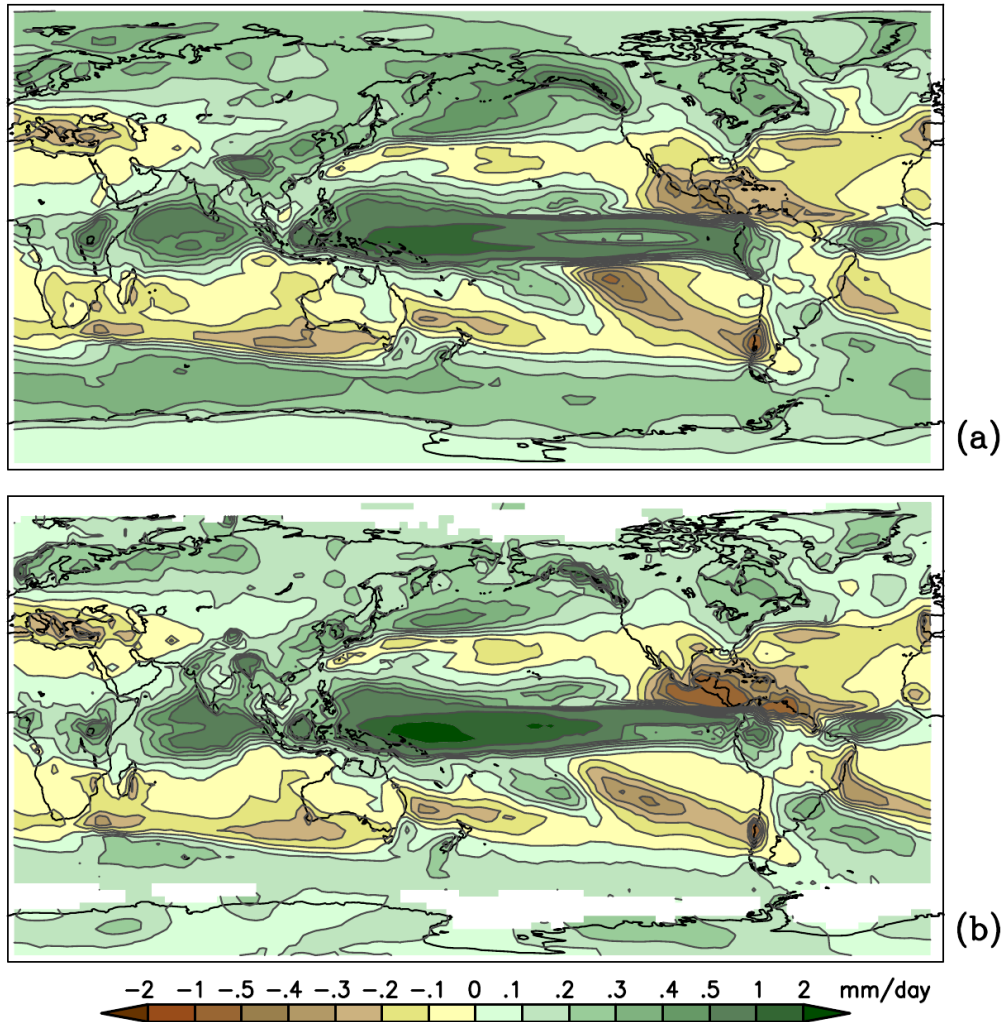
Fig. 4.4 The CMIP3 multi-model average of the trend in annual precipitation as estimated from the (a) equal weight, and (b) unequal weight, schemes. Color scale (mm/day) is shown at bottom. White areas indicate where observation data is missing.

While the two schemes lead to similar global-scale structures of the trend in precipitation, regionally they produce notable differences. (Since R_j is a function of space, the impact of unequal weighting varies from one region to another.) For example, Fig. 4.5a and 4.5b show the detail of the trend of annual precipitation for Western U.S. and Northern Mexico based on the equal and unequal weight schemes, respectively. While both indicate drying in the Southwest U.S. (Seager et al. 2007), with the unequal weight scheme the reduction of precipitation is projected to be less severe for Arizona but more severe for part of Texas. The difference between the two schemes can be seen in Fig. 4.6: for a majority of the region, the alternative scheme predicts more rainfall than the equal weight scheme (indicated by orange and yellow). Over the black box in Fig. 4.5a, the projected reduction of rainfall is 40 mm/yr from the unequal weight scheme, compared to 55 mm/yr from the equal weight scheme. This difference may be large enough to have implications for local stake holders.

Given the concern of a small denominator discussed in section 4.3, sensitivity tests were performed by imposing a criterion which places a cap on the allowable percentage change that a particular model may have for a particular grid point. This percentage is capped at 500%. The grid points which exhibit singular behavior (i.e., affected by the cap) only occur in the seasonal (summer and winter) projections. Since they are very rare (less than one per model, on average) and the same points are not shared by more than one or several models, it has been determined their overall effect on the ensemble average is negligible.

(a)　　　　　　　　　　　　　　(b)

(c)　　　　　　　　　　　　　　(d)

(e)　　　　　　　　　　　　　　(f)

−.4　−.3 −.25　−.2 −.15 −.1　−.05　0　.05　.1　.15　.2　.25　.3　.4　mm/day
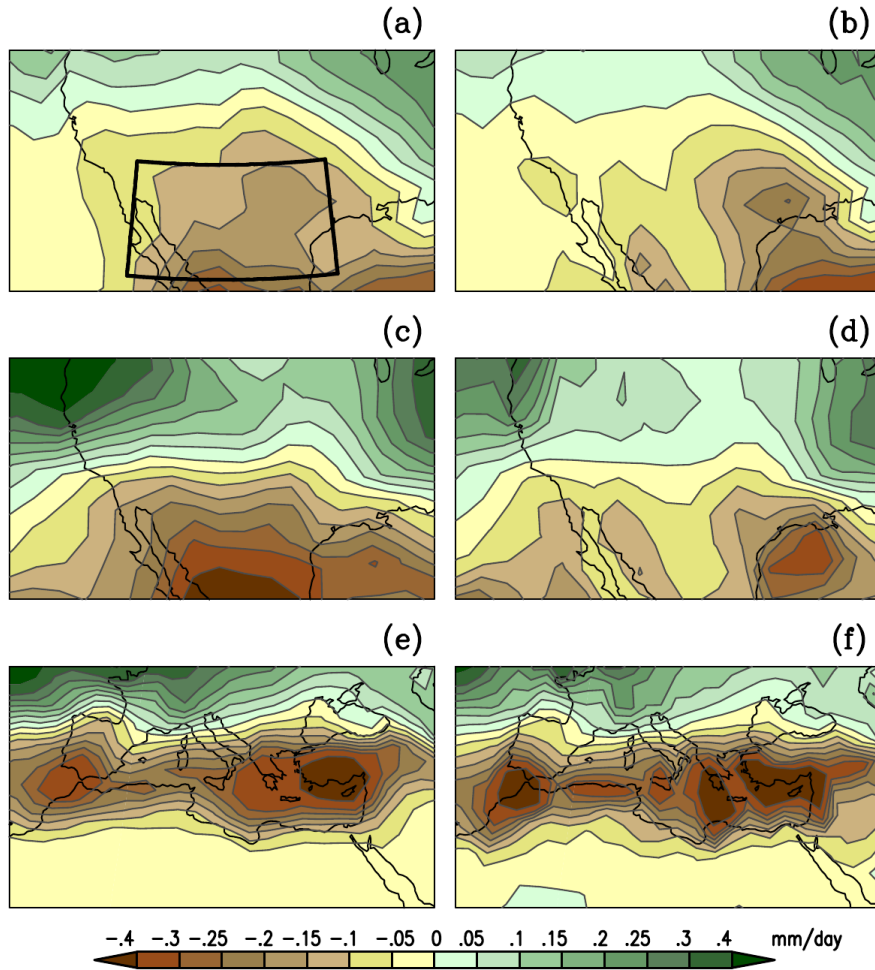
Fig. 4.5 (a) and (b) are similar to Figs. 4.4a and 4.4b but for the Western U.S. and Mexico region. Equal weight and unequal weight schemes are used for (a) and (b), respectively. (c) and (d) are similar to (a) and (b) but for the trend in winter (December-February) precipitation. (e) and (f) are similar to (c) and (d) but for the Mediterranean region.
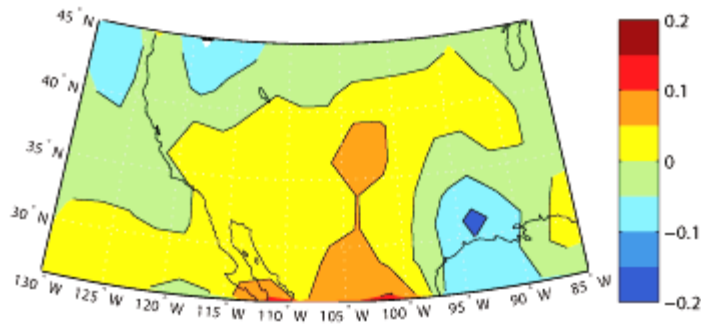
Fig. 4.6 The difference in the projected precipitation trend between the unequal weight and equal weight schemes (unequal – equal) in Fig. 4.5a and b for the southwestern US region. Yellow and orange areas indicate where the unequal weight scheme predicts a higher magnitude of the precipitation trend than the equal weight scheme.

To test if the unequal weight scheme remains stable for a shorter-term climatology of precipitation (when the problem with small denominator might become more severe), it is applied it to the summer (July-September) and winter (December-February) seasonal mean precipitation, also for CMIP3. Figs. 4.8a and 4.8b compare the equal and unequal weight schemes for winter, and 4.8c and 4.8d for summer. Figs. 4.8a and 4.8c can be verified with Fig. 10.9 in IPCC AR4 (Solomon et al. 2007). Just like the annual mean, the large-scale pattern of the trend produced by the unequal weight scheme is similar to its equal-weight counterpart. However, notable differences exist in the regional trend patterns. The trends in winter precipitation over the Western U.S. produced by the two schemes are compared in Figs. 4.5c and 4.5d. The shift of drying from Southwest U.S. to Texas produced by the unequal weight scheme is similar to the annual mean in Fig. 4.5b. Figs. 4.5e and 4.5f show the equal weight and unequal weight (relative change) results for the change in winter precipitation over the Mediterranean region. Just like Southwest U.S., the unequal weight scheme preserves the large-scale pattern but also leads to some differences in the regional detail of the change. The Mediterranean region experiences a strong seasonal influence of winter precipitation

51

from the Northern hemisphere midlatitude storm band. Previous evaluations of the hydrological cycle in this region indicate an atmospheric water deficit evident in observational datasets (Mariotti et al. 2002). This deficit is shown to be strongly correlated with the North Atlantic Oscillation (NAO). It has also been shown that the CMIP3 ensemble projects a drying trend for the Mediterranean region (Mariotti et al. 2008). The different processes which produce precipitation in this region make it another highly relevant choice for investigation. Our analysis showed that, for precipitation, the simple multi-model averaging of the relative change is a viable alternative to the classical equal weight scheme for the absolute change. Moreover, the former is equivalent to multi-model averaging of the absolute change using a specific set of unequal weight. Provided that a climatic variable exhibits a meaningful relation between the simulated 20th century climate state and the simulated trend as exemplified by Fig. 4.3b and 4.3c, the unequal weighting has the added meaning of bias correction for the trend. This relation has been tested for the precipitation over the southwestern US to serve as a motivation for developing the unequal weight scheme. A comprehensive analysis is necessary to determine if the relation is maintained globally and for other climatic variables. To improve on our prototypical scheme, one could design more complicated ways to extract the relation between the simulated present climatology and future trend (for example, by regressing the former on the latter and use the outcome to adjust the R_j factor). However, doing so would require the introduction of new assumptions since the truth of the future trend remains unknown. Additionally, the robustness of the scheme may be tested using the leave-one-out cross-validation method for evaluating unequal

52

weight schemes as suggested by Räisänen et al. (2010). The details of this study have been published in the Atmospheric Science Letters (Baker and Huang 2012).
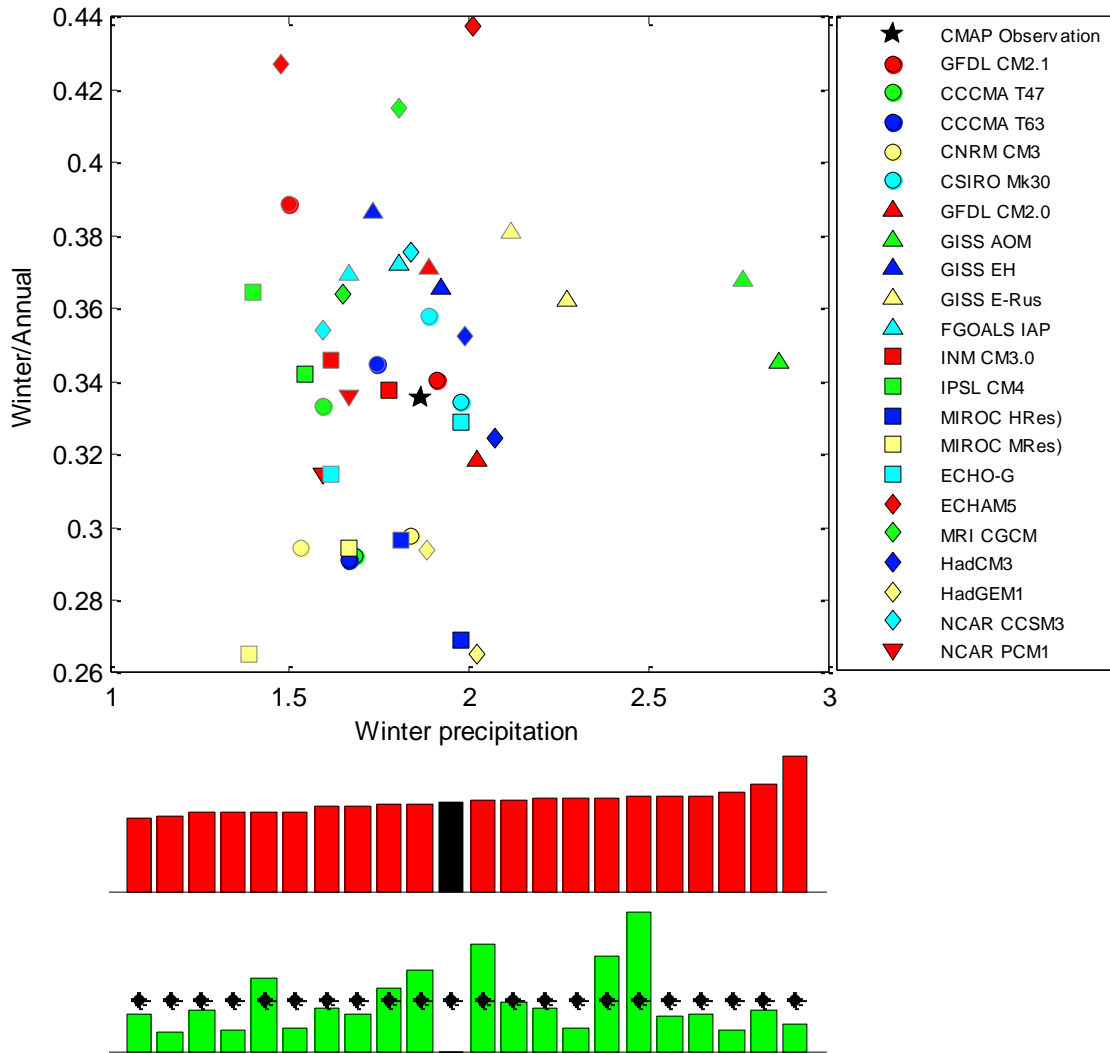
Fig. 4.7 (top) The winter (December-February) precipitation (abscissa, in mm/day) versus winter-to-annual ratio of precipitation (ordinate) simulated by the CMIP3 models listed at right for the Mediterranean region. The symbols with a black border are the 1980-1999 mean from 20C3M runs, and their counterparts with a gray border are the 2080-2099 mean from SRES A1B runs. The observation for 1980-1999 from CMAP data is shown as the black star. (center) The CMIP3 simulations of the 1980-1999 winter precipitation arranged with the driest model to the far left and wettest model to the far right. The length of each red bar indicates the amount of precipitation (in mm/day) simulated by a model. The black bar is CMAP observation. (bottom) The length of each green bar indicates the absolute value of the winter precipitation trend simulated by a CMIP3 model, corresponding to the red bar in the center panel immediately above it. The dashed line indicates the multi-model mean of all green bars.
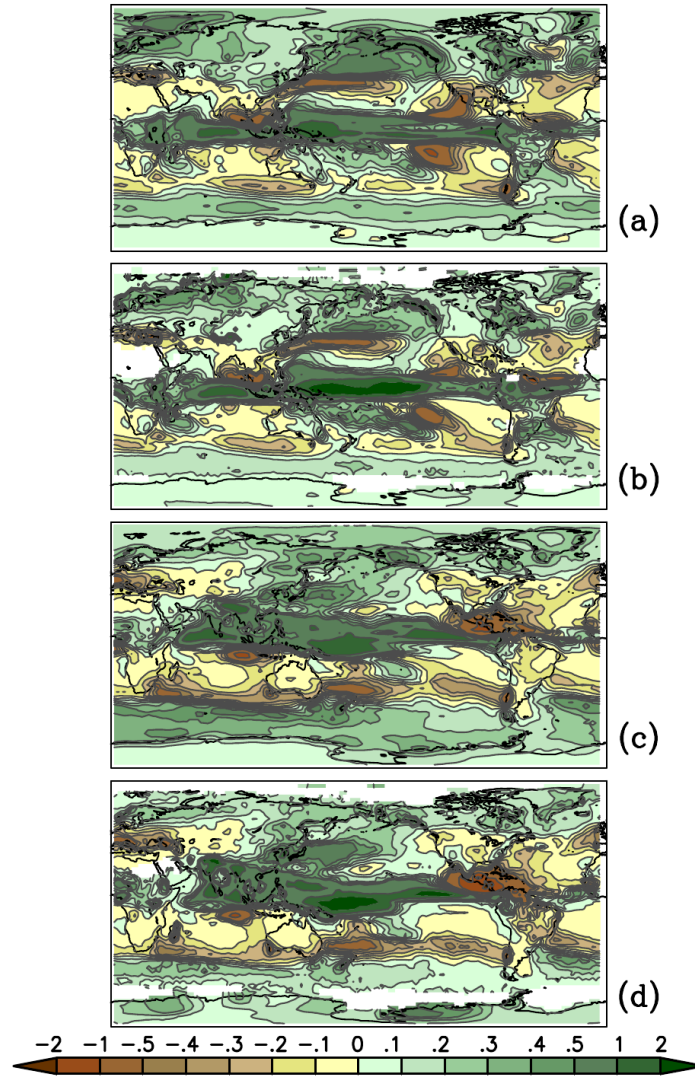
Fig. 4.8 Similar to Fig. 4.4 but (a) and (b) provide winter (December-February) and (c) and (d) provide summer (July-September) precipitation. (a) and (c) are based on the equal weight scheme and (b) and (d) unequal weight scheme. White areas indicate missing observation data.

CHAPTER 5

APPLICATION OF AN ALTERNATIVE METHOD FOR

ENSEMBLE AVERAGING CLIMATE MODELS

The alternative ensemble averaging technique proposed in Chapter 4 is demonstrated on the CMIP5 model archive for the simulated quantities of rainfall and evaporation. This technique is based on the application of an unequal weight to each model which is calculated as the relative change of the model simulation to observed climatology. The trend is calculated globally for each quantity between the model simulated future (21st century) and past (20th century) atmospheric conditions, and the unequal weight is applied to the trend for each model prior to ensemble averaging. The weight can vary both spatially and temporally, and it effectively serves as a bias correction for each model as it alters the trend based on error with observed climatology. This technique has been previously demonstrated on the older CMIP3 archive and compared with the more commonly used equal weight averaging scheme, and it was shown that notable regional differences emerge between the two schemes in the intensity of the projected trend in rainfall; these results are confirmed in the current study using the updated CMIP5 archive for both simulated rainfall and evaporation.

5.1   Introduction

Rainfall and surface evaporation play important roles in a regional water budget which can affect many aspects of human livelihood and the security of the water supply. Climate models attempt to predict possible changes in these quantities with simulations which estimate future conditions, and the predictions made by each model are averaged together for producing climate projections for chief scientific reports such as the Intergovernmental Panel on Climate Change (IPCC) assessment report (AR) 4 (Solomon et al. 2007). The current group of coupled general circulation climate models have produced simulation data which are available in the CMIP5 (Climate Model Intercomparison Project 5) online archive, and these data will be used to formulate the projections which will be included in the upcoming IPCC AR5. The accuracy of these projections is essential since many community managers around the world rely on information from scientific reports for planning regional water resource management and preparation for extreme events. The projections in these reports are typically produced by giving each model an equal weight in the ensemble average. However, it has been well-demonstrated that many biases exist within climate models, and models exhibit varying degrees of skill in reproducing climate processes; for example, early analysis of the CMIP5 archive reveals a tendency of most models to overproduce annual mean precipitation trends (van Oldenborgh et al. 2013) and models exhibit a large spread in reproducing global monsoon area, precipitation, and intensity (Hsu et al. 2013). The models are not unique samples in a set, since the genealogy of the newest archive reveals that many models share considerable amounts of code, thus compounding the ensemble occurrences of certain model biases (Knutti et al. 2013). The idea of implementing

alternative methods for climate model ensemble averaging has been explored and demonstrated through various techniques such as using unequal weights (e.g. Xu et al. 2010) or calculating the ensemble average using only a subset of models (e.g. Lee and Wang 2012). Each method for ensemble averaging has inherent strengths and weaknesses based on the qualitative selection of model weights, and these methods may not fully incorporate the knowledge of model bias. With the motivation of producing more accurate climate projections by using observed climate conditions, an alternative ensemble averaging technique was presented by Baker and Huang (2012) and demonstrated on the previous CMIP3 model archive for the simulated trends in precipitation. It was shown that the alternative unequal weight technique produced reasonable global patterns of rainfall which did not dramatically differ from those produced using the equal weight averaging method. However, the projected regional intensity of rainfall produced by the alternative technique differed from the equal weight method enough that the changes could be significant for managing water resources. These findings indicated that the alternative technique, with its bias-corrected ensemble average trend, may be a viable option for producing ensemble averaged regional projections of certain meteorological quantities using model simulation data. For further demonstration of method feasibility, the alternative technique has been applied to an additional important climatological variable (surface evaporation) and computed for both evaporation and rainfall using data from the newest climate model archive, CMIP5. This study presents the global projections produced using both the alternative and the classical ensemble averaging techniques for each quantity with highlighted selected regions for comparison.

57

5.2   Approach and averaging techniques

5.2.1   Model data

Simulation data from 37 models in the most recent CMIP5 archive are used for demonstrating the ensemble averaging technique. All selected models represent the set of coupled general circulation models with currently available data for the chosen quantities of precipitation and surface latent heat flux; these models are listed in Table 2.3. Documentation and data access for the models can be obtained from the PCMDI website at http://cmip-pcmdi.llnl.gov/cmip5/. Archive designated 'historical' runs of monthly averaged data have been selected for values corresponding to *20th century* (chosen as a 1980-1999 time set) to represent the simulations forced only by observational data. The 20th century values will be used as a basis for comparison with the *21st century* (2080-2099) values which are obtained from the selected 'RCP 4.5' simulation runs of monthly averaged data forced using the corresponding representative concentration pathway (RCP) scenario of greenhouse gas (GHG) emissions, as detailed by Taylor et al. (2012). The long-term difference of 100 years between epochs is chosen to help isolate the model response to the scenario forcings. Observational data are also selected for precipitation as the GPCP (Global Precipitation Climatology Project) version 2.2 dataset (Adler et al. 2003) and for evaporation as the NCEP-DOE (National Centers for Environmental Prediction and the Department of Energy) Reanalysis 2 dataset (Kanamitsu et al. 2002) for the 20th century time set. All model data are interpolated to a T62 Gaussian grid prior to analysis.

5.2.2   Methodology

This study analyzes the atmospheric response to future GHG emissions with simulation data from the CMIP5 model archive by computing the trend for each model for selected quantities. Following the methodology described in Chapter 4, the trend is defined as the difference between the 20-year averaged time sets taken from model simulations, $T_j = C_{MOD21,j} - C_{MOD20,j}$ in which the subscript "j" indicates the j-th model, and "$MOD21$" and "$MOD20$" indicate the model simulated time sets corresponding to 21st and 20th century climate for the selected quantity C. The trend is then ensemble averaged for all models to produce a projection for each quantity. Two methods of ensemble averaging are discussed and demonstrated in this study for comparison. For the classical equal weight scheme, the ensemble average trend of N models is defined by equation (4.2) in which the weighting factor $W_j = 1/N$ for all j. This ensemble averaging method is typically used in climate projections such as those included in the IPCC assessment reports (Solomon et al. 2007). However, the weighting factor treats all models equally in the ensemble average; knowledge of model bias is not incorporated into the projections. As an alternative technique to the equal weight scheme, this study demonstrates an unequal weight method in which the ensemble average trend is defined by equation (4.7) in which the new weighting factor $W_{NEW,j}$ is the weight $1/N$ multiplied by a factor of $R_j = C_{OBS20}/C_{MOD20,j}$. (See Baker and Huang (2012) or Chapter 4 for a complete derivation). This alternative technique was successfully demonstrated on the previous CMIP3 archive with significant regional differences in average projected rainfall. As an update to that study, this chapter presents the extension of the technique to the updated CMIP5 archive and for an additional climatological variable of evaporation.

5.3   Results and discussion

5.3.1   Global trends

To examine the effects of the alternative averaging technique on global trends of rainfall, Fig. 5.1 shows the annual ensemble average calculated using both the alternative technique (a) and equal weight method (b). Fig. 5.1(b) can be compared with the results from Lee and Wang (2012) which use a subset of CMIP5 models and show similar results in the general pattern of future precipitation trends. Increased radiative forcing due to GHG-related climate change is projected to produce wetter conditions in the tropics and high latitudes and drier conditions in the midlatitudes (Solomon et al. 2007). The global structure of the rainfall trend in Fig. 5.1 supports this projection with a positive response near the tropics and a negative response in the midlatitudes. The use of the alternative technique does not change this overall pattern as shown in Fig. 5.1(a) as the projected conditions are indeed preserved in global structure. However, the differences between the two methods can be rather significant as seen in Fig. 5.1(c). Over tropical ocean areas, the unequal weight averaging method still shows a positive trend in precipitation, but it produces a more muted response over the Indian Ocean and muted patterns of drying and wetting over the south Pacific.

Increased radiative forcing also accelerates surface evaporation (Solomon et al. 2007), and Fig. 5.2 supports this projection with a nearly global positive trend in surface evaporation as calculated from model surface latent heat flux. The most notable difference between the global patterns of ensemble-averaged surface evaporation trend as seen in Fig. 5.2(c) is in the stronger signal of increased evaporation predicted by the unequal weight method over most land surfaces in the northern hemisphere.
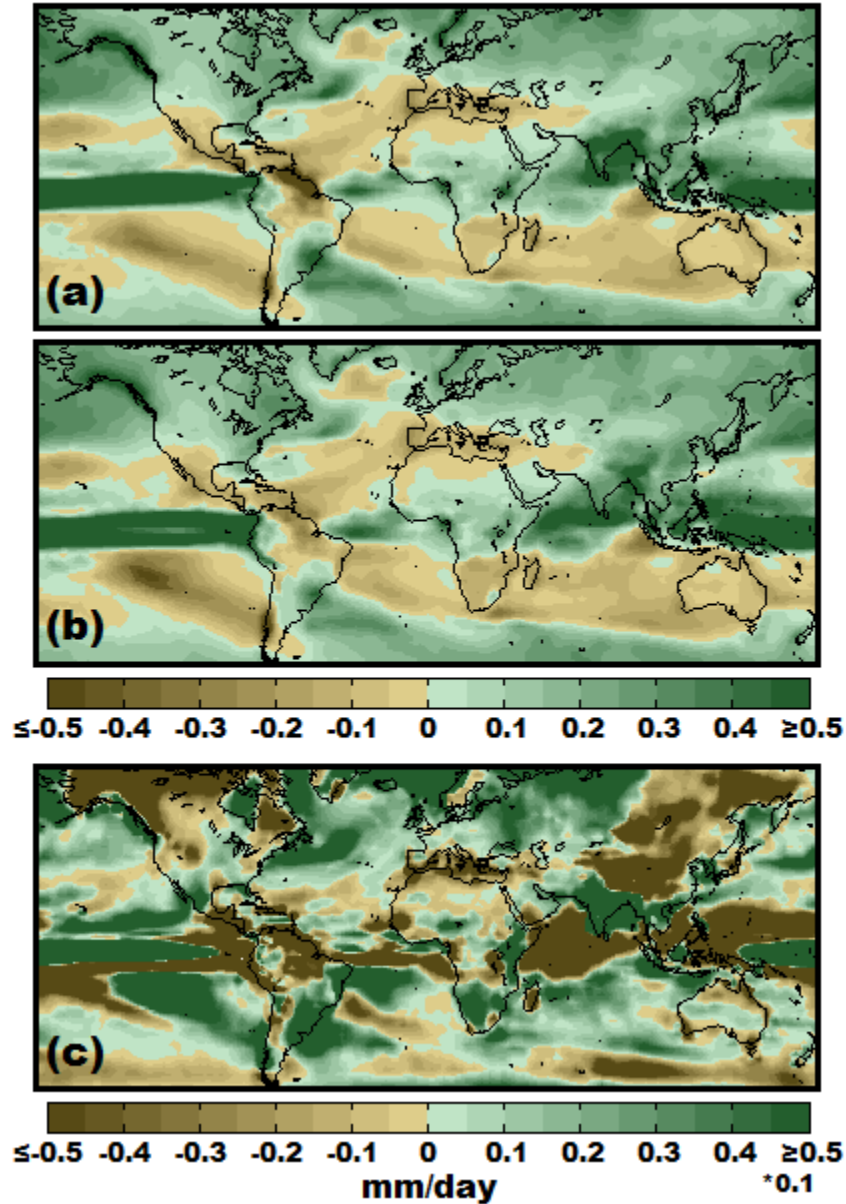
Fig. 5.1: Ensemble average annual trend in global precipitation from 21st century (2080-2099) minus 20th century (1980-1999) means for (a) unequal weight and (b) equal weight averages in mm/day. Panel (c) represents the difference between the two averaging methods (a) minus (b) in 0.1 mm/day. Green colors represent projected surface wetting trends (precipitation trend > 0), brown colors represent projected surface drying trends (precipitation trend < 0).
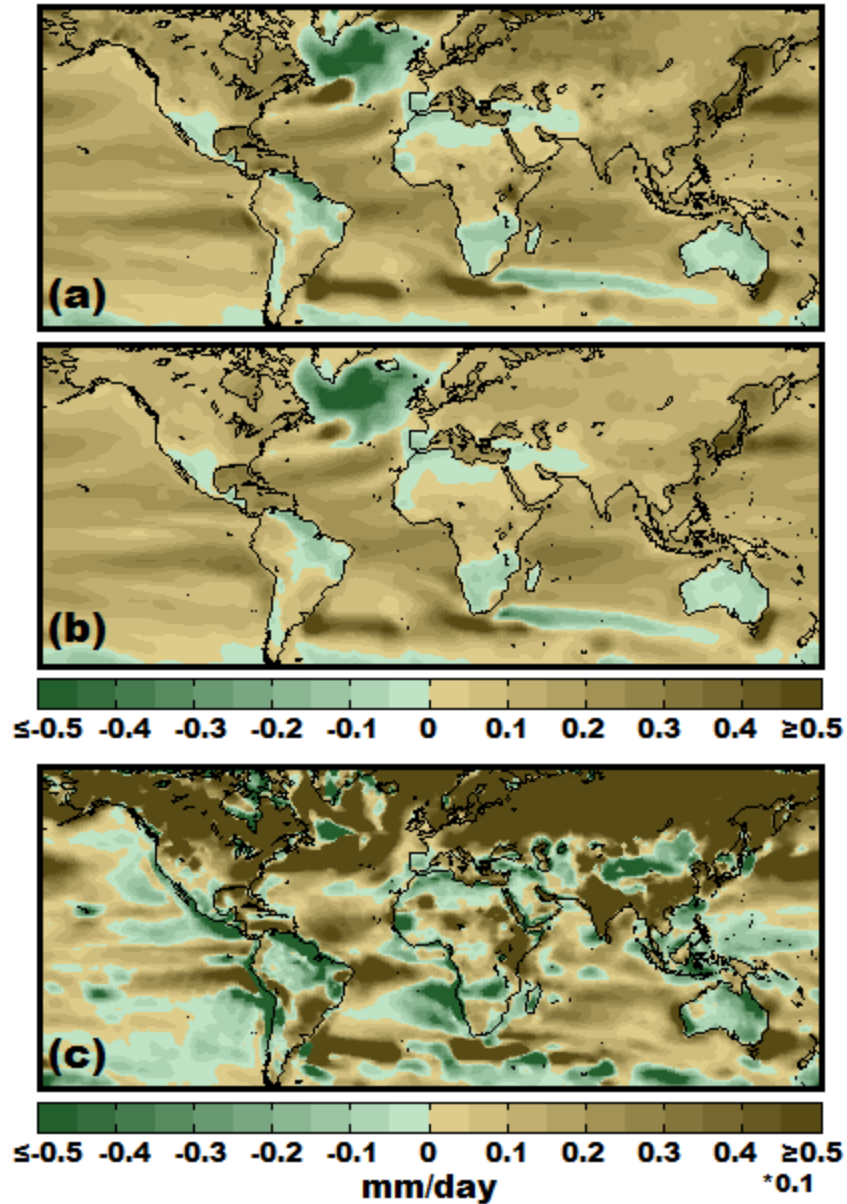
Fig. 5.2: Same as Fig. 5.1 but for the annual trend in global evaporation. Green colors represent projected surface wetting trends (evaporation trend < 0), brown colors represent projected surface drying trends (evaporation trend > 0).

The trends in global precipitation and evaporation averaged zonally to produce meridional cross-sections can be viewed as the consequences of the changes in poleward moisture transport. Fig. 5.3 depicts the seasonal-mean 21st minus 20th century trend in precipitation for both ensemble averaging methods, and the results can be confirmed with

Lau et al. (2013). A strong positive signal of increased precipitation in the tropics for all seasons is evident in the zonal average trend, with the most pronounced increase occurring in March-May. Zonal averages show a negative trend in precipitation for northern hemisphere (December-May) and southern hemisphere (all seasons) midlatitude regions. The differences between the unequal weight and equal weight ensemble averaging methods are most pronounced from December to May in the tropics in which the alternative unequal weight technique adds an even stronger precipitation response to GHG forcing, indicating that the CMIP5 ensemble tends to under produce tropical precipitation during these seasons. The zonally averaged seasonal mean evaporation trends in Fig. 5.4 are dominated by ocean responses to GHG forcing in the southern hemisphere since the evaporation over ocean areas greatly surpasses that from land surfaces, with a nearly globally positive trend in evaporation in all seasons and the largest positive evaporation trends occurring in the winter seasons for northern hemisphere (DJF) and southern hemisphere (JJA). It is notable that the unequal weight method produces ensemble averages with more pronounced positive signals during the winter seasons for both hemispheres, indicating that the CMIP5 models also tend to under reproduce ocean evaporation. In general, the alternative technique highlights ensemble deficiencies in producing poleward moisture transport processes and corrects for these biases accordingly.
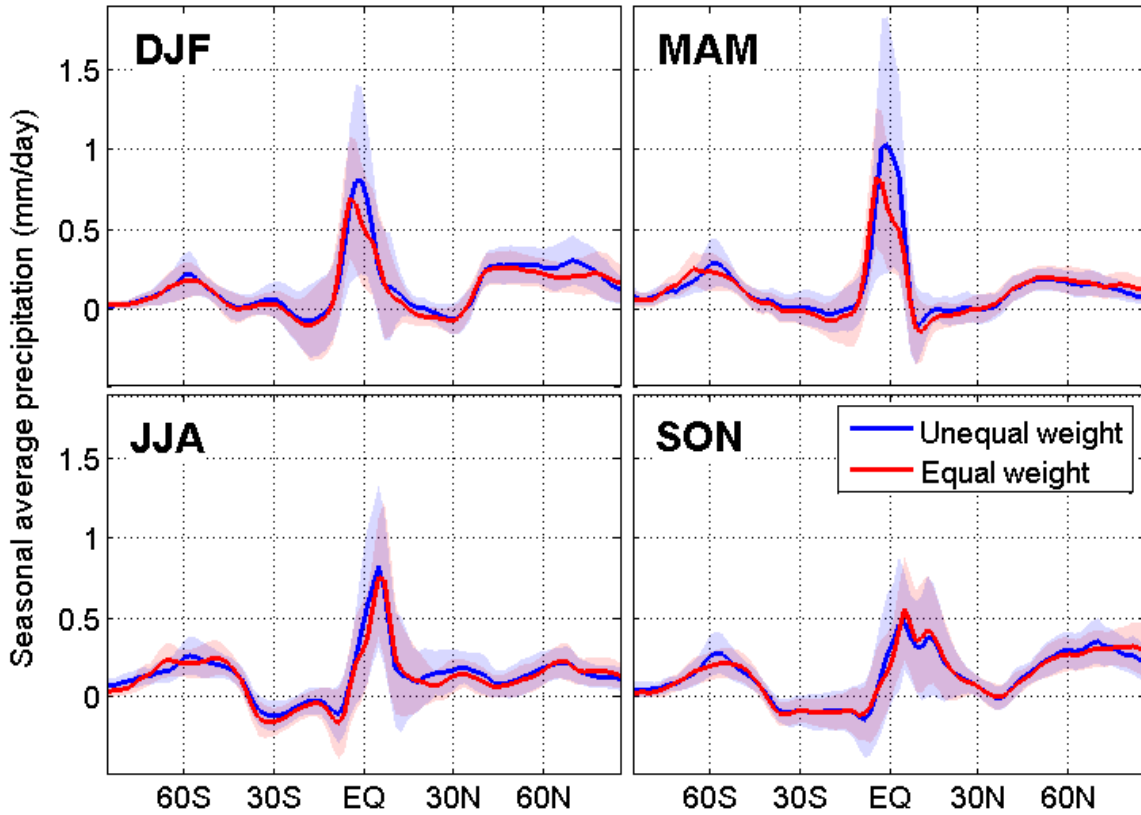
Fig. 5.3: Zonal mean global precipitation trends taken for the same 21st century minus 20th century temporal averages of DJF (December-February), MAM (March-May), JJA (June-August), and SON (September-November) seasonal means for unequal weight (blue) and equal weight (red) ensemble averages in mm/day. Shaded areas indicate ensemble standard deviation error bars for each method.
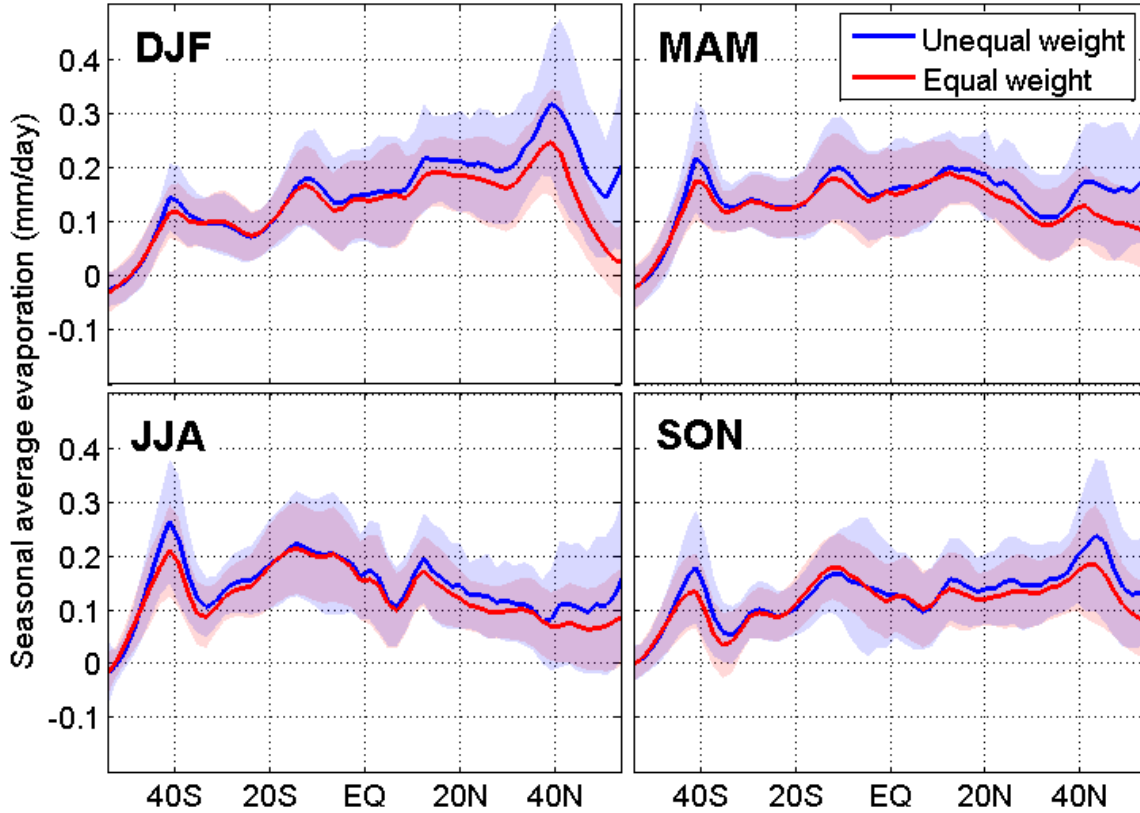
Fig. 5.4: Same as Fig. 5.3 but for zonal mean global evaporation trends.

5.3.2   Regional trends

Regional differences in projected rainfall and surface evaporation trends demonstrate the impacts of the averaging method on land surfaces as seen in Fig. 5.5 and 5.6. The southwestern United States is a particular region of concern regarding water availability, and projections for this region show a future decline in available surface water (Seager et al. 2012). The unequal weight method also predicts a decline in precipitation for this region, but the response is more muted with a rainfall trend up to 10-20 mm/year higher than the trend predicted by the equal weight average as seen in Fig. 5.3(c). The northern US, by contrast, is projected to have increased rainfall and increased surface evaporation for the 21st century (Fig. 5.3(b) and 5.4(b)), but the unequal weight

method projects much drier conditions of up to 60 mm/year less than the equal weight average with less intense rainfall and more intense surface evaporation.

The Mediterranean region also falls within a midlatitude band expected to experience drying in the 21st century as confirmed by initial analysis of the CMIP5 ensemble, although the ensemble tends to demonstrate an underrepresentation of the seasonal cycle amplitude (Kelley et al. 2012). Fig. 5.5(f) shows that the unequal weight method corrects for this bias by predicting an increased drying trend of up to 80 mm/year less annual rainfall than the equal weight average. More intense evaporation is also projected using the unequal weight method for most land surfaces in the region (Fig. 5.6(f)). The alternative technique produces significant enough differences that the results could be critical for planning 21st century water management in the Mediterranean region.

The Asian summer monsoon is an important climatological phenomenon for the region selected in Fig. 5.5 and 5.6 (g-i). Initial comparisons of late 20th century simulations of the Asian monsoon between CMIP5 and its CMIP3 predecessor show ensemble improvements in all tested quantities, but systematic errors are still present in both ensembles (Sperber et al. 2012). A majority of the annual precipitation for the region comes from the summer monsoon, so the annual trend is also indicative of the trend in the summer monsoon. The difference in ensemble averaging methods shows that the unequal weight method projects the Asian monsoon region to receive even more intense rainfall and surface evaporation in the 21st century, predicting up to 120 mm/year more precipitation than the equal weight average over the Indian peninsula. The accelerated

66

hydrological conditions due to GHG forcing of both surface evaporation and rainfall are projected to become more intense for this region due to the relative change in trends.
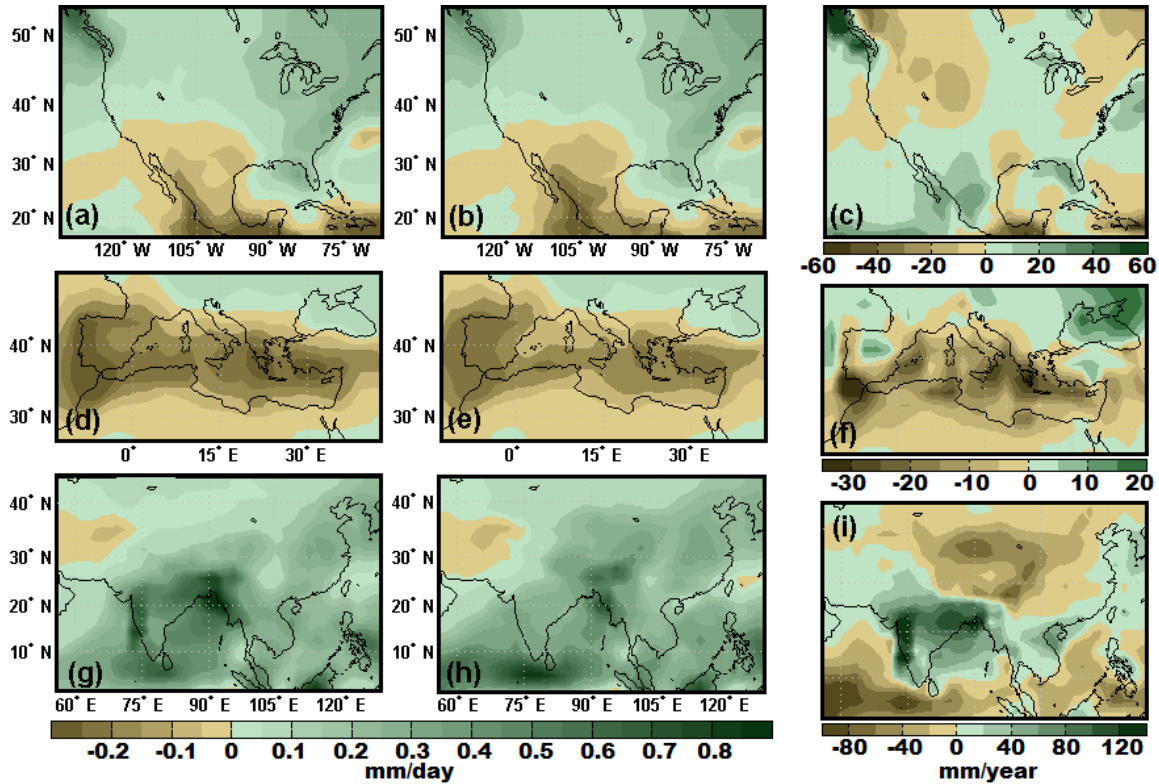
Fig. 5.5: Ensemble average annual trend in precipitation for selected regions from 21st century (2080-2099) minus 20th century (1980-1999) means for unequal weight (a, d and g) and equal weight (b, e and h) averages in mm/day. Panels (c, f and i) represent the difference between the two averaging methods for each region in mm/year. Green colors represent projected surface wetting trends (precipitation trend > 0), brown colors represent projected surface drying trends (precipitation trend < 0).
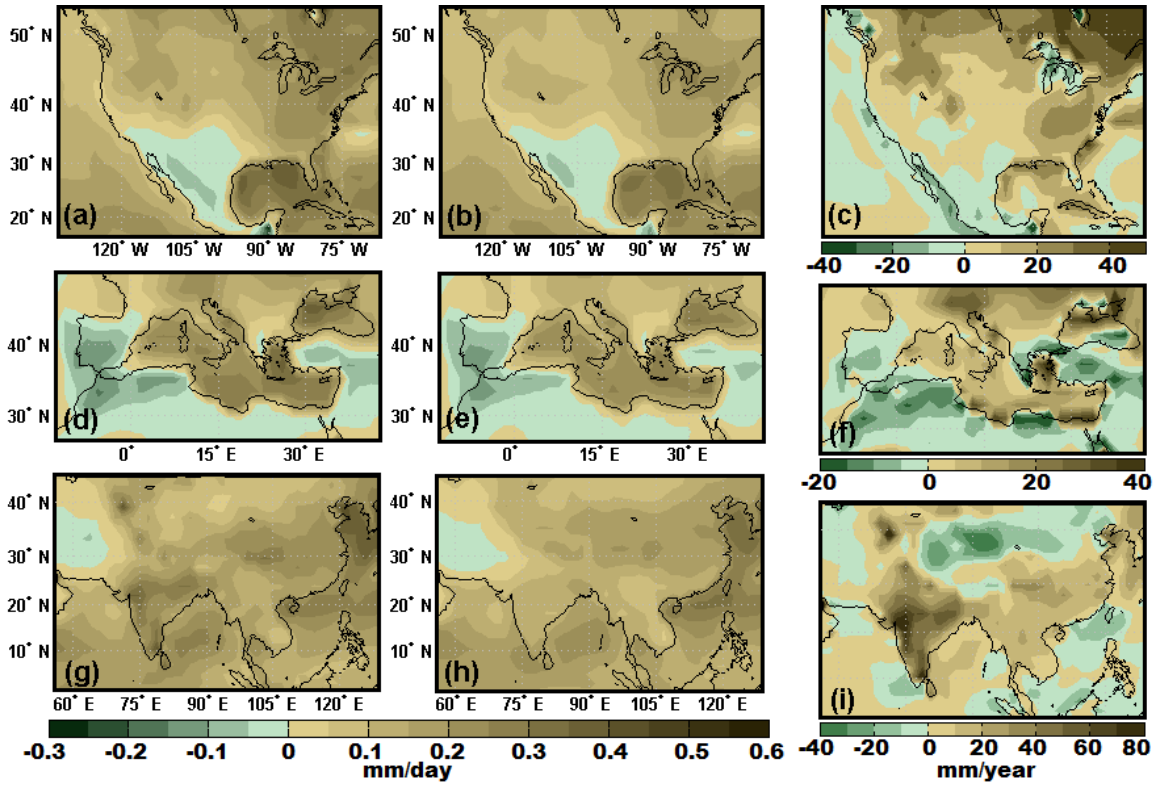
Fig. 5.6: Same as Fig. 5.5 but for the annual trend in evaporation. Green colors represent projected surface wetting trends (evaporation trend < 0), brown colors represent projected surface drying trends (evaporation trend > 0).

5.4   Conclusions

This study exhibits how an alternative ensemble averaging technique can produce regionally significant differences from the commonly used equal weight average for climatological quantities which are important to human life. While the updated CMIP5 archive has been shown to improve over CMIP3 in reproducing many processes and conditions of observed climate, known biases still exist, and the construction of ensemble averages using unequal weight methods which consider model bias can be considered a viable option. The alternative technique demonstrated in this study is presented as one

such option for analyzing simulation data coupled climate models with the intention of considering known model bias in formulation of climate projections.

CHAPTER 6

COMPARING PERFORMANCE OF MODEL ENSEMBLES

This investigation delves into the quality of the water cycle in global climate models by examining multiple terms of the moisture budget in the most current CMIP5 and the previous CMIP3 model archives. The two multimodel ensembles are compared by analyzing the seasonal simulated precipitation P, evaporation E, and $P - E$ terms for each model and verifying the results with selected observational datasets. Inspection of complementary moisture variables enhances the understanding of both individual model and ensemble deficiencies in predicting regional water availability, and a comparison of the model quantities with observational data provides a better evaluation of model quality in simulating the global water cycle. This study focuses on the semiarid Mediterranean and southwestern US regions, comparing the quality of the model ensembles for these regions which have a particular sensitivity to changes in water availability for critical resource management. It is found that the ensembles produce similar seasonal cycles for both regions, with CMIP5 exhibiting no statistical reduction in spread from its CMIP3 predecessor for regional season-averaged P, E and $P - E$. Both ensemble average simulated (future – past) trends (calculated using RCP 4.5 and historical runs for CMIP5 and SRES A1B and 20C3M runs for CMIP3) predict a negative trend for the southwestern US and a strong negative trend for the Mediterranean region in annual $P - E$, with notable seasonal variations between the two archives. Higher resolution CMIP5 models do not perform significantly better than the ensemble average for any calculated quantity.

70

6.1   Introduction

Precipitation encompasses different phase states and convective properties and can exhibit intermittent behavior, making it insufficiently quantified by a single continuous value in the manner of temperature and other climate variables. These uncertainties make model precipitation a particularly challenging quantity to correctly simulate in climate models (Solomon et al. 2007, Ch.3 Sec.3). In order to understand possible contributing sources of bias in model simulations, examining multiple quantities of the moisture budget is one possible method of determining the source of model precipitation trends; for example, an increase in local precipitation could be identified as increased $P - E$ or decreased evaporation. These terms can be evaluated using the mass conservation equation for water vapor in the atmosphere: for long-term averages, vertical integration with respect to pressure of the water vapor balance equation combined with mass continuity leads to $-\nabla \cdot \vec{Q} = P - E$, where P is precipitation, E is evaporation, and the quantity $(-\nabla \cdot \vec{Q})$ is the moisture convergence in the atmosphere. Previous work has incorporated the analysis of complementary moisture variables when assessing climate model projections of precipitation: Seager et al. (2013) examined model projected 21st century $P - E$ for the southwestern US region, and Liepert and Previdi (2012) evaluated the global values of both precipitation and evaporation in the Coupled Model Intercomparison Project Phase 3 (CMIP3) archive. This study extends the analysis of the global moisture budget to the most current global climate model archive, CMIP5. The performance of the two model ensembles is compare using regional- and seasonal-averaged quantities of precipitation, evaporation, and $P - E$ computed for the selected southwestern US and Mediterranean semiarid regions. The long-term seasonal mean

values are calculated for each model from the CMIP3 and CMIP5 archives for both a past and future state, and the trends (future – past) are computed for the two chosen semiarid regions for each quantity P, E, and $P – E$. The same values produced using observational datasets are also included for comparison to provide a better understanding of ensemble behavior in reproducing present climate conditions and possible indications of the reliability of model projections.

Preliminary studies comparing the CMIP3 and CMIP5 model archives have found some improvements in precipitation uncertainties in the CMIP5 ensemble over its CMIP3 predecessor (Blázquez and Nuñez 2012; Kim and Yu 2012). This study endeavors to compare multiple quantities related to the moisture budget with an in-depth seasonal analysis, highlighting particular deficiencies in the model archives and giving a more complete understanding of future surface water availability in the selected semi-arid regions.

6.2   Methods and analysis

Selected for analysis are all available models in the CMIP3 and most current CMIP5 archives (see Chapter 2, Tables 2.2 and 2.3). For regional calculations, the climatological value represents an area-averaged long-term mean (abscissa, mm/day) which is plotted versus a ratio of the seasonal mean to the annual mean (ordinate) to demonstrate seasonal intensity. Past means represent a 1980-1999 average (shown in the scatter plots in Figs. 6.2, 6.4, 6.7, and 6.9), while trends represent a future (2080-2099) minus past mean (6.3, 6.5, 6.8, and 6.10). The southwestern US quantities are calculated as an area average over the box shown in Fig. 6.1a (30N – 40N, 120W – 95W) and

72
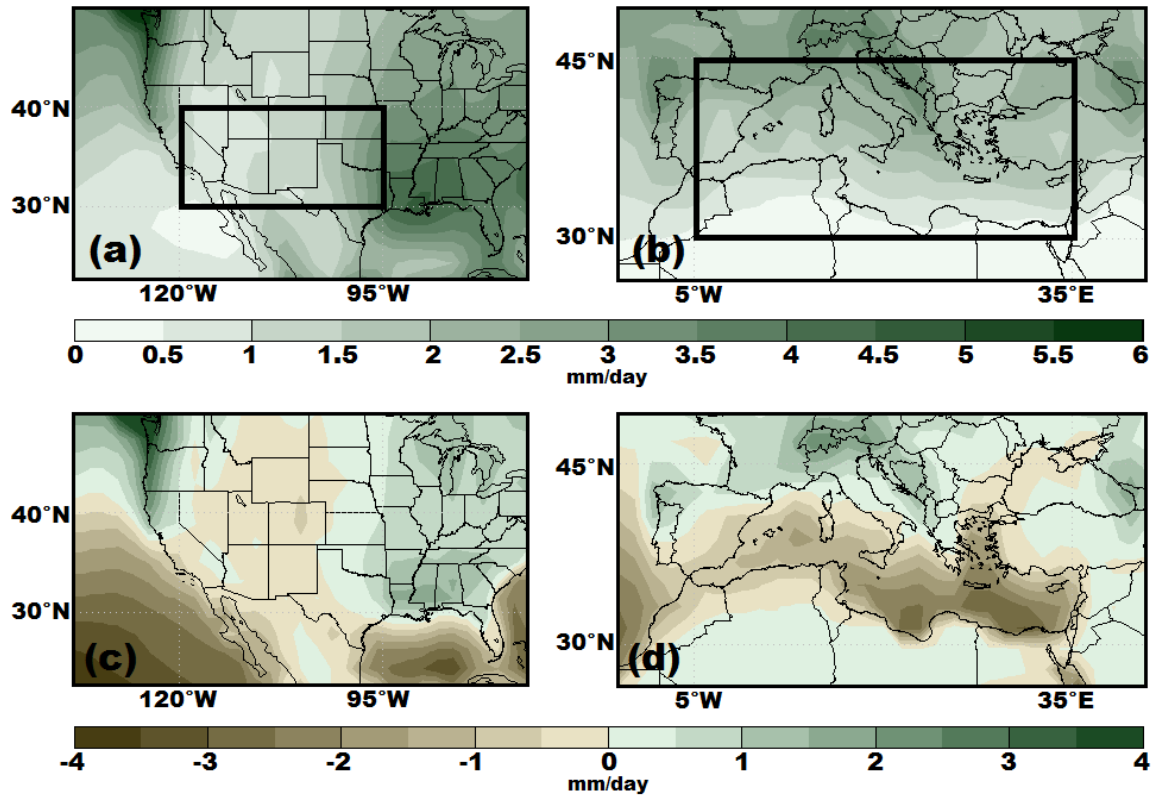
Fig. 6.1 The annual mean precipitation averaged 1980-1999 for (a) Southwest US, (b) the Mediterranean region. (c) and (d) are the counterparts of (a) and (b) but for precipitation minus evaporation. Precipitation is based on the GPCP data and evaporation the ECMWF-Interim reanalysis. Color scale is shown at bottom. The bold boxes in (a) and (b) indicate the regions over which area averaging is made to construct the scatter plots in Figs. 6.2-6.11.

Mediterranean region quantities are calculated for the box in Fig. 6.1b (30N – 45N, 5W – 35E) for all seasons. Also included for comparison are the same quantities calculated using four observational datasets: NCEP-DOE AMIP-II Reanalysis Global Precipitation (NCEP) (Kanamitsu et al. 2002), Climatology Centre (GPCC) Full Data Product version 5 (Schneider et al. 2008), CPC Merged Analysis of Precipitation (CMAP) (Xie and Arkin 1997), and European Centre for Medium-Range Weather Forecasts - ERA Interim (ECMWF) (Dee et al. 2011). The climatological annual mean values of precipitation and $P - E$ averaged for 1980-1999 using observational datasets for the selected regions are

shown in Fig. 6.1. These semi-arid regions are characterized by generally dry climates as a result of their mid-latitude positions which receive descending dry air from the northern hemisphere Hadley cell circulation (Solomon et al. 2007). The seasonal modeled and observed values for each region will be compared and discussed in the following sections.

6.3   Regional comparisons of ensemble quality

6.3.1   Southwestern US

As a basis for the examination of model bias, the southwestern US region provides a highly relevant starting point for regional analysis due to the diverse behavior of climate models in simulating its climatology. This region experiences strong annual rainfall contributions both from large-scale winter storm systems and from summer and early fall precipitation from the North American monsoon phenomenon. The most significant annual drying due to evaporation occurs in the hottest summertime months. Previous work (Baker and Huang 2012) demonstrated the ineffectiveness of the CMIP3 ensemble in generating summer precipitation for this region due to the large variation in model skill in reproducing monsoon activity. This paper further explores the North American monsoon by inspecting the summertime regional averages of precipitation as well as complementary moisture variables of evaporation and $P - E$. Fig. 6.2 shows the seasonal mean precipitation versus the ratio of season to annual precipitation generated by CMIP3 and CMIP5 model simulations for an area-averaged region of the Southwest U.S. (box shown in Fig. 6.1a). CMIP3 models are shown as red markers and CMIP5 models are shown as blue markers, with the largest markers indicating the ensemble

74

mean. A list of values for selected quantities and the corresponding models is shown in Table 6.1. The open ellipses represent one standard deviation from the ensemble means. Inspection of seasonal ratios (ordinate) reveals that both CMIP3 and CMIP5 ensembles simulate too much winter precipitation (a) and too little summer precipitation (c) when compared with both observational datasets (black stars). Both archives perform similarly for all seasons in this region, indicating that the CMIP5 ensemble does not demonstrate improvement in simulating the winter storm system and summer monsoon precipitation for the southwestern US region. Comparisons of ensemble average regional bias for annual means depict similar results between the archives for 1980-1999, showing a general pattern of CMIP models simulating the western US as too wet and the Midwest as too dry, primarily due to the difficulties in simulating precipitation (Fig 6.13a, c). An inspection of seasonal mean values of evaporation for the same region and time set, however, reveal that CMIP5 does demonstrate some improvement over the CMIP3 ensemble. The Student's T-test and Kolmogorov-Smirnov test were performed between the CMIP3 and CMIP5 archives for all calculated quantities to determine whether the ensembles are statistically indistinguishable; Table 6.5 contains the results of these tests. For evaporation and $P - E$ quantities for season-averaged summer, both tests failed, indicating that the two multimodel ensembles are statistically distinct at a 95% significance level. The outcome indicates that the CMIP5 ensemble produces statistically significant simulation results when compared with its CMIP3 predecessor for the southwestern US region evaporation and $P - E$ quantities. The CMIP5 ensemble also converges closer to the observational dataset values for this season, indicating an improvement in the archive.

75

The improvement in skill between CMIP3 and CMIP5 in simulating present-day climate could also indicate improved skill for CMIP5 simulated trends (for justification, see the relevant discussion in section 4.2.2). Hsu et al. (2013) recently showed that North American monsoon precipitation is projected to increase by a majority of CMIP3 and CMIP5 models, though the monsoon will be affected by delayed onset. The trends in seasonal precipitation shown in Fig. 6.3 support these findings based on calculations of trend using the CMIP5 ensemble simulations of RCP 4.5 scenario 20-year mean (2080-2099) minus 1980-1999 climatology. The CMIP5 ensemble mean does indicate a slight increase in precipitation during the fall season (Fig. 6.3) which is affected by the later activity of the North American monsoon; this result also supports the prediction that the monsoon will experience delayed onset and completion, with the maximum trend increase occurring in the fall. Previous work analyzing the trend in P and $P - E$ indicated that the CMIP3 ensemble predicts a decrease in surface water availability in the southwestern US due to reduced precipitation and increased evaporation in the winter and spring seasons (Seager et al. 2007); updated recent studies demonstrate a similar result using CMIP5 RCP 8.5 scenario simulations (Seager et al. 2012). While the scatter plots for trend values of P (Fig. 6.3) do indicate reduced future precipitation in the winter and spring months for CMIP3; however, the CMIP5 ensemble mean indicates a much weaker drying trend in spring and even a slight moistening trend in winter for the area-averaged southwestern US region using RCP 4.5 scenario data. Considering the precipitation values alone would lead to the conclusion that the southwestern US will not experience a significant drying trend in the future. It is necessary to inspect the overall trends for $P - E$ (Fig. 6.6) for a more complete picture of the projected climate. In Fig. 6.6, both

76

ensembles do show an annual drying trend for the southwestern US. While the monsoon precipitation is not projected to increase significantly, reduced surface evaporation will contribute to an increase in surface water availability for the summer season. However, increased future evaporation combined with slightly decreased precipitation predicted by CMIP5 will create overall drier conditions for the region during the winter and spring seasons, and a drier annual average. A geographical inspection of the trends in P and $P - E$ reveal that the drying trend is predicted not just over the southwestern US, but for most of the contiguous US and Mexico as well (Fig 6.12a, c, e, g).
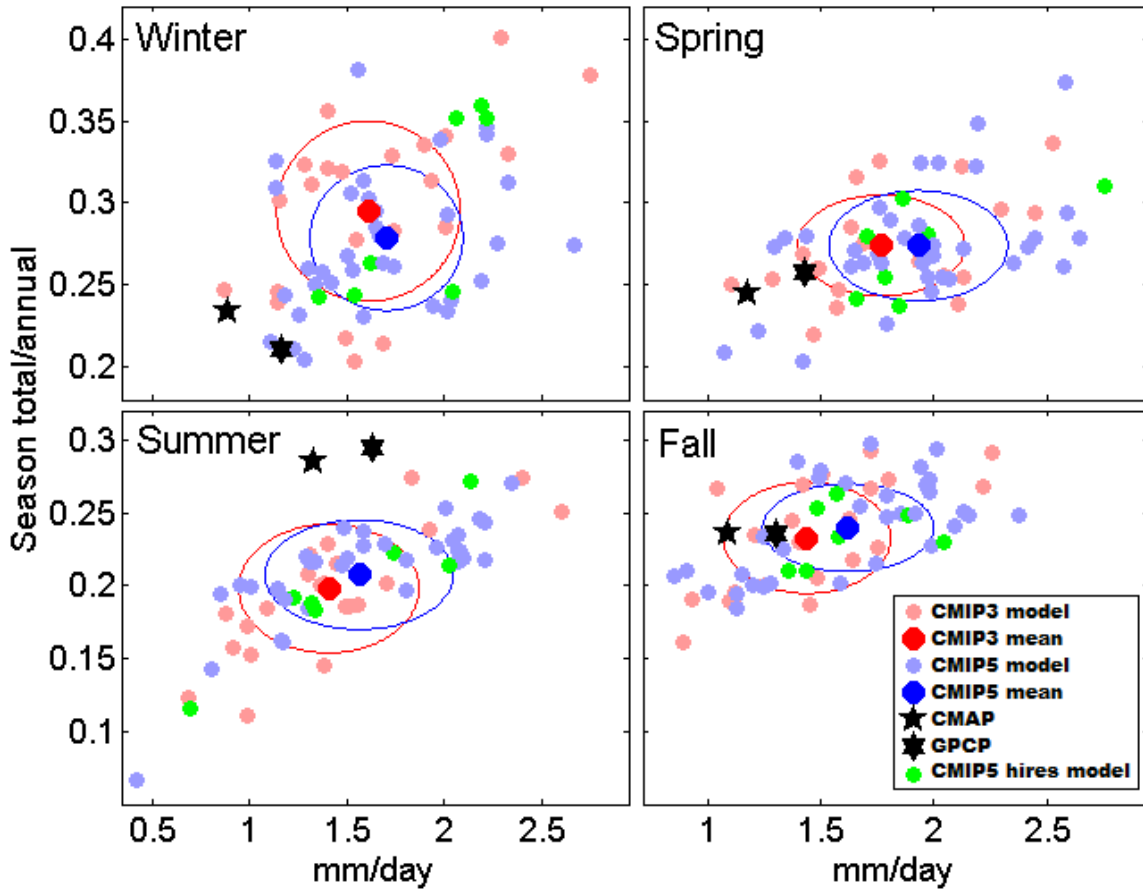
Fig. 6.2 The scatter plots of seasonal mean precipitation (abscissa) vs. the ratio of seasonal to annual mean precipitation (ordinate) for the southwestern US and for four seasons as indicated in the individual panels. Light blue is the CMIP5 ensemble with bold dark blue its ensemble mean. A subset of the high-resolution (horizontal resolution 1.25 degrees or finer) models from CMIP5 are marked in green. Pink and bold red are the CMIP3 ensemble and its ensemble mean. The ovals indicate one standard deviation of the ensemble in the abscissa and ordinate. The two filled stars are the observation from CMAP and GPCP. All simulations and observations are based on the average from 1980-1999. The four seasons are defined as: Spring: MAM, Summer: JJA, Fall: SON, and Winter: DJF.
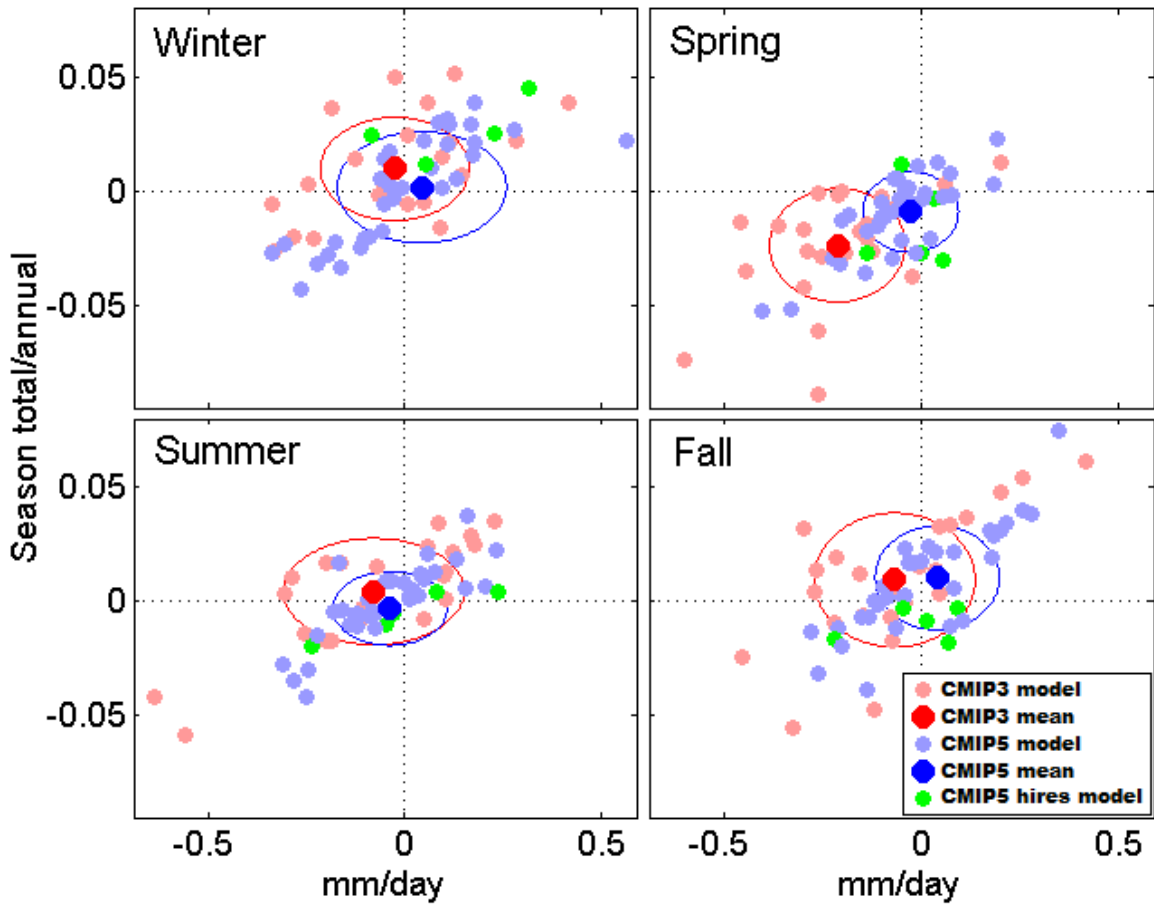
Fig. 6.3 The scatter plots for precipitation in four seasons in the same format as Fig. 6.2 but for the 21st century trend, defined as the mean of 2080-2099 minus that of 1980-1999. The 20C3M and SRES A1B runs from CMIP3, and Historical and RCP4.5 runs from CMIP5, are used to construct the late-20th and late-21st century climatology.
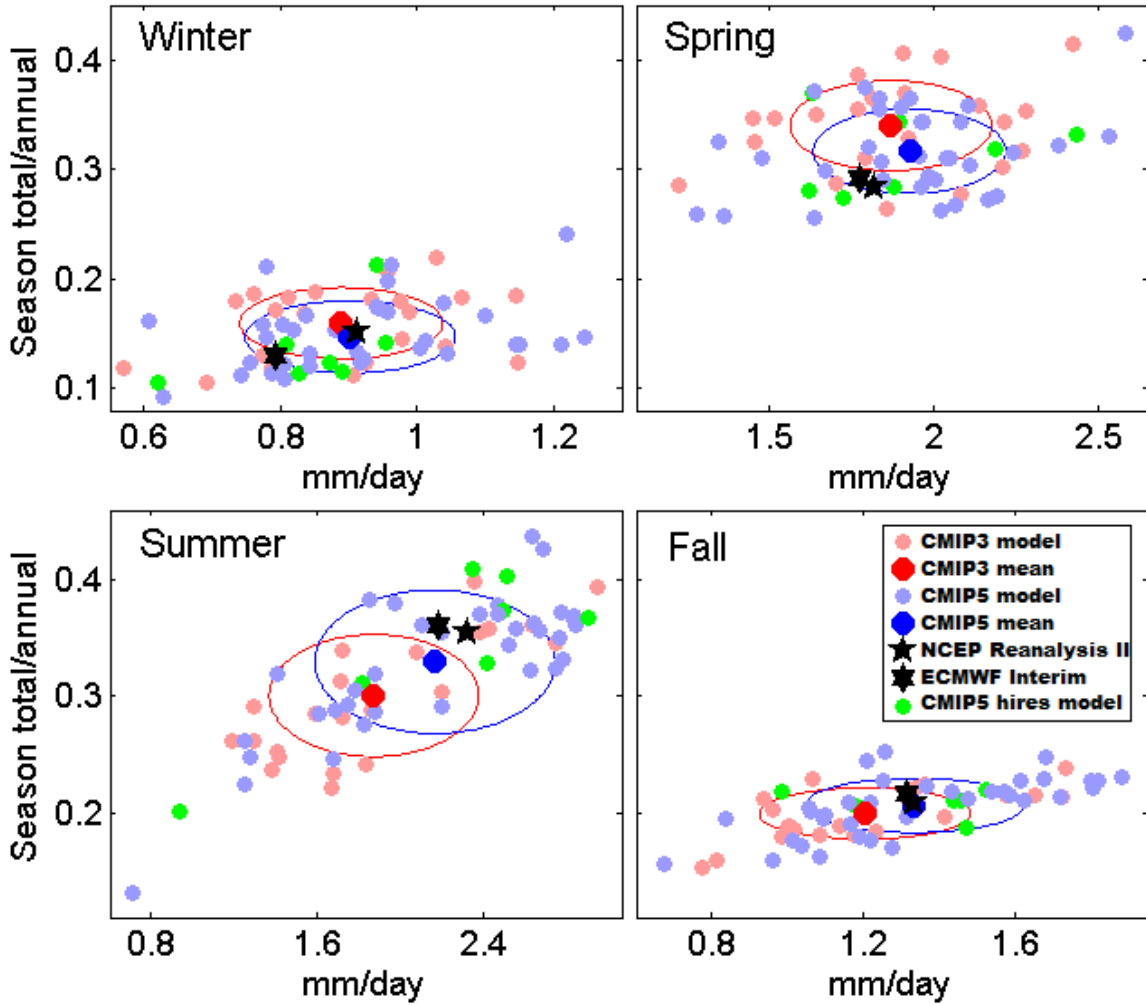
Fig. 6.4 Similar to Fig. 6.2 but for the 1980-1999 climatology of evaporation for the Southwest US. The two filled stars are the seasonal climatology deduced from NCEP Reanalysis II and ERA-Interim reanalysis.
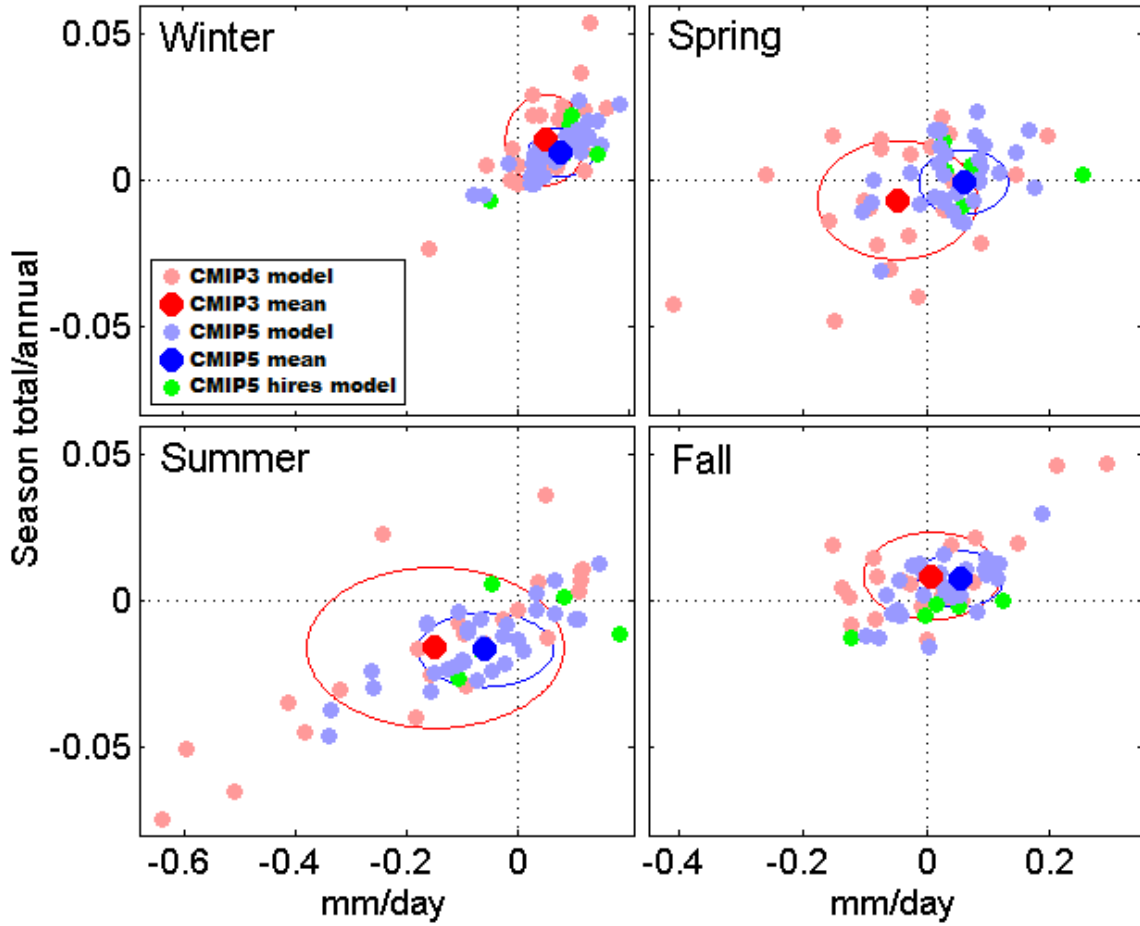
Fig. 6.5 Similar to Fig. 6.3 but for the trend in evaporation for the Southwest US from CMIP3 and CMIP5.
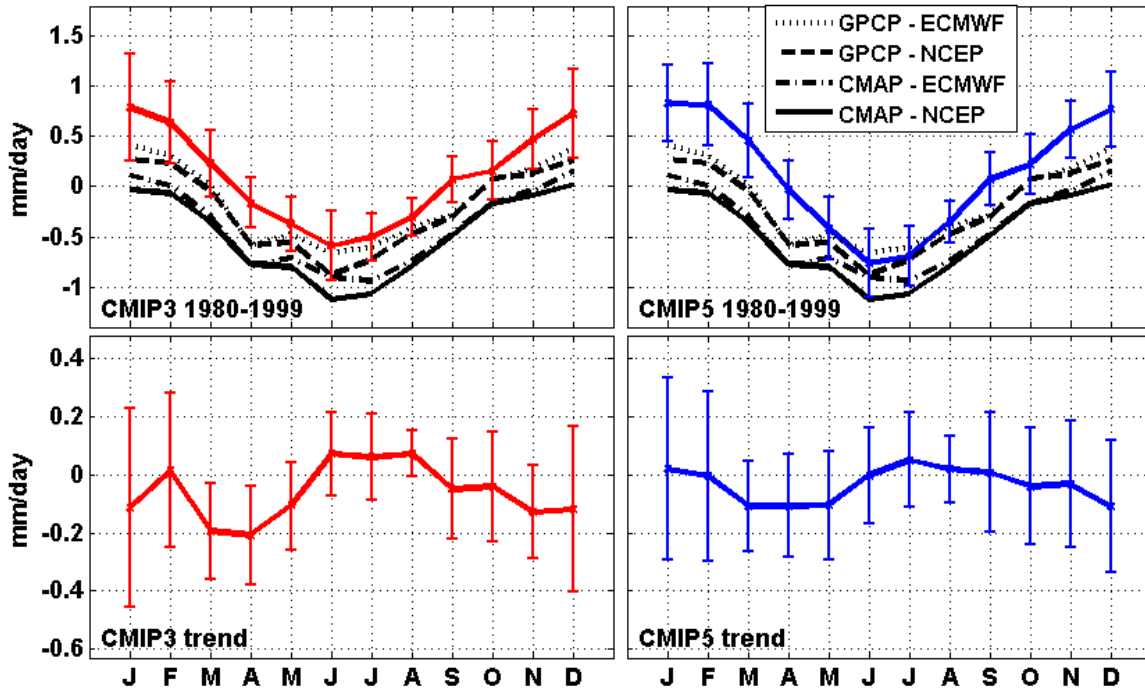
Fig. 6.6 Left column: Top panel is the monthly climatology of *P-E* for 1980-1999 for the Southwest US from the CMIP3 ensemble (red line, with vertical bar indicating plus/minus one standard deviation), compared to the *P-E* from four combinations (black lines) with *P* taken from GPCP or CMAP and *E* taken from ERA-Interim or NCEP Reanalysis II. Bottom panel is the monthly mean trend in *P-E* for the CMIP3 ensemble, with the vertical bar indicating plus/minus one standard deviation. The right column is similar to the left column but for CMIP5.

6.3.2 Mediterranean

The Mediterranean region experiences a strong seasonal influence of winter precipitation from the Northern hemisphere midlatitude storm band. Previous evaluations of the hydrological cycle in this region indicate an atmospheric water deficit evident in observational datasets (Mariotti et al. 2002). This deficit is shown to be strongly correlated with the North Atlantic Oscillation (NAO). It has also been shown that both the CMIP3 and CMIP5 ensembles project a drying trend for the Mediterranean region (Kelley et al. 2012). These findings are confirmed in the regional map of CMIP3 and CMIP5 annual trends in precipitation (Fig. 6.12b, d) and *P – E* (Fig. 6.12f, h) in which

CMIP3 predicts a uniform decrease in precipitation over the entire region and CMIP5 also predicts a nearly uniform decrease, and both ensembles predict severe uniform $P - E$ drying trends. The different processes which govern water availability in this region make it another highly relevant choice for investigation; Fig. 6.13b and d indicate that both CMIP3 and CMIP5 archives produce systematic bias in simulating precipitation for the whole region. Figs. 6.7-6.11 contain the results of the seasonal region-averaged precipitation, evaporation, and $P - E$ using the CMIP3 and CMIP5 ensembles. The wintertime intensity (calculated as the ratio of winter to annual) of precipitation is very high for this region, indicating the high importance of winter storm systems for water resource management. The projected decrease in winter precipitation (Fig. 6.8) and increase in evaporation (Fig. 6.10) and the resulting strong drying trend (Fig. 6.11) predicted by both model ensembles may be cause for concern for local stakeholders. However, notable differences can be seen between the CMIP3 and CMIP5 simulated trends. The ensemble drying trends in precipitation predicted by the CMIP5 RCP4.5 scenario is less severe for all seasons than those predicted by the CMIP3 SRES A1B scenario, but the drying trends in evaporation are more intense for the CMIP5 simulations during winter, spring and summer. The resulting trend in $P - E$ (Fig. 6.11) is thus still present in the CMIP5 simulations, although somewhat less intense than that predicted by their CMIP3 predecessors (Fig. 6.12f, h). These differences are due to variances between the two scenario forcings which are imposed on each model ensemble as well as new modifications which are present in the updated CMIP5 models; however, it is unclear how much each source contributes to the simulated output differences between ensembles.
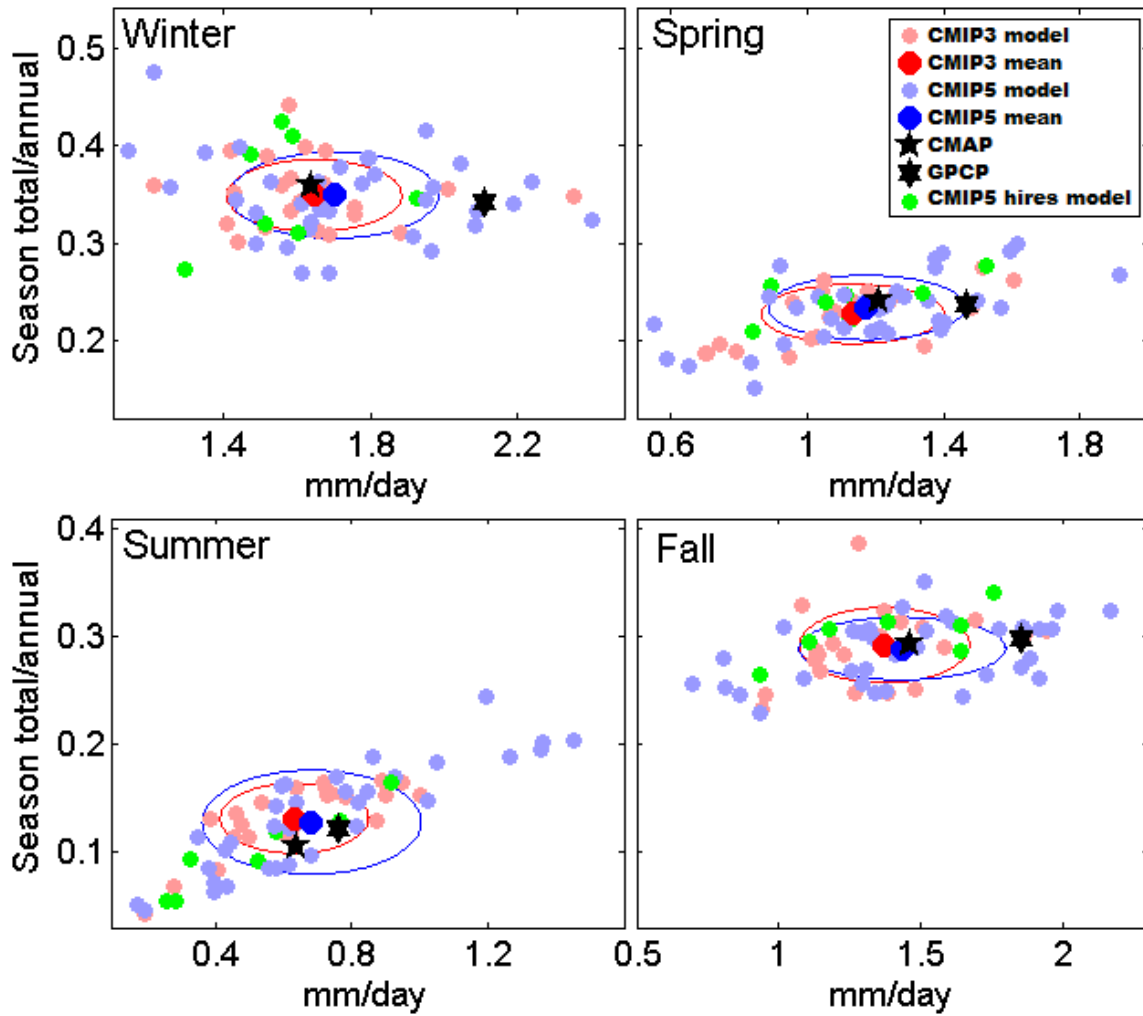
Fig. 6.7 Same as Fig. 6.2 but for the 1980-1999 climatology of precipitation over the Mediterranean region.
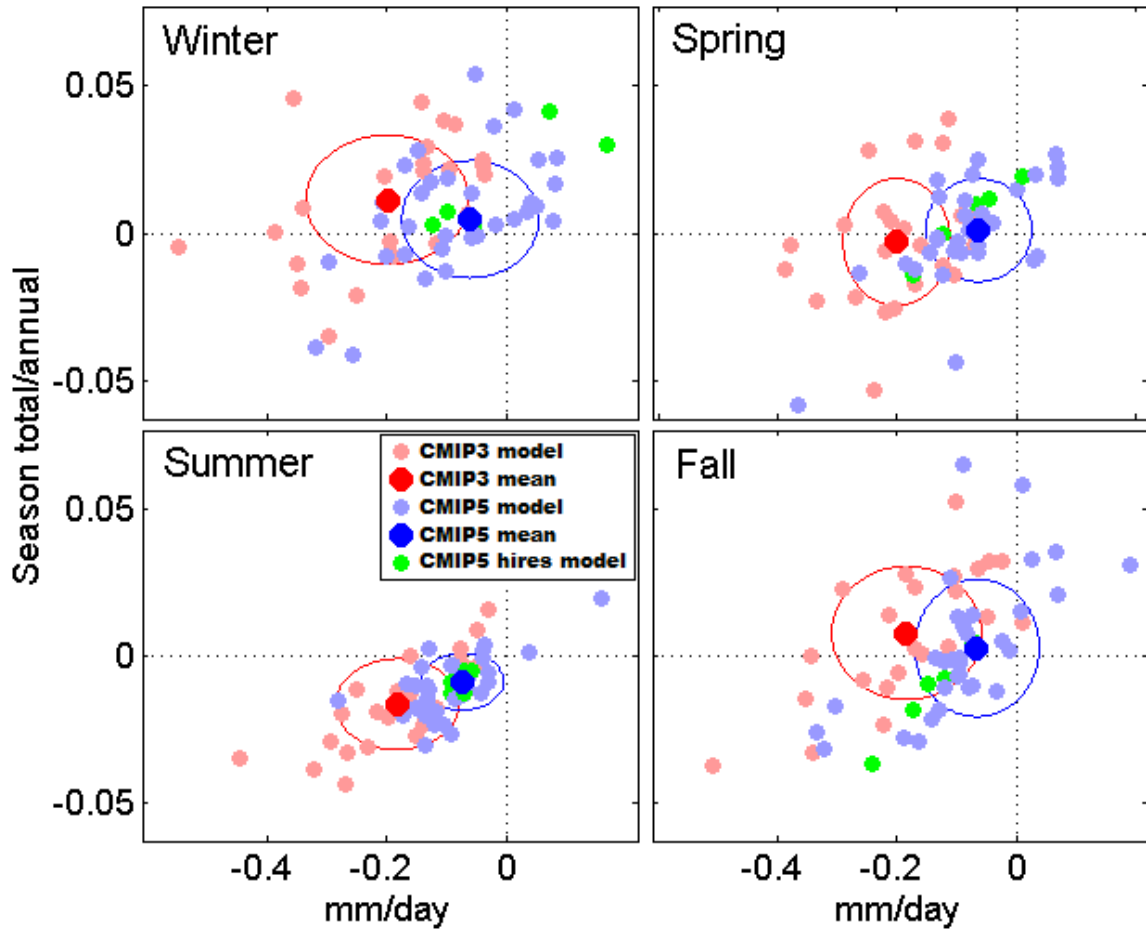
Fig. 6.8 Same as Fig. 6.3 but for the trend in precipitation over the Mediterranean region.
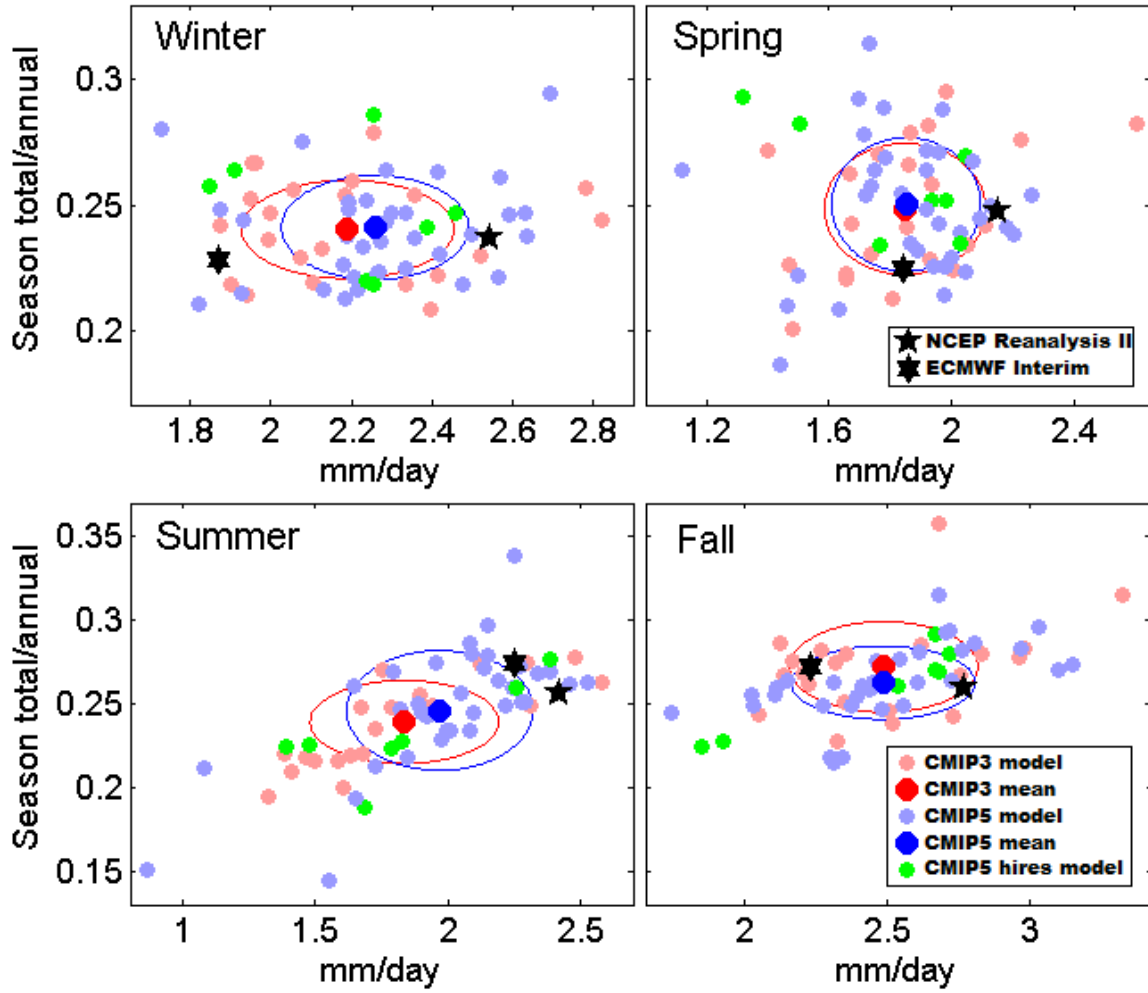
Fig. 6.9 Same as Fig. 6.4 but for the 1980-1999 climatology of evaporation over the Mediterranean region.
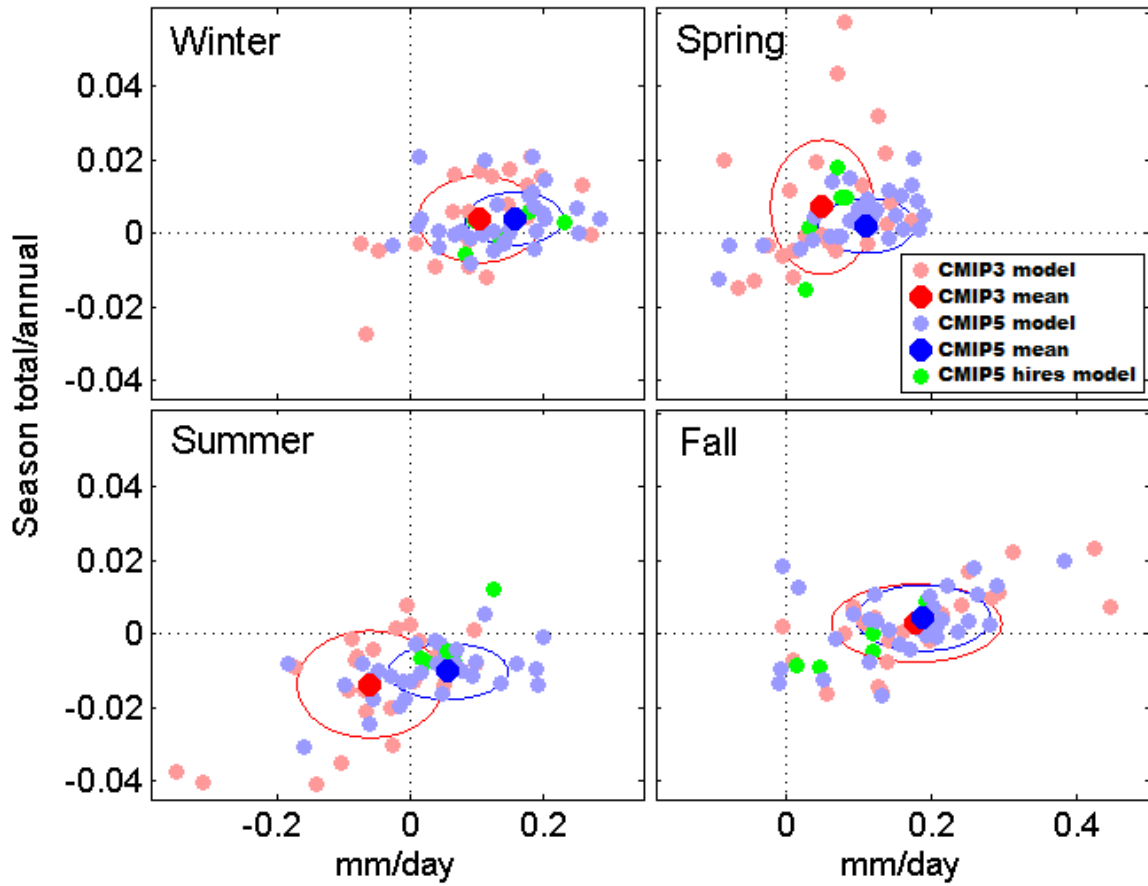
Fig. 6.10 Same as Fig. 6.5 but for the trend in evaporation over the Mediterranean region.
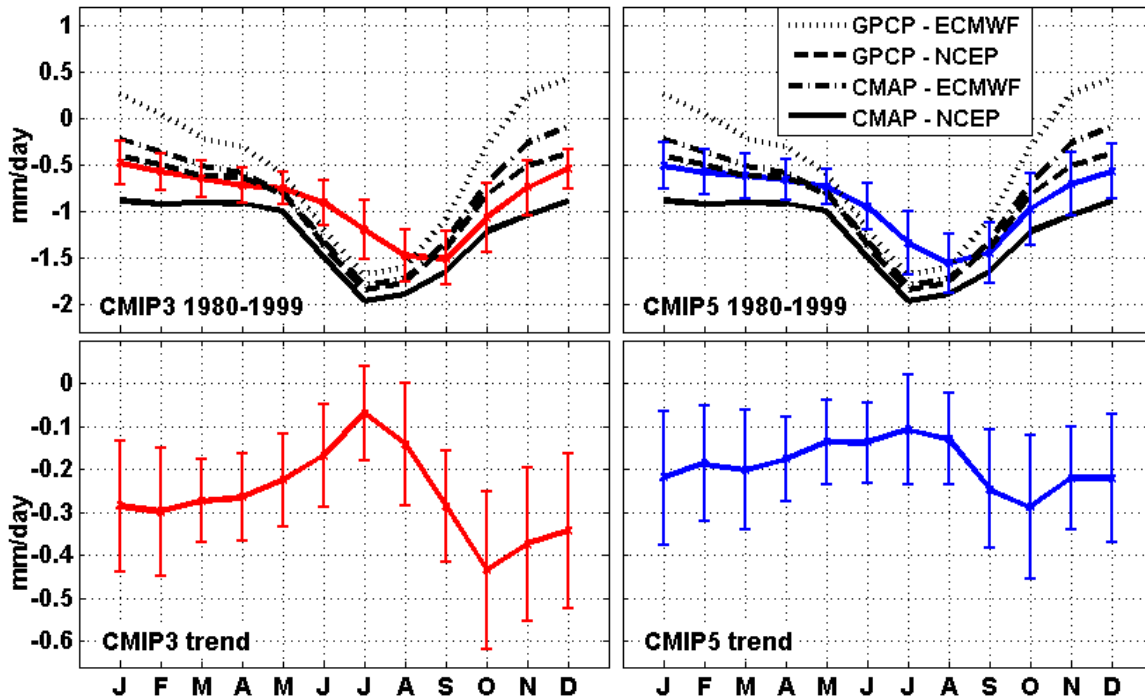
Fig. 6.11 Same as Fig. 6.6 but for the monthly climatology and trend in *P-E* for CMIP3 (left column) and CMIP5 (right column), for the Mediterranean region. The format of presentation is the same as Fig. 6.6, with four different combinations of *P* and *E* used to construct the observed 1980-1999 climatology of *P-E* in the upper panels.

6.4   Conclusions

This chapter provides a detailed analysis of multiple terms associated with the water cycle for two semi-arid regions; the results are highly beneficial both to model development and to water managers who will use the CMIP archives for formulating projections of future climate. The analysis of complementary moisture variables provides a deeper understanding of model strengths and weaknesses when performing studies of present and future climate. The CMIP5 archive is found to perform similarly to CMIP3 in most tested quantities, exhibiting no statistically significant improvement in spread. Both ensembles predict drying trends for both the southwestern US and Mediterranean regions due to seasonal decreases in precipitation and increases in surface evaporation, indicating

reduced surface water availability over the next 100 years. However, in certain regional and seasonal quantities, the two ensembles demonstrate notable bias when compared with observational datasets. The diverse behavior of the models provides an interesting comparison for the selected quantities. Significant bias may be contributed by poor convective parameterizations by ensemble members in regions with large amounts of sub-grid scale precipitation (such as North American monsoonal rainfall). Since these processes occur at scales even below the refinement of the highest resolution models in the archives, no significant improvements can be determined in the performance between the previous CMIP3 and current CMIP5 ensembles for the quantities tested in this study.
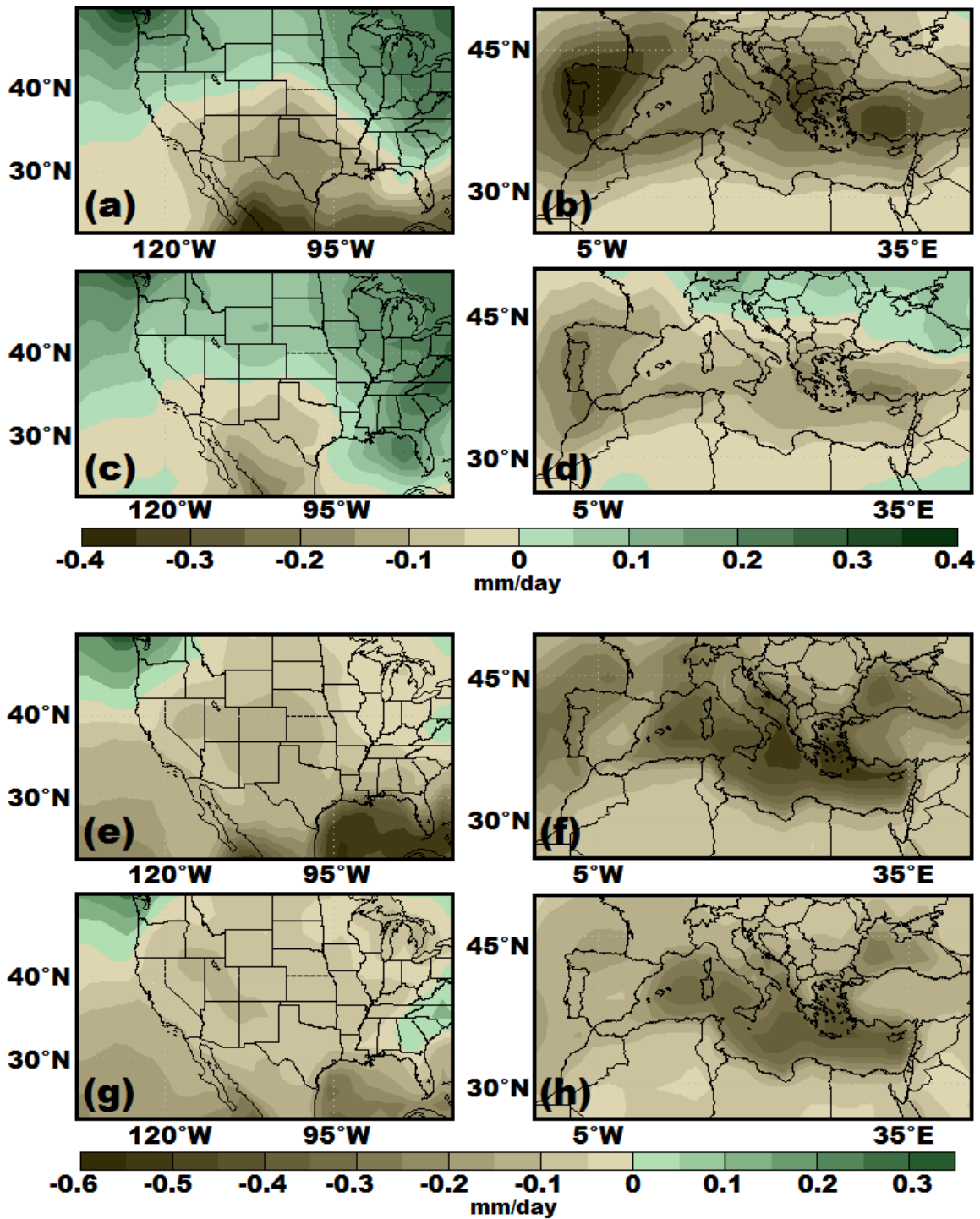
Fig. 6.12 (a) The trend in the annual mean *P* over Southwest US from CMIP3. (b) The trend in the annual mean *P* over the Mediterranean region from CMIP3. (c) The trend in the annual mean *P* over Southwest US from CMIP5. (d) The trend in the annual mean *P* over the Mediterranean region from CMIP5. Panels (e), (f), (g), and (h) are the *P-E* counterparts of (a), (b), (c), and (d). The trend is defined as the average of 2080-2099 minus that of 1980-1999.

90
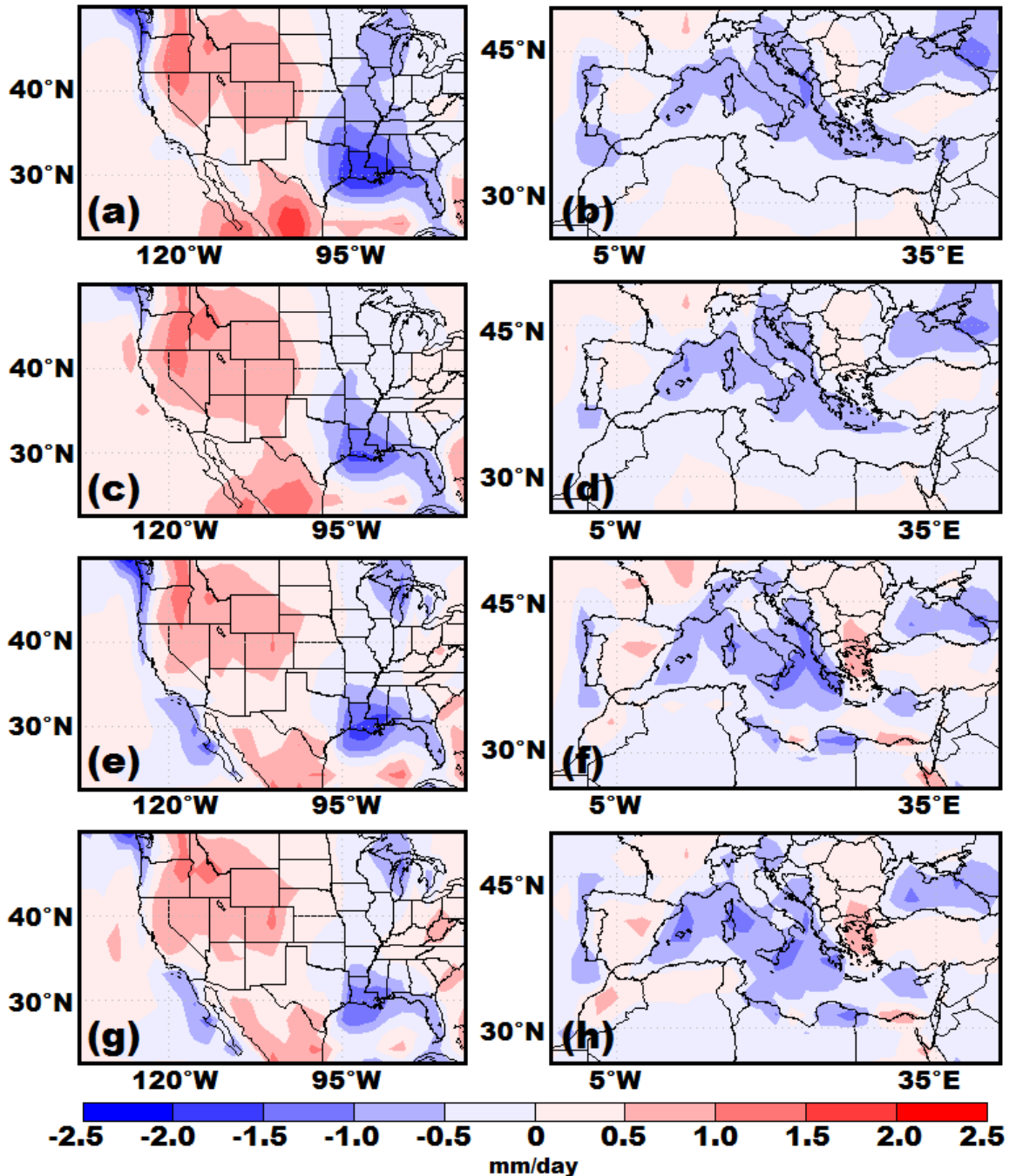
Fig. 6.13 (a) The bias in the annual mean *P* over Southwest US for CMIP3. (b) The bias in the annual mean *P* over the Mediterranean region for CMIP3. (c) The bias in the annual mean *P* over Southwest US for CMIP5. (d) The bias in the annual mean *P* over the Mediterranean region for CMIP5. Panels (e), (f), (g), and (h) are the bias in *P-E* counterparts of (a), (b), (c), and (d). The bias is defined as the multi-model ensemble mean of CMIP3 or CMIP5 minus observation for 1980-1999. The GPCP data is used for the observed precipitation and ECMWF-Interim data used for evaporation.

| No. | Model (CMIP3) | CMIP3 20C3M climatology (1980-99) | | | |
| | | Southwestern US (Summer) | | Mediterranean (Winter) | |
		Precipitation	Evaporation	Precipitation	Evaporation
1	BCCR-BCM2.0	0.92	1.72	2.35	2.82
2	CCSM3	1.09	1.41	1.51	2.07
3	CGCM3.1(T47)	0.98	1.41	1.69	2.40
4	CGCM3.1(T63)	1.51	2.39	1.58	2.13
5	CNRM-CM3	1.36	1.86	1.43	1.95
6	CSIRO-Mk3.0	0.88	1.29	1.62	2.36
7	CSIRO-Mk3.5	1.39	1.67	1.76	1.99
8	ECHAM5/MPI-OM	1.49	1.67	1.56	2.20
9	FGOALS-g1.0	1.56	2.20	2.01	2.52
10	GFDL-CM2.0	1.83	2.43	1.21	1.87
11	GFDL-CM2.1	1.93	2.64	1.67	2.06
12	GISS-AOM	1.00	1.19	1.58	2.19
13	GISS-EH	0.99	1.38	1.61	1.90
14	GISS-ER	0.69	1.29	1.42	1.95
15	INM-CM3.0	2.40	2.95	1.88	2.41
16	INGV-SXG	1.30	2.08	1.44	2.33
17	IPSL-CM4	1.71	1.84	1.76	2.78
18	MIROC3.2(hires)	1.44	2.36	1.58	1.96
19	MIROC3.2(medres)	1.40	1.71	1.68	2.00
20	MRI-CGCM2.3.2	1.38	1.59	1.52	2.25
21	PCM	2.61	2.75	1.41	2.11
22	UKMO-HadCM3	1.31	1.72	1.66	1.94
23	UKMO-HadGEM1	1.20	1.55	1.94	2.18
	Ensemble mean	1.41	1.87	1.65	2.19
	Std. deviation	0.46	0.51	0.24	0.26
	Model (obs.)				
	CMAP	1.33	-	1.64	-
	GPCP	1.63	-	2.11	-
	NCEP	-	2.32	-	2.54
	ECMWF	-	2.19	-	1.87

Table 6.1: CMIP3 (20C3M simulation runs) and observational dataset quantities calculated as long-term past (1980-1999) seasonal averages: (July-September) for southwestern US (30N – 40N, 120W – 95W), (December-February) for Mediterranean region (30N – 45N, 5W – 35E) for mean climatological values in units of mm/day. Calculated ensemble mean and standard deviation for each quantity are also shown.

		CMIP5 Historical climatology (1980-99)			
		Southwestern US (Summer)		Mediterranean (Winter)	
No.	Model (CMIP5)	Precipitation	Evaporation	Precipitation	Evaporation
1	BCC-CSM1.1	1.30	1.82	2.09	2.30
2	BCC-CSM1.1.m	1.34	1.88	2.09	2.35
3	BNU-ESM	1.17	1.27	1.66	2.29
4	CanCM4	0.70	0.94	1.47	2.25
5	CanESM2	1.80	2.20	1.79	2.57
6	CCSM4	0.85	1.25	1.53	2.23
7	CMCC-CESM	0.95	1.41	1.44	2.22
8	CMCC-CM	1.74	2.42	1.52	2.39
9	CMCC-CMS	1.80	2.47	1.21	1.73
10	CNRM-CM5	1.31	2.35	1.59	1.91
11	ACCESS1.0	1.34	2.52	1.56	1.85
12	ACCESS1.3	1.50	2.10	1.57	2.13
13	CSIRO-Mk3.6.0	0.80	1.25	2.05	2.41
14	EC-EARTH	1.23	1.82	1.93	2.46
15	FGOALS-g2	1.81	1.88	2.41	2.50
16	FGOALS-s2	0.42	0.71	1.44	2.69
17	FIO-ESM	2.08	2.64	1.49	2.42
18	GFDL-CM3	2.21	2.76	1.64	2.19
19	GFDL-ESM2G	2.35	2.67	1.61	2.18
20	GFDL-ESM2M	2.07	2.53	1.69	2.27
21	GISS-E2-H	2.04	2.85	1.97	2.63
22	GISS-E2-H-CC	1.96	2.77	1.92	2.59
23	GISS-E2-R	2.19	2.84	1.69	2.27
24	GISS-E2-R-CC	2.21	2.84	1.62	2.21
25	HadCM3	1.31	1.75	1.63	1.93
26	HadGEM2-AO	1.29	1.78	1.97	2.19
27	HadGEM2-CC	1.18	1.69	2.24	2.24
28	HadGEM2-ES	1.14	1.61	1.95	2.19
29	INM-CM4	1.16	1.68	1.26	2.08
30	IPSL-CM5A-LR	1.15	1.98	1.35	1.93
31	IPSL-CM5A-MR	1.00	1.86	1.14	1.87
32	IPSL-CM5B-LR	2.07	2.69	1.49	1.82
33	MIROC4h	2.13	2.49	1.60	2.24
34	MIROC5	1.47	2.38	2.19	2.64
35	MIROC-ESM	2.01	2.78	1.68	2.48
36	MIROC-ESM-CHEM	1.70	2.56	1.67	2.56
37	MPI-ESM-LR	1.59	2.47	1.80	2.26
38	MPI-ESM-MR	1.48	2.21	1.72	2.19
39	MPI-ESM-P	1.59	2.64	1.95	2.33
40	MRI-CGCM3	2.03	2.90	1.30	2.26
41	NorESM1-M	2.10	2.79	1.81	2.34
42	NorESM1-ME	2.08	2.63	1.78	2.29
	Ensemble mean	1.56	2.17	1.70	2.26
	Std. deviation	0.46	0.51	0.28	0.23

Table 6.2: CMIP5 quantities calculated as long-term past (1980-1999) seasonal averages: (July-September) for southwestern US (30N – 40N, 120W – 95W), (December-February) for Mediterranean region (historical CMIP5 simulation runs) for mean climatological values (abscissa, mm/day) and seasonal ratios (ordinate). Calculated ensemble mean and standard deviation for each quantity are also shown.

		CMIP3 SRES A1B trend (2080-99 minus 1980-99)			
		Southwestern US (Summer)		Mediterranean (Winter)	
No.	Model (CMIP3)	Precipitation	Evaporation	Precipitation	Evaporation
1	BCCR-BCM2.0	0.23	0.11	-0.39	-0.05
2	CCSM3	0.12	0.12	-0.14	0.10
3	CGCM3.1(T47)	-0.11	-0.16	-0.09	0.12
4	CGCM3.1(T63)	-0.29	-0.24	-0.34	0.04
5	CNRM-CM3	-0.11	-0.18	-0.06	0.09
6	CSIRO-Mk3.0	0.10	0.11	-0.04	0.18
7	CSIRO-Mk3.5	-0.64	-0.64	-0.14	0.09
8	ECHAM5/MPI-OM	-0.56	-0.51	-0.36	-0.07
9	FGOALS-g1.0	-0.25	-0.38	-0.14	0.26
10	GFDL-CM2.0	0.06	-0.10	-0.10	0.15
11	GFDL-CM2.1	-0.16	-0.32	-0.20	0.18
12	GISS-AOM	-0.07	-0.03	-0.12	0.15
13	GISS-EH	-0.20	-0.18	-0.19	0.20
14	GISS-ER	0.09	0.05	-0.19	0.11
15	INM-CM3.0	-0.20	-0.41	-0.34	0.08
16	INGV-SXG	-0.30	-0.60	-0.30	0.09
17	IPSL-CM4	0.10	0.05	-0.35	0.27
18	MIROC3.2(hires)	-0.18	-0.11	-0.55	-0.07
19	MIROC3.2(medres)	0.17	0.04	-0.04	0.01
20	MRI-CGCM2.3.2	0.18	0.11	-0.25	0.18
21	PCM	0.07	-0.06	-0.03	0.06
22	UKMO-HadCM3	0.05	-0.09	-0.09	0.18
23	UKMO-HadGEM1	0.10	0.00	-0.13	0.07
	Ensemble mean	-0.08	-0.15	-0.20	0.10
	Std. deviation	0.23	0.23	0.14	0.09

Table 6.3: Same as Table 6.1 but for long-term mean future (2080-2099) minus past (1980-1999) trends using CMIP3 SRES A1B simulation runs.

| No. | Model (CMIP5) | CMIP5 RCP4.5 trend (2080-99 minus 1980-99) | | | |
| | | Southwestern US (Summer) | | Mediterranean (Winter) | |
		Precipitation	Evaporation	Precipitation	Evaporation
1	BCC-CSM1.1	-0.18	-0.26	0.05	0.20
2	BCC-CSM1.1.m	0.15	0.11	-0.20	0.25
3	BNU-ESM	-0.09	-0.10	0.08	0.25
5	CanESM2	-0.05	-0.07	-0.06	0.23
6	CCSM4	0.04	0.07	-0.10	0.09
8	CMCC-CM	0.16	0.15	-0.10	0.15
9	CMCC-CMS	0.08	0.09	0.07	0.18
10	CNRM-CM5	-0.23	-0.05	-0.10	0.14
11	ACCESS1.0	0.00	-0.09	-0.05	0.11
12	ACCESS1.3	-0.07	0.01	0.08	0.14
13	CSIRO-Mk3.6.0	0.01	-0.02	-0.15	0.20
14	EC-EARTH	-0.03	-0.10	-0.12	0.08
15	FGOALS-g2	-0.09	-0.06	-0.06	0.07
16	FGOALS-s2	0.02	0.04	-0.14	0.28
17	FIO-ESM	0.13	0.04	-0.30	0.01
18	GFDL-CM3	-0.12	-0.04	-0.21	0.20
19	GFDL-ESM2G	-0.03	0.07	-0.11	0.11
20	GFDL-ESM2M	0.08	0.00	-0.17	0.12
21	GISS-E2-H	-0.25	-0.13	0.01	0.08
22	GISS-E2-H-CC	-0.12	-0.06	-0.16	0.04
23	GISS-E2-R	-0.31	-0.26	0.01	0.18
24	GISS-E2-R-CC	-0.22	-0.15	0.08	0.18
26	HadGEM2-AO	-0.28	-0.34	0.04	0.18
27	HadGEM2-CC	-0.07	-0.11	-0.05	0.11
28	HadGEM2-ES	0.01	-0.10	0.05	0.19
29	INM-CM4	0.04	-0.02	-0.13	0.01
30	IPSL-CM5A-LR	-0.09	-0.11	-0.17	0.02
31	IPSL-CM5A-MR	-0.14	-0.16	-0.02	0.13
32	IPSL-CM5B-LR	0.21	0.11	-0.06	0.15
34	MIROC5	0.06	-0.15	-0.02	0.14
35	MIROC-ESM	0.05	-0.15	-0.26	0.19
36	MIROC-ESM-CHEM	0.23	-0.02	-0.32	0.09
37	MPI-ESM-LR	-0.16	-0.34	-0.14	0.04
39	MPI-ESM-P	-0.25	-0.07	-0.21	-0.03
40	MRI-CGCM3	0.24	0.19	0.17	0.10
41	NorESM1-M	-0.05	-0.09	0.04	0.19
42	NorESM1-ME	-0.17	-0.16	-0.10	0.13
	Ensemble mean	-0.04	-0.06	-0.06	0.16
	Std. deviation	0.15	0.12	0.12	0.07

Table 6.4: Same as Table 6.2 but for long-term mean future (2080-2099) minus past (1980-1999) trends using CMIP5 RCP4.5 simulation runs.

Region	Season	Quantity	T-test	KS-test	F-test
Southwest US	Winter (December-February)	Precipitation	0	0	0
		Evaporation	0	0	0
		P-E	0	0	0
	Spring (March-May)	Precipitation	0	1	0
		Evaporation	0	0	0
		P-E	0	0	0
	Summer (June-August)	Precipitation	0	0	0
		Evaporation	1	1	0
		P-E	1	1	0
	Fall (September-November)	Precipitation	0	0	0
		Evaporation	0	0	0
		P-E	0	1	0
Mediterranean	Winter (December-February)	Precipitation	0	0	0
		Evaporation	0	1	0
		P-E	0	0	0
	Spring (March-May)	Precipitation	0	0	0
		Evaporation	0	0	0
		P-E	0	0	0
	Summer (June-August)	Precipitation	0	0	0
		Evaporation	0	1	0
		P-E	0	0	0
	Fall (September-November)	Precipitation	0	0	0
		Evaporation	0	0	0
		P-E	0	0	0

Table 6.5: Two-sample Student's T-test, Kolmogorov-Smirnov test, and F-test for equal variance results performed with the CMIP3 and CMIP5 ensembles for selected quantities (1980-1999). A result of 0 supports the null hypothesis that the two ensembles are statistically indistinguishable; a result of 1 rejects the null hypothesis at the 5% significance level.

CHAPTER 7

EXAMINING MODEL QUALITY IN SIMULATING

GLOBAL MOISTURE TRANSPORT

This investigation delves deeper into the quality of the water cycle in the CMIP model archives by further examining the individual terms of the water budget. Four models from the most current CMIP5 model archive are selected for analysis due to the limited availability of daily simulation output data. The horizontal and vertical structure of present (1981-2000) global moisture transport is examined and compared with NCEP Reanalysis I observational data. All quantities are directly computed from the model simulation data for both the time-averaged present and future (2081-2100) states for the selected CMIP5 models. It is shown that the models reasonably reproduce global moisture transport; however, all models exhibit deficiencies which are illuminated when the calculated quantities are compared with those produced using the observational dataset.

7.1   Introduction

Analyses of precipitation in model simulations tend to focus on average precipitation quantities for both regional and global studies (Covey et al. 2003, Rasch et al. 2006, Solomon et al. 2007, Karl et al. 2009). However, precipitation can exhibit intermittent behavior which cannot be quantified by continuous values like temperature and other climate variables. Precipitation also encompasses different phase states and convective properties, each with particular properties. Previous studies have made efforts in quantifying the response of model simulated precipitation to the physical variables

97

associated with its generation. It has been shown that the frequency of precipitation extremes in climate change scenarios depends on changes in the moist-adiabatic temperature lapse rate, in the upward velocity, and in the temperature when precipitation extremes occur (O'Gorman and Schneider 2009). Challenges in parameterizing precipitation within models have been shown to be related to specific aspects of precipitation such as regional patterns, temporal variations, and the proper combination of the frequency and intensity of precipitation (Houghton et al. 2001, Covey et al. 2003, Meehl et al. 2005, Trenberth et al. 2007). Examining multiple characteristics of precipitation can reveal deficiencies in model physics which is necessary in order to understand possible contributing sources of bias in model simulations. For example, it is possible that multiple errors in these processes cancel to produce a correct precipitation field in the simulation. Previous studies have examined the individual quantities in the moisture budget using observational datasets: Mestas-Nuñez et al. (2007) evaluated seasonal convergence of water vapor flux, and Trenberth and Guillemot (1995) have examined the global vertically integrated moisture budget through evaporation minus precipitation calculations. Liepert and Previdi (2012) also evaluate the global budget for precipitation and evaporation in the CMIP3 archive. This study proposes to build on previous work by further examining the full equation for the water budget for selected models from the updated CMIP5 archive. An in-depth analysis of the individual terms of the moisture budget and a comparison of the quantities with those calculated from observational data will provide a better evaluation of model quality in simulating precipitation.

Chosen for analysis are four models from the CMIP5 archive which have daily output data available for the necessary terms. The simulation data from the 'historical' scenario run output is used for the CMIP5 models: GFDL ESM2M (NOAA Geophysical Fluid Dynamics Laboratory, resolution 144x90 L24), HadGEM2 CC (Hadley Centre for Climate Prediction and Research, 192x145 L40), MPI ESM LR (Max Planck Institute for Meteorology, T63), and BNU ESM (Beijing Normal University, T42). All four models are of the newest type of 'Earth system' models (ESM) which represent a general group of the most advanced global coupled climate models in the archive, featuring a range of new components such as more interactive atmospheric chemistry, aerosols, and dynamic vegetation. The NCEP/NCAR Reanalysis I (Kalnay et al. 1996) data (T62 resolution) is used as the observational dataset for comparison with the model simulations. All calculations use simulations archived at daily time steps unless otherwise noted.

7.2 Calculating the mean flux of water vapor transport

The amount of water vapor for a unit area column of air extending from the surface to the top of the atmosphere is defined as the precipitable water W contained within the unit column (Peixoto and Oort 1992),

$$W(\lambda, \phi, t) = \int_0^{p_0} q \frac{dp}{g}, \qquad (7.1)$$

where q is the specific humidity, p is the pressure, and g is the acceleration of gravity. W is a function of longitude λ, latitude ϕ, and time t. Fig. 7.1 depicts the global distribution of annual mean precipitable water $\overline{W}$. The general structure of precipitable water in the atmosphere shows a general decrease from the equatorial region, where the highest

99

values are observed, to the poles, where minimums occur. The magnitude is generally higher over ocean than land, and the magnitude is also somewhat lower over the desert areas corresponding to the large anticyclones of the subtropics. The vertical structure of water vapor is shown in Fig. 7.2 in the form of zonal-mean cross sections of the specific humidity q. Decreasing dramatically with height, the concentration of water vapor is highest near the surface of the Earth.
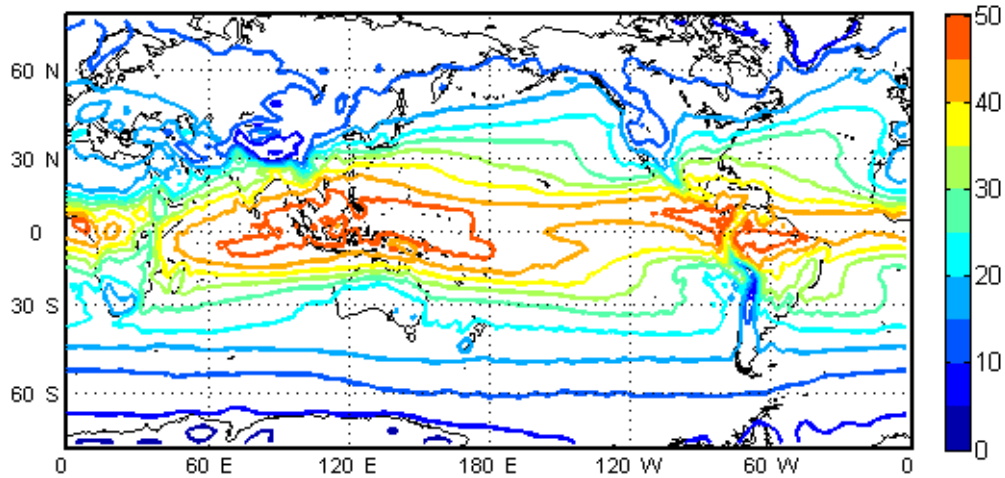
Fig. 7.1 Global distribution of the (1981-2000) atmospheric precipitable water annual mean in units of 10 kg/m^2 using NCEP Reanalysis I observational data.

The integration of the horizontal transport of water vapor with respect to pressure leads to the definition of the water vapor flux $\mathbf{Q}$,

$$\mathbf{Q}(\lambda, \phi, t) = \int_0^{p_s} q\mathbf{V}\frac{dp}{g} = Q_\lambda \mathbf{i} + Q_\phi \mathbf{j}, \qquad (7.2)$$

whose components are given as the zonal Q_λ and meridional Q_ϕ water vapor flux,

$$Q_\lambda = \int_0^{p_s} qu\frac{dp}{g} = \langle qu \rangle \qquad (7.3)$$

$$Q_\phi = \int_0^{p_s} qv\frac{dp}{g} = \langle qv \rangle, \qquad (7.4)$$

where u and v are the zonal and meridional wind velocity components of the atmospheric flow vector $\boldsymbol{V}$. The time averages of the total zonal transport of water vapor $\bar{Q}_\lambda$ and the total meridional transport of water vapor $\bar{Q}_\phi$ are defined as,

$$\bar{Q}_\lambda = \overline{\langle qu \rangle}, \qquad (7.5)$$

$$\bar{Q}_\phi = \overline{\langle qv \rangle}. \qquad (7.6)$$

The quantity $\overline{\langle qu \rangle}$ is defined as the time and vertical average of the product,

$$\overline{\langle qu \rangle} = \overline{\langle q \rangle}\,\overline{\langle u \rangle} + \overline{\langle \bar{q}''\bar{u}'' \rangle} + \overline{\langle q \rangle'\langle u \rangle'} + \overline{\langle (q'')'(u'')' \rangle}, \qquad (7.7)$$

where the first and second terms on the right-hand side represent the time-average barotropic and baroclinic contributions, respectively, and the last two terms represent the transient barotropic and baroclinic perturbations, respectively. The quantity $\overline{\langle qv \rangle}$ may be defined similarly.

The vertical average for the zonal component is calculated as the sum of the ratio of the discrete pressure levels to the surface pressure, or,

$$\langle qu \rangle \equiv \frac{\int_{p_0}^{p_s} qu\, dp}{\int_{p_0}^{p_s} dp} = \frac{1}{p_s - p_0} \int_{p_0}^{p_s} qu\, dp \approx \frac{1}{p_s - p_0} \sum_{k=1}^{K} (qu)_k (\Delta p)_k. \qquad (7.8)$$

The pressure level thickness $(\Delta p)_k$ is a function of the vertical pressure level and varies with the surface pressure for that particular location. It is determined using a central finite difference approximation. The vertical average for the meridional component $\langle qu \rangle$ may be found similarly.

Finally, the time averages of the zonal $\overline{\langle qu \rangle}$ (and respective meridional $\overline{\langle qv \rangle}$) components may be calculated by:

$$\overline{\langle qu \rangle} = \frac{1}{N} \sum_{n=1}^{N} \langle qu \rangle_n. \qquad (7.9)$$

Figs. 7.3 and 7.4 show the global distributions of the vertical mean zonal water vapor transport in the eastward direction $\overline{\langle qu \rangle}$ and meridional water vapor transport in the northward direction $\overline{\langle qv \rangle}$ by all motions. The general pattern of the zonal transport reflects the zonal flow pattern, disrupted in only certain locations, such as over India where the summer monsoon circulation occurs. The meridional transport depicts the largest transport of moisture by Hadley circulation, and its variability is associated with the movement and changes in Hadley cells. A closer look at the semiarid regions of the southwestern US and the Mediterranean in Fig. 7.5 depicts the divergence of moisture associated with the descending dry branch of Hadley cell circulation in the subtropical regions related with semiarid climate conditions.

The vertical integrals of the moisture transport terms represent the actual transport of the mass of water vapor in the atmosphere. For the zonal component Q_λ, we may calculate the vertical integral with,

$$\int_{p_0}^{p_s} qu \frac{dp}{g} \approx \frac{1}{g} \sum_{k=1}^{K} (qu)_k (\Delta p)_k \qquad (7.10)$$

in which the integral is calculated from local surface pressure p_s to a pressure at the top of the atmosphere p_0 over K pressure levels using central difference approximation for each level k. An approximation for the vertical integral of the meridional component Q_ϕ is employed in section 7.3 for selected models and observational data, and an in-depth analysis of the moisture flux divergence can be found in section 7.4.

A comparison of the global horizontal and vertical structure of water vapor transport between the selected CMIP5 models and the NCEP Reanalysis data reveals certain model deficiencies. For example, while all models reproduce the basic vertical structure of zonal-mean atmospheric water vapor with a higher concentration near the surface and equatorial regions (Fig. 7.2), all of the models underrepresent the annual equatorial maximum water vapor when compared with observational data for 1981-2000. Three of the CMIP5 models also suffer from errors in reproducing the concentration of water vapor in the vertical column over the polar regions; these errors are consistently present in the simulation data for all calculated time periods. Since these models are similar in that they utilize relatively new schemes which govern active atmospheric chemistry, it is possible that the generated errors are due to these chemistry components of the models. Comparisons between the CMIP5 models and observational data for the vertically averaged horizontal structure of water vapor transport reveal a general strong agreement between simulations. All models reproduce the low- and high-pressure systems associated with Hadley circulation and angular momentum which drive the global transportation of water vapor from the equator to the polar regions.
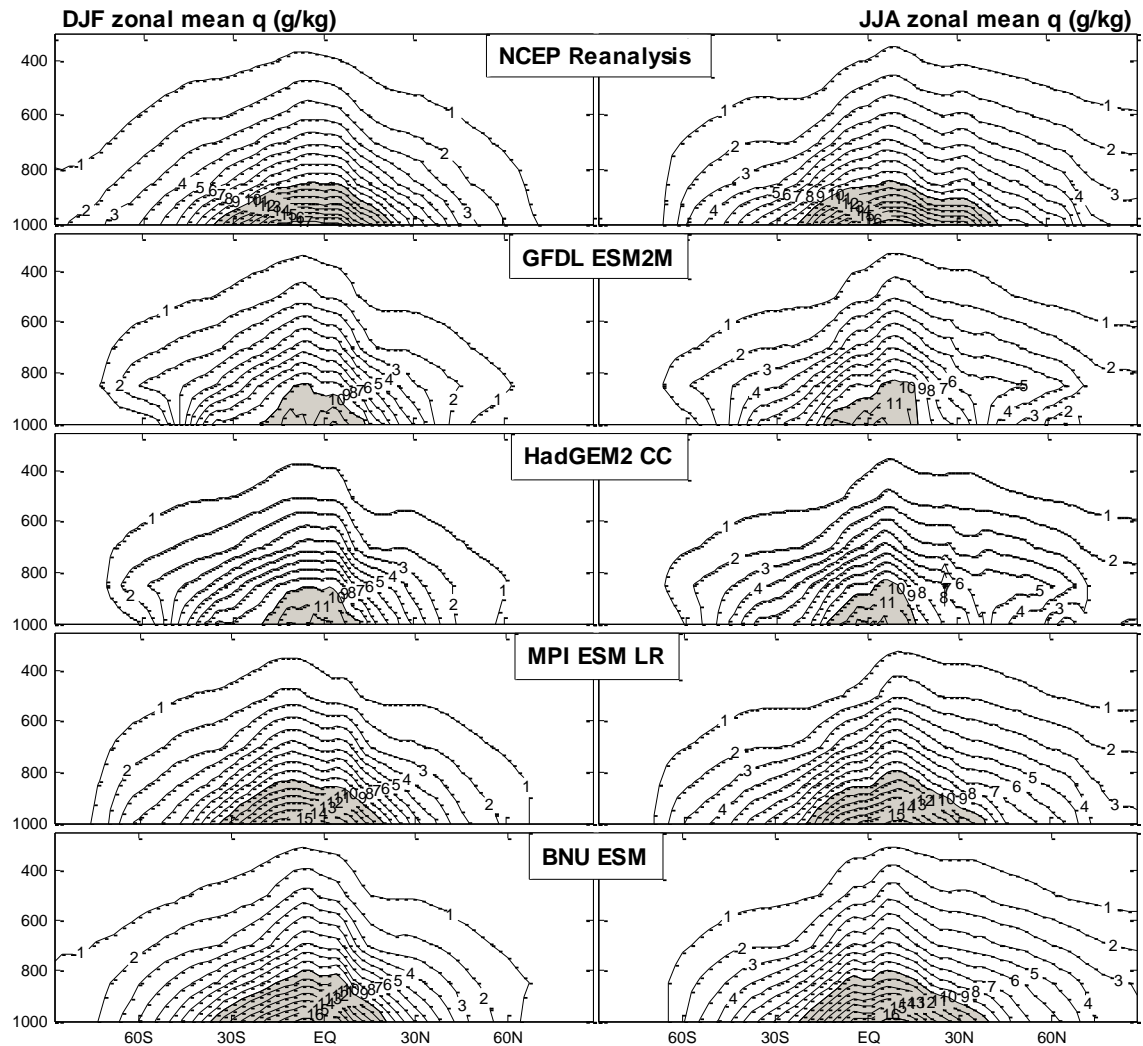
Fig. 7.2 Zonal-mean cross sections of specific humidity for DJF and JJA mean conditions averaged from 1981-2000 comparing four CMIP5 models ('historical' simulation runs) with NCEP Reanalysis I observational data. Shaded regions indicate the highest concentration of water vapor (>10 g/kg). This figure may be verified with Mo and Higgins (1996) for the NCEP data, but with improved accuracy over their analysis, especially over the polar regions due to corrected values where observational data is missing.
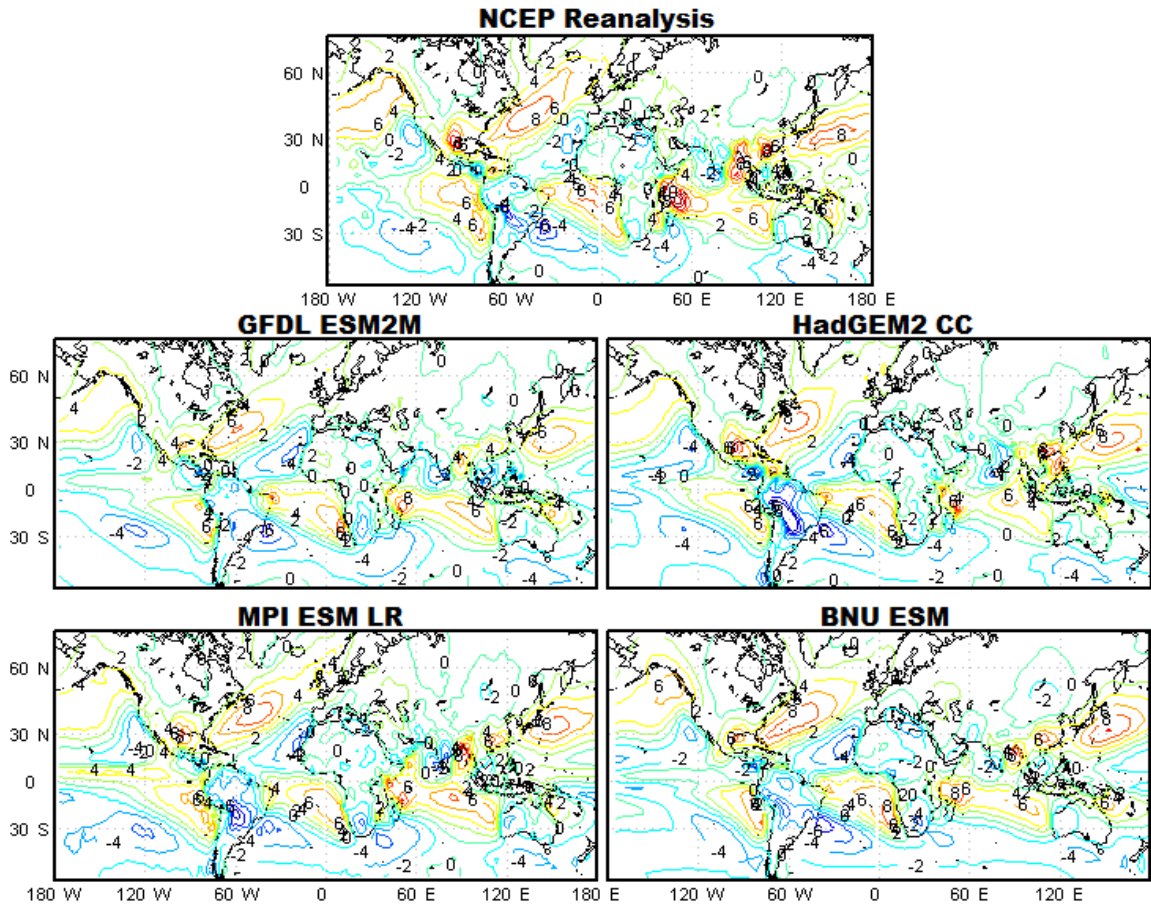
Fig. 7.3 Global distributions of the vertical mean meridional water vapor transport in the northward direction by all motions in m/s g/kg for annual mean (1981-2000) conditions using CMIP5 models ('historical' simulation runs) and NCEP Reanalysis I observational data.
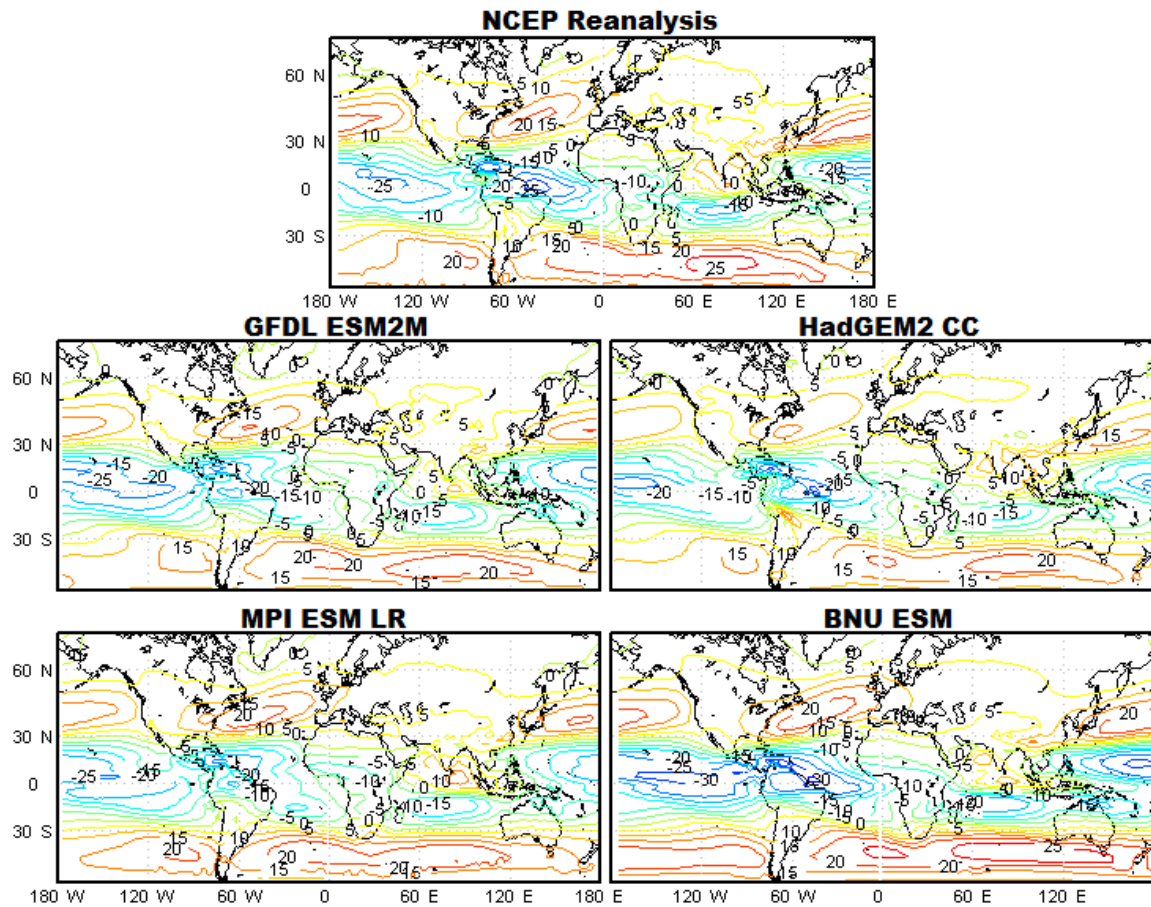
Fig. 7.4 Global distributions of the vertical mean zonal water vapor transport in the eastward direction by all motions in m/s g/kg for annual mean (1981-2000) conditions using CMIP5 models ('historical' simulation runs) and NCEP Reanalysis I observational data.
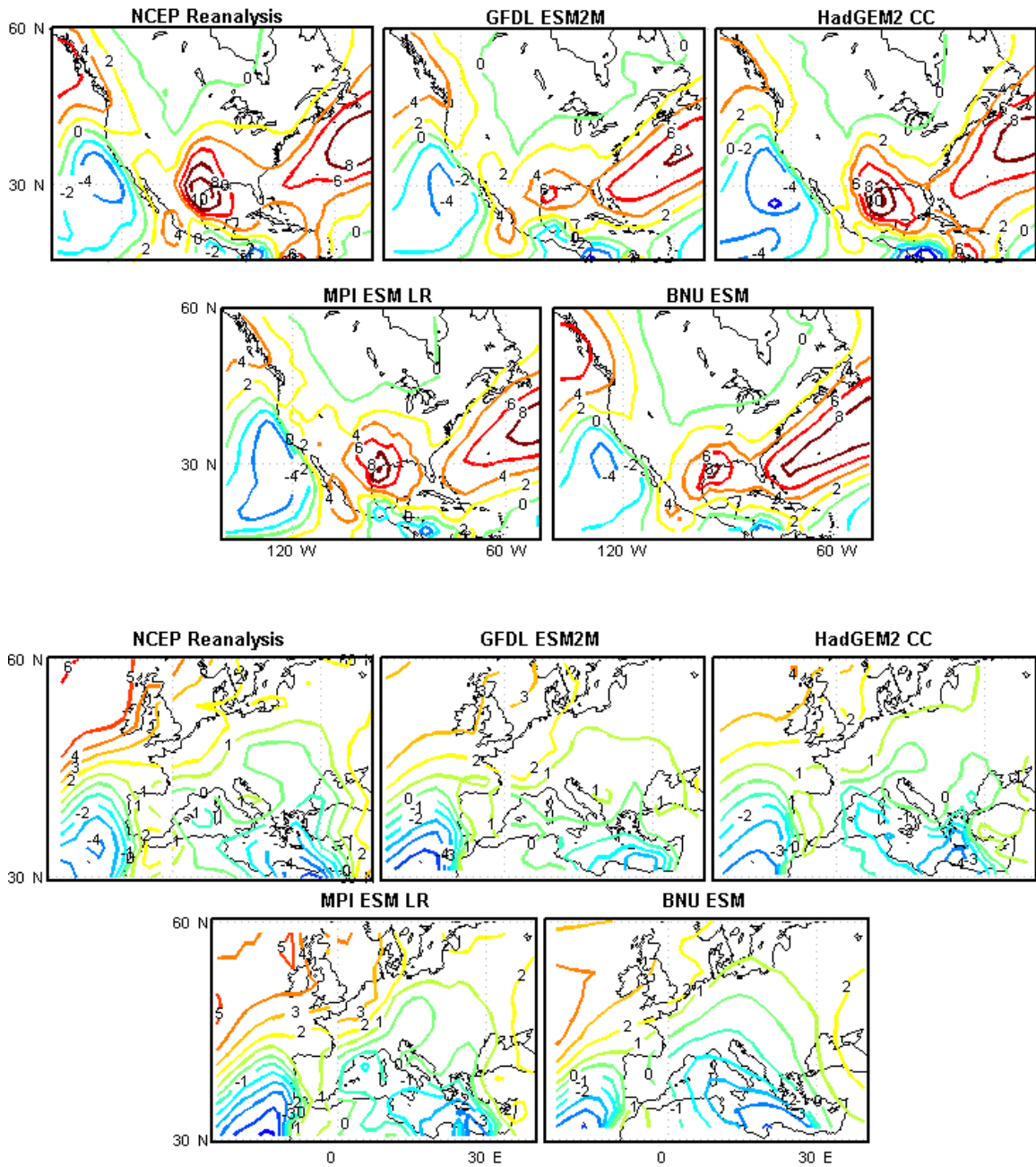
Fig. 7.5 Distributions of the meridional water vapor transport in the northward direction by all motions in m/s g/kg for annual mean (1981-2000) conditions using CMIP5 models ('historical' simulation runs) and NCEP Reanalysis I observational data for the southwestern US (top) and Mediterranean (bottom) regions.

7.3   The moisture transport term

The atmospheric moisture budget analysis continues with an inspection of the meridional moisture transport term (qv). We may explore moisture transport by different time scales in which the total moisture transport is the sum of the long term mean and the climate and synoptic anomalies:

$$x \quad = \quad \bar{x} \quad + \quad x^c \quad + \quad x^s.$$

$$total \; = \quad long\;term\;mean \; + \; climate\;anomaly \; + \; synoptic\;anomaly$$

The mean mass conservation of the atmosphere may be defined as,

$$\bar{Q} = \overline{qv} + \overline{q^c v^c} + \overline{q^s v^s}. \qquad (7.11)$$

The mean moisture budget is a balance between the moisture flux divergence and the water source/sink terms. In the tropics and subtropics, the meridional moisture flux is dominated by transport from the mean flow terms. In the midlatitudes, the meridional flux by synoptic anomalies is equivalent to or greater than the meridional flux by mean flow. This synoptic variability is focused within atmospheric rivers (Zhu and Newell 1998) which provide extratropical water vapor transport from the tropics. The profile of the zonal mean vertically integrated meridional moisture transport term (qv) can thus be used as a measure of Hadley circulation. Adapting (7.10), this quantity is defined as,

$$\int_{p_0}^{p_s} qv \frac{dp}{g} \approx \frac{1}{g} \sum_{k=1}^{K} (qv)_k \, (\Delta p)_k \qquad (7.12)$$

where q and v are the simulated daily values for specific humidity and northward meridional wind velocity, respectively. The vertical integral was calculated from the local surface pressure to a pressure near the top of the atmosphere over K pressure levels using

central difference approximation for each level k. Since only a small fraction of the total

water vapor present in the
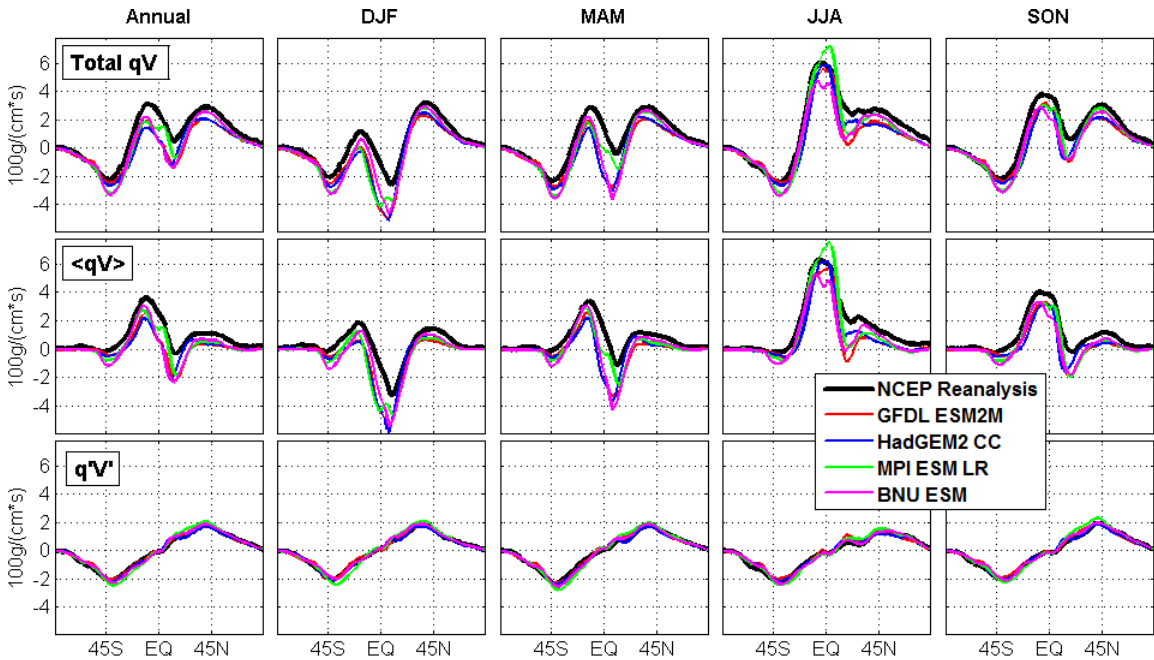
Fig. 7.6 Seasonal decomposition of the vertically integrated meridional profiles of the zonal mean seasonal northward transport of water vapor into the monthly mean component $< qV >$ and the sub-monthly variations due to transient eddies $q'V'$. Derived from 1981-2000 in units of 100 g/(cm*s) using CMIP5 models ('historical' simulation runs) and NCEP Reanalysis I observational data.

atmosphere exists at an altitude higher than the 300 mb pressure level, this level was

chosen as the integral upper limit for calculation.

The calculation for the zonal mean vertically integrated meridional moisture

transport was performed for each grid space on the respective model then averaged

zonally to produce the profiles shown in Fig. 7.6. The profile for NCEP Reanalysis data

in Fig. 7.6 may be verified with the findings of Mo and Higgins (1996). These profiles

show a good agreement between the CMIP5 models and the observational dataset.

However, notable differences can be seen between the observations and the CMIP5

model simulations. All of the models produce a stronger cross equatorial flow than

observations during all seasons except the northern hemisphere summer (June-August) months. Additionally, the model simulations produce a muted poleward transport from the northern midlatitudes and an amplified poleward transport from the southern midlatitudes in all seasons when compared with the observational dataset. Fig. 7.6 further decomposes the total meridional transport of water vapor into the average contributions (produced using monthly means) $< qV >$ and the sub-monthly transient eddies produced using daily average values $q'V'$. The sub-monthly contributions are significant sources of transport from the equatorial region in all seasons, and their inclusion justifies the necessity of using data archived for daily values when analyzing the quality of water transport in model simulations.

7.4   Calculation of the divergence of moisture flux

The next step in the analysis of model quality in calculating the water budget is the computation of the divergence of moisture flux term, or $\nabla \cdot \vec{Q}$. Vertical integration with respect to pressure of the water vapor balance equation combined with mass continuity leads to the mass conservation equation for water vapor in the atmosphere,

$$\frac{\partial W}{\partial t} = -\nabla \cdot \vec{Q} + E - P \qquad (7.13)$$

where E is evaporation, P is precipitation, and $\nabla \cdot \vec{Q}$ is the moisture flux divergence or net outflow of water vapor through the sides of the atmospheric column. In long-term averages, the storage and tendency terms are small and may be neglected (e.g. Huang et al. 2005, Trenberth et al. 2007). This divergence may be represented mathematically by,

$$\nabla \cdot \vec{Q} = \frac{\partial Q_u}{\partial x} + \frac{\partial Q_v}{\partial y} \qquad (7.14)$$

and measures the difference between the inflow and outflow of water vapor to the atmospheric column. A positive divergence means that outflow is greater than inflow, and a negative divergence (or convergence) means that inflow is greater than outflow. The spherical form of the divergence equation (7.4) can be derived following the methodology of Kreyzig (1993),

$$\nabla \cdot \vec{Q} = \frac{1}{R_e \cos \phi} \left(\frac{\partial Q_\lambda}{\partial \lambda} + \frac{\partial (Q_\phi \cos \phi)}{\partial \phi} \right) \qquad (7.15)$$

where R_e is the radius of the Earth taken as 6371.2 km, Q_λ and Q_ϕ are the zonal and meridional components of vapor flux, λ is longitude in radians, and ϕ is latitude in radians. The central difference approximation of 7.15 is given by

$$\nabla \cdot \vec{Q}(i,j) = \frac{1}{R_e \cos(\phi_j)} \left(\frac{Q_{\lambda(i+1,j)} - Q_{\lambda(i-1,j)}}{(\lambda_{i+1} - \lambda_{i-1})} \right.$$

$$\left. + \frac{\cos(\phi_{j+1}) Q_{\phi(i,j+1)} - \cos(\phi_{j-1}) Q_{\phi(i,j+1)}}{(\phi_{j+1} - \phi_{j-1})} \right). \qquad (7.16)$$

This calculation is performed on the selected CMIP5 models as well as NCEP observational reanalysis data for comparison. The results are shown in Fig. 7.7. The general behavior of the global moisture flux calculated using observational data is well reproduced by the moisture flux computed with CMIP5 model simulation data. Fig. 7.7 gives another good indicator of model quality in producing Hadley circulation. Shaded areas denote a negative moisture flux divergence from the atmospheric column, indicating inflow of water vapor to the region. White areas denote a positive moisture flux divergence which indicates an outflow of water vapor. Moisture in the atmosphere is concentrated in the tropics, while the subtropical regions exhibit expected patterns of drying.
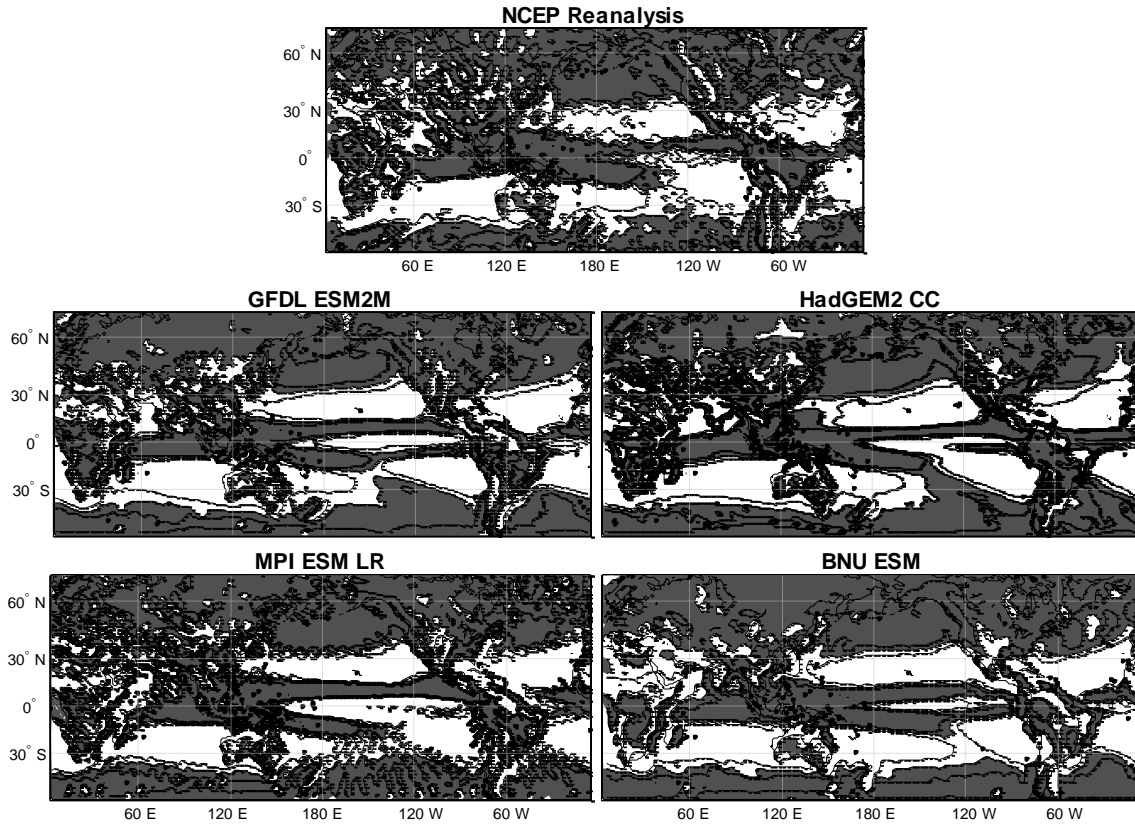
Fig. 7.7 The global annual divergence of moisture flux averaged from 1981-2000 using CMIP5 models ('historical' simulation runs) and NCEP Reanalysis I observational data. Contour interval is 1 mm/day. Shading indicates negative values.

7.5   Decomposition of the moisture convergence trend

The trend in moisture convergence is defined as the difference between a time-averaged future state and present (or past) state. For a complete qualitative analysis of these terms and their contributions to the water vapor transport, the convergence of moisture can be further decomposed into terms related to the change in circulation (the dynamical change) and the change in concentration of water vapor (the thermodynamic change). Following the methodology by Seager et al. (2007), the change in the convergence of moisture can be approximated by,

$$-\delta(\nabla \cdot \boldsymbol{V}q) \approx -\nabla \cdot (q_P \delta \boldsymbol{V} + \boldsymbol{V}_P \delta q) \qquad (6.1)$$

where q_P and V_P represent the present values of atmospheric humidity and flow, and δq and δV represent the future – present trend in these values, respectively. The first term on the right-hand side of (6.1) approximates the contribution from the change in mean circulation, and the second term approximates the contribution from the change in mean humidity. Specifically, these terms show the contributions from model forcings of the individual water vapor transport terms on the convergence of moisture in the atmosphere. Fig. 7.8 shows the total trend and term decomposition of vertically integrated zonal averaged meridional water vapor transport between future (2081-2100) and present (1981-2000) epochs. The strongest trend in poleward water vapor transport is due to the dynamical change $q_P\delta V$ for all models; this result is demonstrated in the similarity between the total trend and the trend in dynamical change profiles. Most models agree on the sign of the change and general magnitude; however, the HadGEM2 CC model produces a much more intense annual response of equatorial transport to climate change than the other models. The zonal average meridional transport profile of the thermodynamic change $V_P\delta q$ demonstrates much weaker model agreement in both magnitude and intensity with strong seasonal variation between models. Fig. 7.9 depicts the global trend in moisture convergence decomposed into the dynamical and thermodynamical change terms for the same time periods. Here, the motions due to changes in mean humidity dominate moisture transport with most intense changes occurring over the equatorial region. The top four panels in Fig. 7.9 of the trend in moisture convergence closely resemble the 1981-2000 pattern depicted in Fig. 7.7, signifying that the trend of the global pattern of atmospheric water vapor remains largely the same in response to climate change, and the global structure of moisture transport is

113

most dependent on the atmospheric water vapor. These figure demonstrates the importance of including the term for ($q'\boldsymbol{V'}$) sub-monthly variations in the calculations of total moisture flux convergence, as this term is not negligible. The recent study by Hsu et al. (2013) included calculations of moisture flux convergence values for many CMIP5 models, but since daily archived simulation data is not available for these models, these values exclude the contributions due to high-frequency eddies. The values presented here for the selected models for both present climatology (Figs. 7.6 and 7.7) and decomposition of trend (Figs. 7.8 and 7.9) are thus more accurate than those published in the Hsu et al. (2013) study.
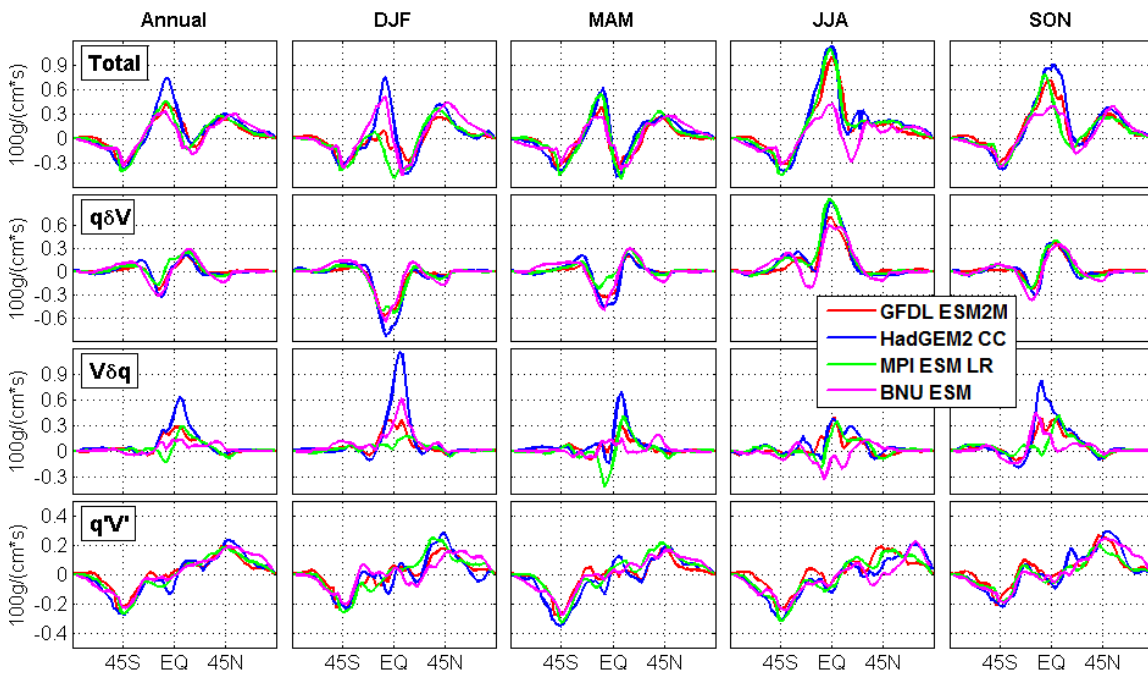
Fig. 7.8 Seasonal decomposition of the future minus present trend in vertically integrated meridional profiles of the zonal mean seasonal northward transport of water vapor into change in specific humidity $\boldsymbol{V}_P \delta q$, the change in mean circulation $q_P \delta \boldsymbol{V}$, and transient eddies $q'\boldsymbol{V'}$ in units of 100 g/(cm*s) using the CMIP5 model RCP 4.5 emissions scenario for future (2081-2100) and 'historical' simulation runs for past (1981-2000) epochs.

114
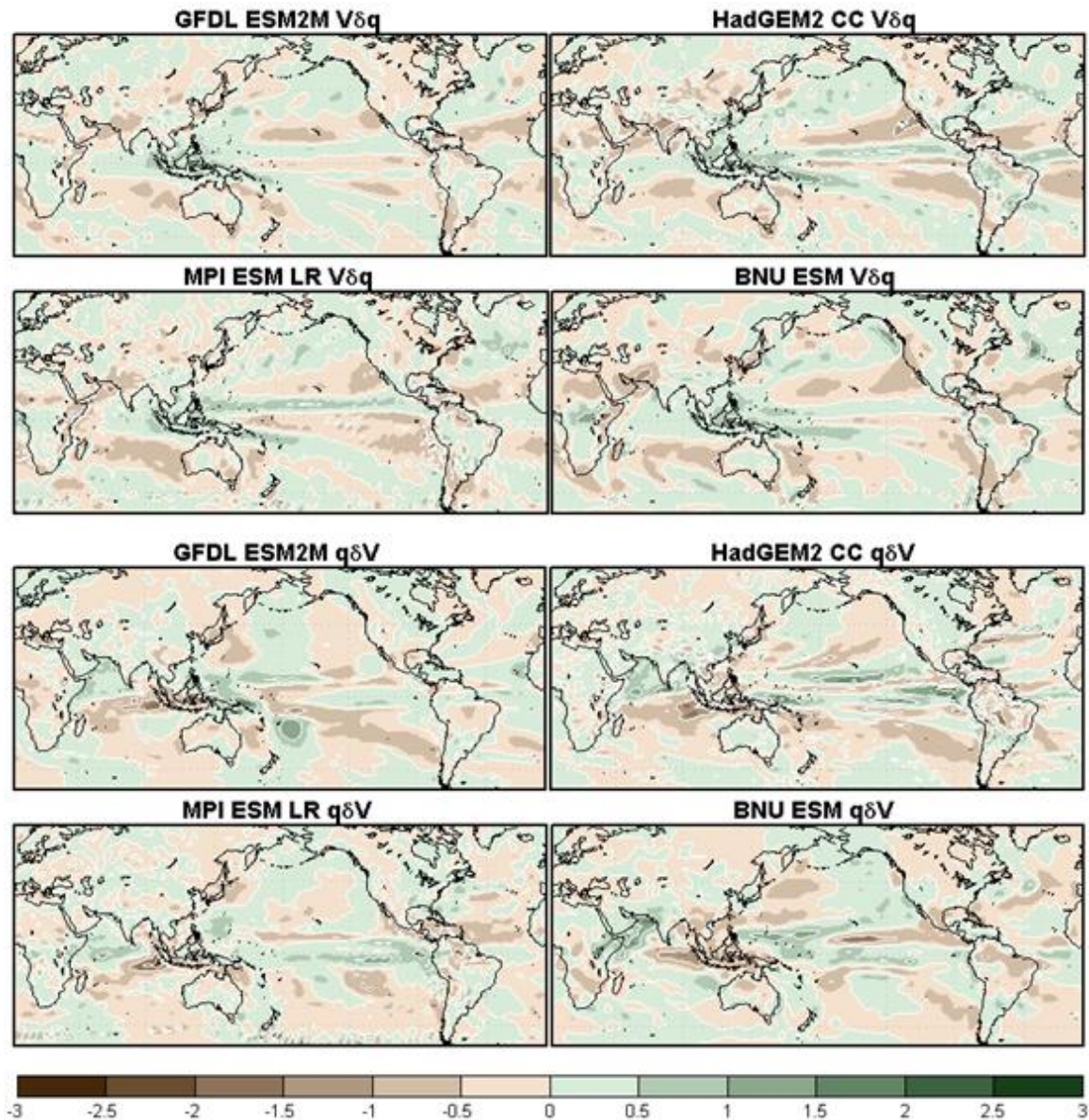
Fig. 7.9 Decomposition of the trend in moisture convergence into the change in specific humidity (top four panels) and the change in mean circulation (bottom four panels) calculated as the difference between CMIP5 model RCP 4.5 emissions scenario for future (2081-2100) and 'historical' simulation runs for past (1981-2000) epochs. Shading contours in mm/day.

115

CHAPTER 8

IDENTIFYING MODEL RESPONSE TO CLIMATE CHANGE

The final step in this project examines the production of precipitation within the atmospheric component of climate models by identifying a link between greenhouse gas (GHG) emissions and simulated precipitation. A direct consequence of changing atmospheric concentrations of GHGs is seen in the increased net radiation acting on the climate system, causing a warming of surface conditions. One method for modeling these effects is to isolate the atmospheric response to forced changes in sea surface temperature (SST). Using this method, the following study discusses the results of simulations generated by in-house model runs of the NCAR CAM 3.1 atmospheric general circulation model (AGCM) forced by an SST boundary condition. The SST trend data which provides the forcing for the AGCM simulations is derived from selected CMIP5 coupled atmosphere-ocean general circulation models (AOGCMs). Global patterns of the 21st century minus 20th century trend in precipitation are shown to be reasonably well reproduced using the AGCM and the SST trend forcing. Comparisons of regional precipitation trends, however, do show large differences between the AGCM simulations and fully-coupled AOGCM output for each model, indicating the limitations of SST control on regional precipitation.

8.1   Introduction

The understanding of temperature variations in the climate system as a response to the effects of climate change has improved with each new iteration of the model ensembles. Climate sensitivity to changes in radiative forcing due to higher atmospheric

greenhouse gas concentrations is well understood, and the sign and magnitude of the changes can be predicted with high confidence. An immediate response to increased radiative forcing is a warming of global surface temperatures, with land surfaces changing at a faster rate than oceans and the Northern Hemisphere experiencing the highest degree of warming (Solomon et al. 2007, sec. 10.3). While ocean warming occurs more slowly than on land, the changes have a robust effect on the atmosphere. Heating at the Earth's surface affects evaporation and sensible heating and increases the capacity of the atmosphere to retain moisture. These changes alter the global hydrological cycle and shape the patterns and intensity of precipitation.

The correlation between the observed trends in precipitation and the trend in SST has been examined for multiple regions. For example, Hoerling and Kumar (2003) demonstrate how the SST of the Indian Ocean influenced the post-1998 North American drought. Huang et al. (2009) examine how an atmospheric model forced with a tropical Atlantic SST gradient hindcast experiment may be used to study the influences on South American rainfall. Schubert et al. (2009) compare precipitation responses to SST forcing patterns in five selected atmospheric general circulation models and in NCEP Reanalysis observational data. It has also been shown that climate models exhibit well-known biases in the simulation of SST. For example, the models have displayed the tendency to produce a feature known as the equatorial Pacific "cold tongue" which extends too far west at colder temperatures than observation (Davey et al. 2002, Cai et al. 2003). This feature causes the model maximum SST (e.g. the Pacific warm pool) to become displaced too far west; the unrealistic displacement of the South Pacific convergence zone (SPCZ), evident as the well-known climate model issue which leads to the generation of an

incorrect double-band pattern of the intertropical convergence zone (ITCZ), has been shown to be linked to model bias in tropical rainfall patterns (Cai et al. 2009). The unrealistically warm SST in the southern ocean, incorrect zonal pattern of the SPCZ, and the double ITCZ are all common features in GCMs which have been studied in CMIP3 and previous archives (e.g. Davey et al. 2002, Meehl et al. 2005, Lin 2007), and preliminary analyses indicate that these issues have not significantly improved in the CMIP5 ensemble (Meehl et al. 2012).

8.2   Numerical experiments

The use of fully-coupled climate model output SST trends as a forcing for atmospheric model simulations is inspired by Stephenson and Held (1993), who showed that many climate features can be reproduced using an atmospheric model. A similar analysis of the new CMIP5 archive provides the most updated results on this type of study. The selected models from the CMIP5 ensemble are all the newest type of GCMs, the Earth System models (ESMs, described in section 2.4.1); simulations forced by these models will provide valuable insight regarding the progression of global climate model quality. The list of CMIP5 models and their respective native resolutions is shown in Table 2.6. In order to isolate the atmospheric response to a forced SST, the simulations are executed using the NCAR CAM 3.1 atmospheric model which has a spectral T42 resolution and 26 vertical pressure levels (performed by Houk Paek, see Paek 2013). The NCAR CAM 3.1 model represents the atmospheric component of the NCAR CCSM4 fully-coupled model in CMIP5 (see section 2.4.1). Unlike a fully-coupled climate model in which the model components may pass information to each other and mutually adjust,

118

the atmospheric model treats the ocean component as a boundary condition. The imposed SST does not change based on the atmospheric response, but rather, it acts as a lower boundary forcing which drives an atmospheric response. The values for SST are long-term means derived from simulations of selected CMIP5 models. The model is initialized with default conditions except for the values of SST and sea ice concentrations which are taken from the selected CMIP5 model simulation outputs, then simulations are performed for 30-year runs for each model using both a present (1981-2000) simulated state (with CMIP5 'historical' runs providing the long-term mean) and a future (2081-2100) simulated state (the RCP 8.5 simulation data is selected for the future since this scenario depicts the highest radiative forcing response to greenhouse gas emissions of the CMIP5 RCP scenario sets, producing the most pronounced simulated response). The trend in SST is the difference between these long-term means. Thus, the CAM 3.1 simulated precipitation response to the SST trend represents the precipitation trend attributed to the CMIP5 coupled climate model emissions scenario forcing.

Initial analyses of the AGCM simulations indicate that certain atmospheric quantities are qualitatively well-produced in the runs forced by the SST trend. Paek and Huang (2013, in preparation) have shown that the global pattern of atmospheric zonal wind and angular momentum determined from simulation data may be verified with observations. These findings confirm that the atmospheric model simulations produce realistic data when forced with the CMIP5 SST trend. The analysis of the precipitation trend within these runs provides further insight regarding the diverse behavior of precipitation in climate model simulations. Conceptually, this analysis demonstrates how a warmer climate heats the oceans, and the change in SST influences the atmospheric

Institute	Model	Resolution
Canadian Centre for Climate Modelling and Analysis (CCCMA)	CanESM2	1.875°×1.875° L35
National Center for Atmospheric Research (NCAR)	CCSM4	1.25°×0.9° L26
Geophysical Fluid Dynamics Laboratory (GFDL)	GFDL-ESM2M	2.5°×2.5° L35
Met Office Hadley Centre (MOHC)	HadGEM2-ES	1.875°×1.25° L38
Atmosphere and Ocean Research Institute (The University of Tokyo), National Institute for Environmental Studies, and Japan Agency for Marine-Earth Science and Technology (MIROC)	MIROC-ESM	2.8°×2.8° L80
Max Planck Institute for Meteorology (MPI-M)	MPI-ESM-LR	1.875°×1.875° L47

Table 8.1: CMIP5 climate models which are used for analysis in this study, shown with their respective modeling centers and horizontal resolutions (Paek and Huang 2013).

branch of the hydrological cycle through the circulation of moisture, resulting in global changes in precipitation. The precipitation trend generated by the SST trend demonstrates one pathway which connects climate change, represented by the radiative forcing within the models, to a corresponding change in model simulated global precipitation. While each model is forced with the same globally uniform radiative forcing, the SST response from this forcing, and ultimately the resulting precipitation response, will vary among models. Thus, performing simulations which demonstrate the precipitation response to CMIP5 model-generated SST provides an excellent tool for illustrating the effects of climate change.

8.3   Global precipitation response to SST trend

Preliminary analyses of the CMIP5 archive indicate a robust global precipitation response to a warming climate as a positive trend over the wet tropical regions (especially the equatorial Pacific Ocean and the Asian monsoon regions) and a negative trend over the land areas of the subtropics (Lau et al. 2013) following a similar global pattern indicated by the previous CMIP3 archive (Seager et al. 2007, Karl et al. 2009). Fig. 8.1

demonstrates how this pattern in precipitation response can be replicated using an SST trend-forced AGCM. For example, the common feature of the equatorial Pacific maximum trend is present in both the AGCM precipitation responses and the corresponding AOGCM fully-coupled simulated trends. General global zonal mean patterns of precipitation responses also show agreements between the two sets of simulations (Fig. 8.2); both sets of simulations predict increased annual precipitation in the tropics and high latitudes and drying trends in the midlatitude subtropical dry zones. The zonal profile of each 5-model mean indicates that the AGCM simulations project higher magnitudes of precipitation increases globally except over the Southern Ocean. The AGCM runs forced using SST data from the HadGEM2 ES model predicts the most intense response in annual tropical precipitation at nearly a 2 mm/day increase over a zonal band slightly north of the equator. Precipitation trends from the AGCM runs forced using SST data from the GFDL ESM2M model show the most muted global responses of the five models.

While the previous experiments by Stephenson and Held (1993) do show that many atmospheric features can be reproduced using SST boundary conditions as AGCM forcings, it should be noted that these experiments were performed using the atmospheric components of the CMIP3 models which they tested, and the results were compared to each model's fully-coupled counterpart. Since this study is limited to all simulations being performed using one model (NCAR CAM 3.1), the results are limited by this model's native resolution and parameterization schemes which contribute sources of bias. The individual models cannot be as easily compared with their AOGCM counterparts due to the inherent differences between them and the NCAR model. Nevertheless, the
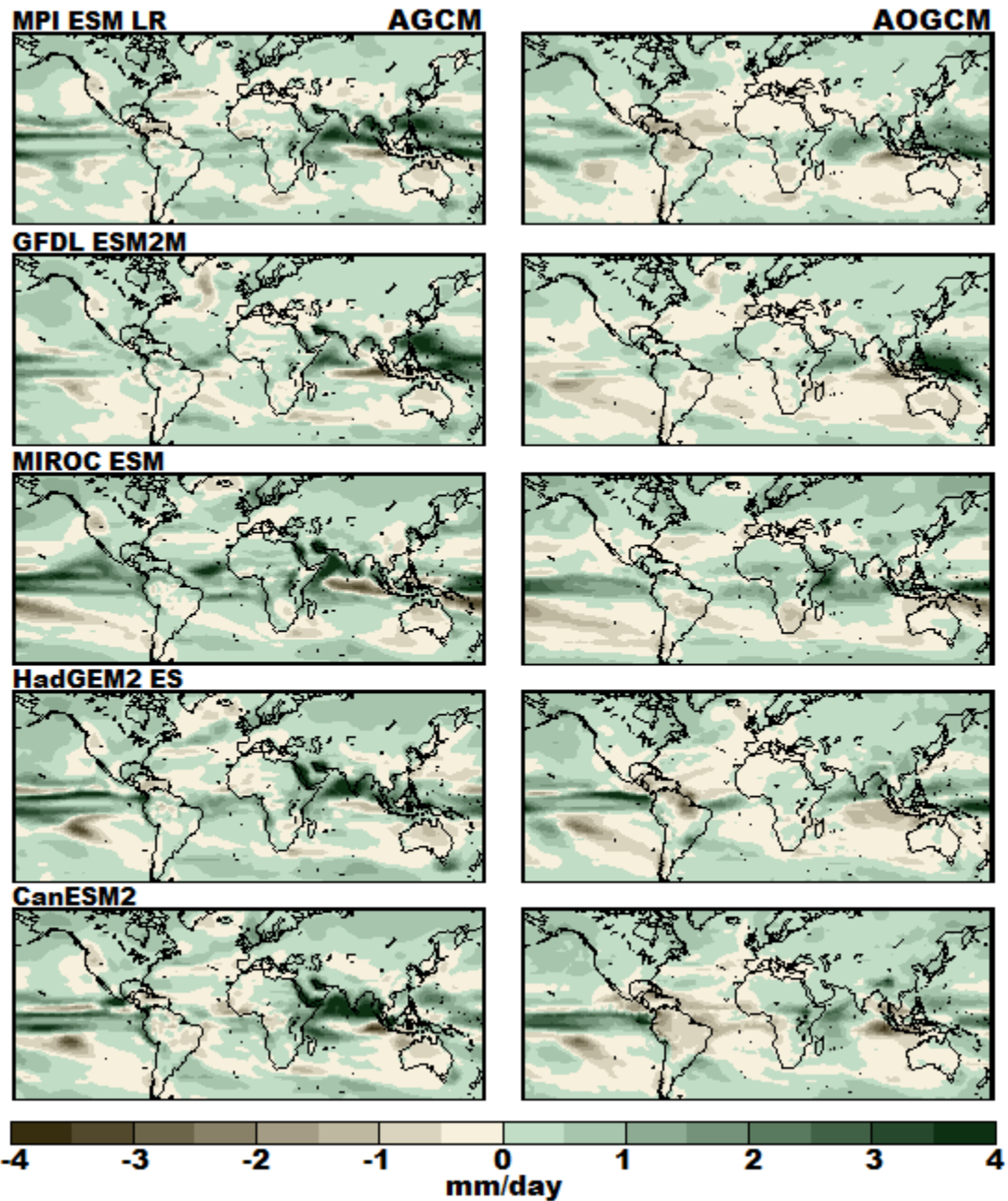
Fig. 8.1 Mean annual global precipitation responses produced using NCAR CAM 3.1 AGCM forced by model SST trends (left column) and the fully-coupled AOGCM simulation output (right column) calculated as average future (2081-2100, RCP 8.5 simulations) minus present (1981-2000, 'historical' simulations).
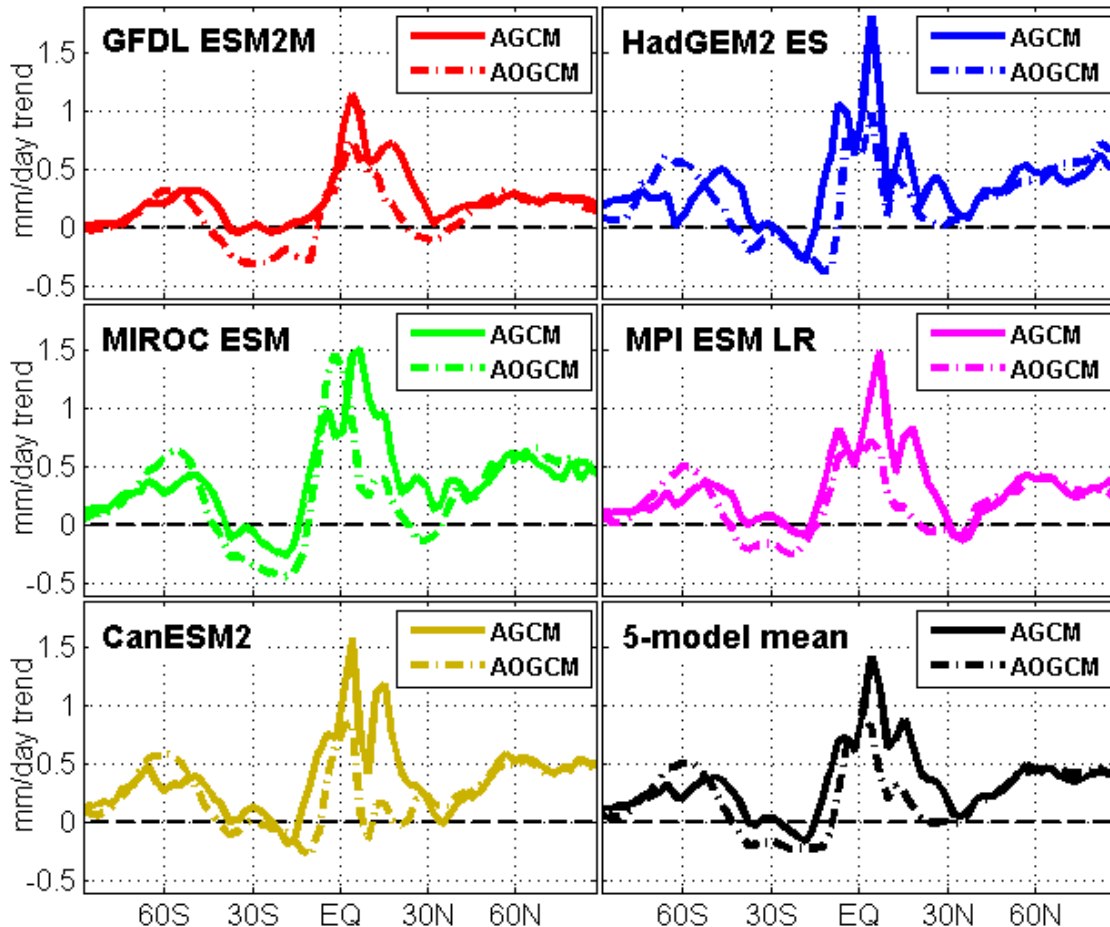
Fig. 8.2 Zonal mean annual global precipitation responses produced using NCAR CAM 3.1 AGCM forced by model SST trends and the fully-coupled AOGCM simulation output calculated as average future (2081-2100, RCP 8.5 simulations) minus present (1981-2000, 'historical' simulations) for each CMIP5 model and the 5-model mean.

agreement on a global scale between the AGCM and AOGCM simulated precipitation trends indicates that these differences are reasonably small.

Lee and Wang (2012) note in their analysis of CMIP5 that the center of increased precipitation over the equatorial Pacific is located further east in CMIP5 than CMIP3. They hypothesize that the differences may be related to the changes in SST mean field over the equatorial Pacific region. Fig. 8.1 confirms that the equatorial Pacific precipitation trend maximum exhibits an amplified eastern response; since this feature

123

has been reproduced here using only an atmospheric model and forced CMIP5 SST trends, the results of this study lend credibility to their hypothesis.

8.4   Regional precipitation response to SST trend

Regional patterns of rainfall have not been shown to be strongly correlated to global changes in SST (e.g. Ruff et al. 2012 found no coherent connections between the patterns of interannual precipitation for the southwestern US and global SST for the same time set) since regional precipitation trends over land are more directly influenced by changes in atmospheric circulation and moisture (such as the projected poleward expansion of subtropical dry zones, Scheff and Frierson 2012), and are dependent on local topography, land use, and vegetation (Solomon et al. 2007, Ch.11). As a result, the regional precipitation responses to forced SST in the AGCM simulations are not expected to closely resemble those produced using the AOGCMs.

Annual trends in precipitation over North America are projected to be positive for most of the continent and negative over the southernmost portion which encompasses much of the southwestern US by both the CMIP3 (Solomon et al. 2007) and CMIP5 (Seager et al. 2012) ensemble means. Individual model output of the CMIP5 AOGCMs depicted in Fig. 8.3 typically follows this pattern in moisture trends with some uncertainty between models regarding the sign of the change, especially in the northwestern portion of the region in which some models (GFDL ESM2M, MIROC ESM, HadGEM2 ES) project a drying trend while others project a mixed region of wet and dry trends (MPI ESM LR) or even a strong moistening trend (CanESM2). The precipitation response generated by the AGCM, however, depicts an intense negative trend (-0.5 to -

1.3 mm/day) over the northwest portion of the region and a generally uniform positive trend in annual precipitation. Inspection of the monthly trends for an area averaged box over the southwestern US (30N-40N, 120W-95W) reveals little resemblance between the annual profiles of the AGCM and AOGCM means. A comparison of the individual models shows that certain features are reproduced, however; for example, the MPI ESM LR model experiences a minimum precipitation trend in late summer/early fall in both the coupled AOGCM output and the response simulated in the AGCM, and the MIROC ESM model experiences a maximum trend in October for both simulation sets. These similarities could be an indication of teleconnections between the SST trends and a precipitation response in this region.

The Mediterranean region is also projected to become drier in the 21st century with the sign and magnitude of this trend maintained both spatially and seasonally (Kelley et al. 2012). Individual model output of coupled AOGCMs shows a relatively high degree of certainty in the CMIP5 archive, with a reduced spread compared to the precipitation trends forecasted for the southwestern US region (see section 6.3). Fig. 8.4 confirms these results in the selected CMIP5 models, depicting nearly uniform annual drying trends from the AOGCM simulations. The AGCM simulations again fail to capture the regional pattern of precipitation trends. Interestingly, while there is some disagreement between models over the spatial patterns of annual precipitation responses, the monthly profiles reveal a strong agreement in the seasonal pattern for all tested models. Positive precipitation responses in the Mediterranean region (30N-45N, 5E-35W) to forced SST conditions happen entirely during the summer and fall seasons, with a maximum for all models occurring in August. This robust signal could be an indication of

a shared aspect between the tested models, or it could indicate a systematic bias inherent

to the NCAR CAM 3.1 model.
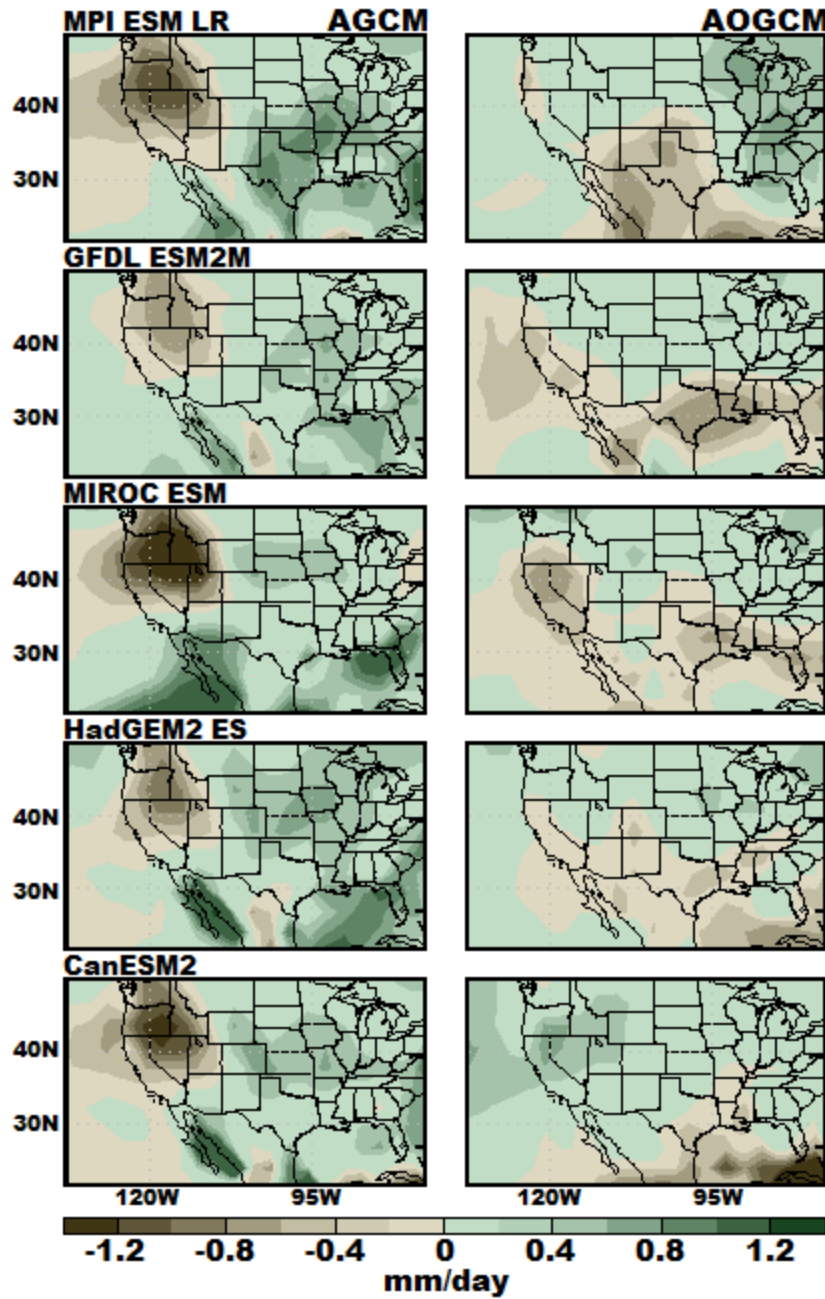
Fig. 8.3 Mean annual precipitation responses for the southwestern US region produced using NCAR CAM 3.1 AGCM forced by model SST trends (left column) and the fully-coupled AOGCM simulation output (right column) calculated as average future (2081-2100, RCP 8.5 simulations) minus present (1981-2000, 'historical' simulations).
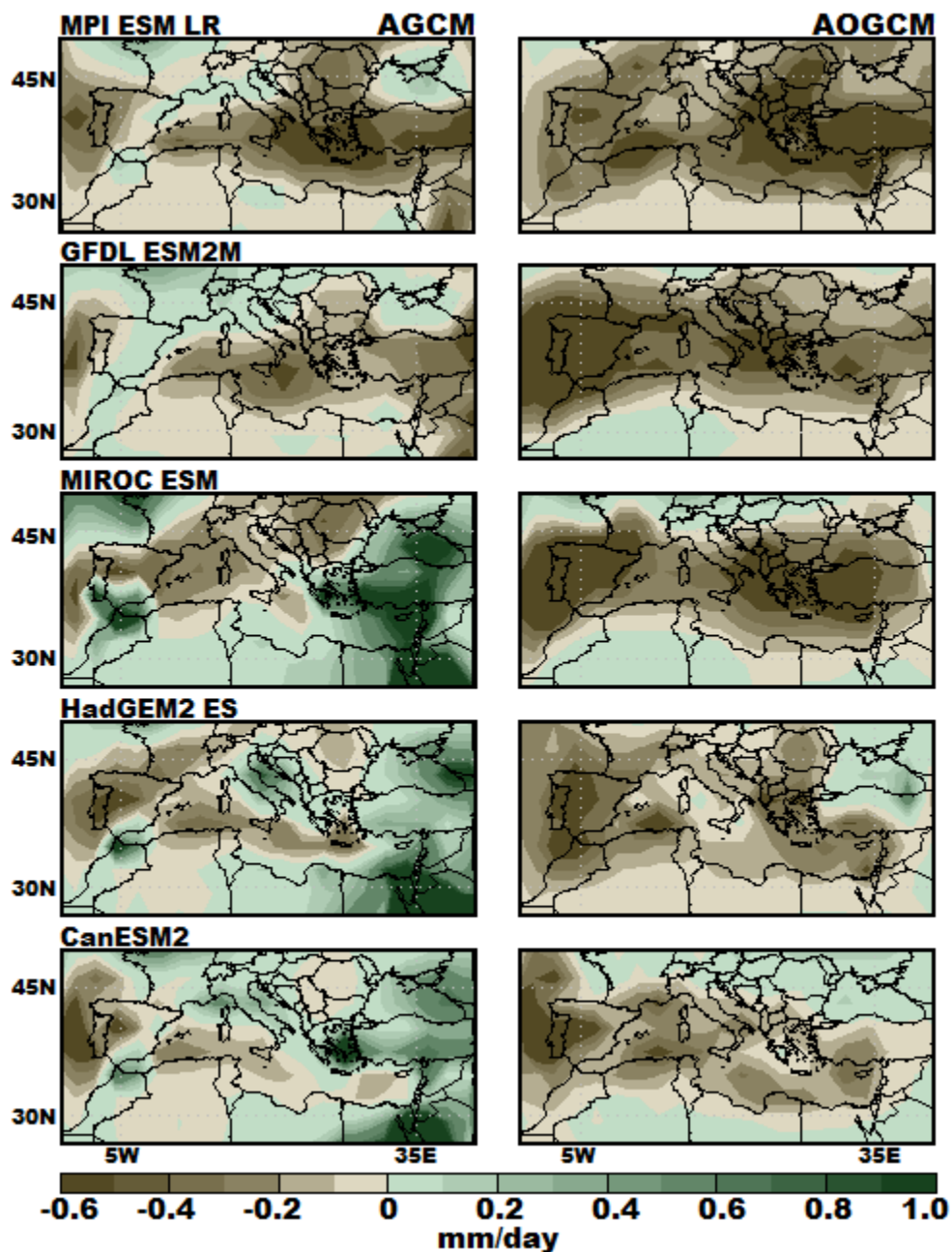
Fig. 8.4 Mean annual precipitation responses for the Mediterranean region produced using NCAR CAM 3.1 AGCM forced by model SST trends (left column) and the fully-coupled AOGCM simulation output (right column) calculated as average future (2081-2100, RCP 8.5 simulations) minus present (1981-2000, 'historical' simulations).
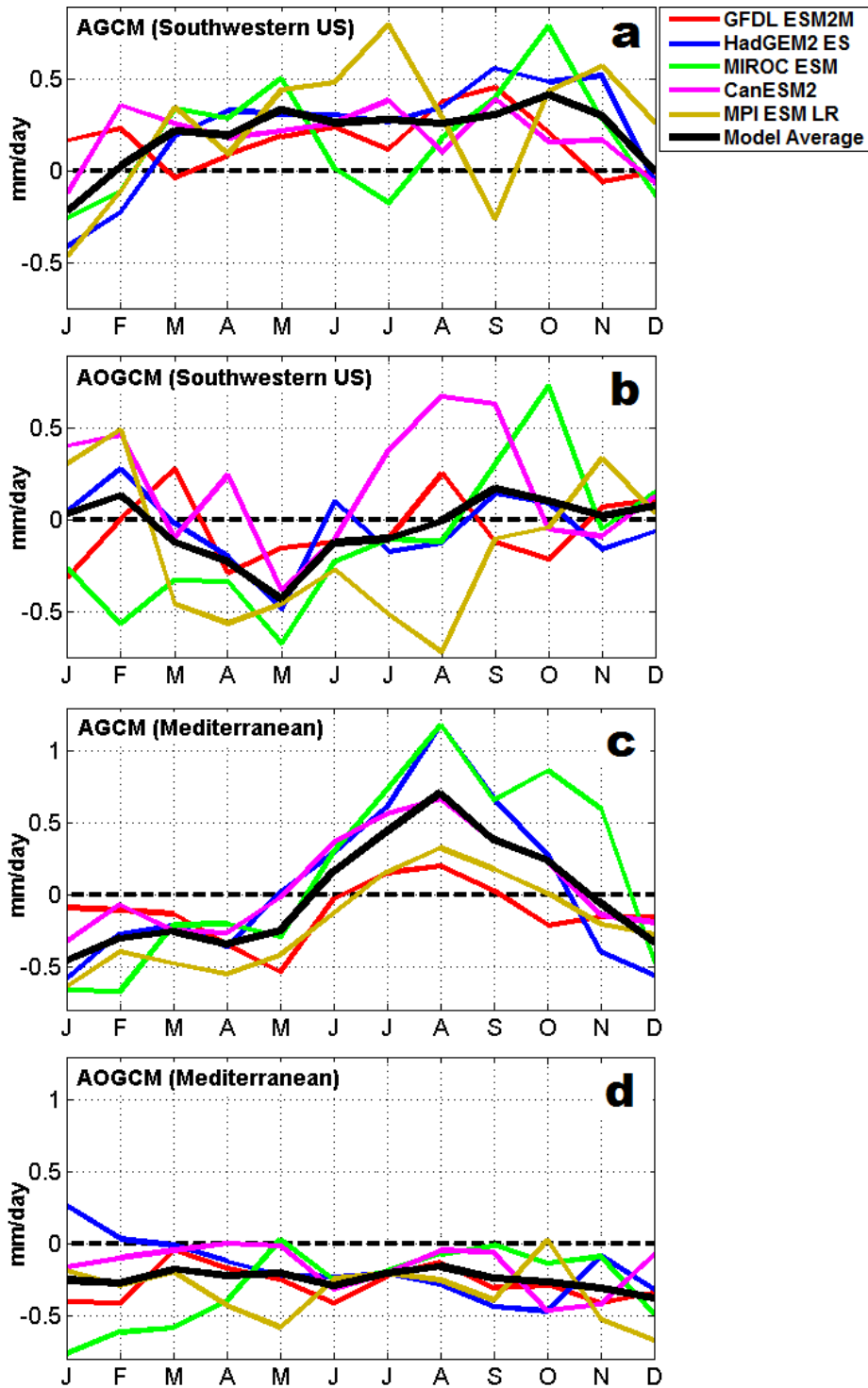
Fig. 8.5 Annual profiles of monthly precipitation responses area-averaged for the southwestern US (30N-40N, 120W-95W) and Mediterranean (30N-45N, 5E-35W) regions produced using NCAR CAM 3.1 AGCM forced by model SST trends (a,c) and the fully-coupled AOGCM simulation output (b,d) calculated as average future (2081-2100, RCP 8.5 simulations) minus present (1981-2000, 'historical' simulations).

8.5   Conclusions

This chapter provides detailed studies of particular model bias associated with the production of precipitation in an atmospheric climate model. The results are highly beneficial to model development and provide a deeper understanding of the sources of individual model bias. The study has demonstrated that the global pattern of precipitation trends over the 21st century can be reproduced reasonably well using a decoupled atmospheric component model and SST trend values as a boundary condition. The annual mean trends in precipitation are predicted to increase between the 20th and 21st century, and the large-scale structure of these trends is maintained when comparing AGCM simulations with the fully-coupled model output. Maximum precipitation increases are projected to occur near the equator and tropics, and precipitation decreases of a much smaller magnitude are forecasted for the midlatitudes by both sets of simulations. However, the patterns of regional precipitation responses to a forced SST boundary condition do not share meaningful similarities with the regional trends simulated by a fully-coupled model. Comparisons of individual models do show some similarities between data derived for each model from the two types of simulations such as local maximum or minimum seasonal precipitation response, but it is unclear if these similarities are actually due to SST teleconnections to regional precipitation. The stronger correlation between SST trends and global patterns of precipitation responses indicates that a SST-forced AGCM can be effectively used for modeling the direct global effects of surface warming attributed to the GHG-caused climate change.

CHAPTER 9

RECOMMENDATIONS

The results of the studies performed for this project are highly beneficial for climate model developers, for the scientific community, and for local stakeholders and water resource managers who wish to construct accurate projections of future climate conditions. This project has demonstrated both the systematic bias of the water cycle in climate models as well as a viable, useable alternative for constructing climate projections which corrects for this bias. Chapters 4 and 5 provide the alternative method for constructing climate projections which is described in detail for the direct implementation by communities in need of water resource management as well as the scientific community. Chapters 6, 7, and 8 provide more detailed analyses of both individual models and model archives which identify particular sources of model bias; these studies are relevant both to the model developers who will work on future improved versions of the models, and to communities to help identify particular strengths and weaknesses of the models or model archives for their region which are optimal for their needs. It is my recommendation that both the climate community and water managers consider my alternative model averaging method when constructing climate projections based on the studies given in Chapters 4 and 5, since this new method corrects for model bias and may produce more accurate projections than the currently used methods for model averaging. For more in-depth discussions of particular sources of model bias, I recommend reading the studies provided in Chapters 6-8 and considering strengths and weaknesses of the tested climate models when constructing climate projections.

SUMMARY

The quality of climate simulations of the water cycle in global general circulation models has been evaluated. It is found that the models, on average, show an increasing ability to accurately simulate present hydroclimatic conditions. However, analyses of precipitation indicate systematic biases between simulations and observed climatology which inherently exist in the models due to limited resolutions and simplifications of the dynamic and thermodynamic processes. These biases have not significantly improved in the most updated set of models. Individual models also exhibit a wide variety of behavior which is an indicator of the uncertainty of simulations. A deeper inspection of multiple quantities related to the water cycle reveals sources of bias in simulations of 20th century climate: the tested models tend to underproduce the concentration of atmospheric water vapor but overproduce the zonal mean poleward transport of water vapor, especially in cross equatorial flow. The combination of these biases leads to an average global overproduction of precipitation. While the general flow patterns and global structure of atmospheric moisture transport is relatively well reproduced in climate models, on a regional scale, the errors due to model bias become much more significant. When modeling centers develop approaches for improving climate model simulations of precipitation, it will be necessary for them to consider the biases of all variables related to the moisture budget, not just the precipitation quantity. This project has demonstrated the importance of identifying multiple sources of bias in the full equation for global moisture transport for consideration when improving model quality.

Despite the presence of inherent model bias, this project gives evidence that climate models are still beneficial tools for studying climate processes and projecting

131

future conditions when the knowledge of these biases are incorporated into projections. A new approach is presented for ensemble averaging climate models for producing future projections which utilizes observed climatological information and acts as a form of bias correction. The approach can easily be implemented by local water resource managers and stakeholders to whom the new climate projections could be highly beneficial, as these projections demonstrate small but significant differences on a regional scale which would have strong impacts on local water supply.

REFERENCES

Annan, J. D., and J. C. Hargreaves, 2010: Reliability of the CMIP3 ensemble, *Geophys. Res. Lett.*, **37**, L02703, doi:10.1029/2009GL041994.

Adler, R.F., G.J. Huffman, A. Chang, R. Ferraro, P. Xie, J. Janowiak, B. Rudolf, U. Schneider, S. Curtis, D. Bolvin, A. Gruber, J. Susskind, P. Arkin, 2003: The Version 2 Global Precipitation Climatology Project (GPCP) Monthly Precipitation Analysis (1979-Present), *J. Hydrometeor.*, **4**,1147-1167.

Arakawa, A., and W. H. Schubert, 1974: Interaction of a cumulus cloud ensemble with the large-scale environment, Part I, *J. Atmos. Sci.*, **31**, 674–701.

Baker, N.C., and H.-P. Huang, 2012: A comparison of absolute and relative changes in precipitation in multi-model climate projection, *Atmos. Sci. Lett.*, **13**, 174-179.

Barnett, T. P., and D. W. Pierce, 2008: When will Lake Mead go dry?, *Water Resour. Res.*, **44**, W03201, doi:10.1029/2007WR006704.

Betts, A. K., 1986: New convective adjustment scheme, Pt. 1, Observational and theoretical basis, *Quart. J. Roy. Meteor. Soc.*, **112**, 677–691.

Blázquez, J., and M. N. Nuñez, 2012: Analysis of uncertainties in future climate projections for South America: comparison of WCRP-CMIP3 and WCRP-CMIP5 models. *Climate Dyn.*, 1-18.

Bony, S., and K. A. Emmanuel, 2001: A parameterization of the cloudiness associated with cumulus convection: Evaluation using TOGA COARE data, *J. Atmos. Sci.*, **58**, 3158–3183.

Cai, W., M. A. Collier, H. B. Gordon, and L. J. Waterman, 2003: Strong ENSO variability and a super-ENSO pair in the CSIRO Mark 3 coupled climate model, *Mon. Wea. Rev.*, **131**, 1189-1210.

Cai, W., A. Sullivan, and T. Cowan, 2009: Rainfall teleconnection with Indo-Pacific Variability in the WCRP CMIP3 models, *J. Clim.*, **22**, 5046-5071.

Covey, C., K. M. AchutaRao, U. Cubasch, P. Jones, S. J. Lambert. M. E. Mann, T. J. Phillips, and K. E. Taylor, 2003: An overview of results from the Coupled Model Intercomparison Project (CMIP), *Global Planet. Change*, **37**, 103-133.

Dai, A., 2006: Precipitation Characteristics in Eighteen Coupled Climate Models, *J. Clim.*, **19**, 4605-4630.

Davey, M. K., and coauthors, 2002: STOIC: A study of coupled model climatology and variability in tropical ocean regions, *Climate Dyn.*, **18**, 403-420.

Del Genio, A. D., and M.-S. Yao, 1993: Efficient cumulus parameterization for long-term climate studies: The GISS scheme. The Representation of Cumulus Convection in Numerical Models, *Amer. Meteor. Soc.*, 181–184.

Diamond, H.J., and C.J. Lief, 2009: A Comprehensive Data Portal for Global Climate Information. *Eos, Transactions, American Geophysical Union*, **90**, 341.

Dominguez, F., J. Cañon, and J. Valdez, 2010: IPCC-AR4 climate simulations for the Southwestern US: the importance of future ENSO projections, *Climatic Change*, **99**, 499-514.

Emanuel, K. A., 1991: A scheme for representing cumulus convection in large-scale models, *J. Atmos. Sci.*, **48**, 2313–2335.

Emori, S., T. Nozawa, A. Numaguti, and I. Uno, 2001: Importance of cumulus parameterization for precipitation simulation over East Asia in June, *J. Meteor. Soc. Japan*, **79**, 939–947.

Giorgi, F., and L. O. Mearns, 2002: Calculation of average, uncertainty range and reliability of regional climate changes from AOGCM simulations via the 'reliability ensemble averaging' (REA) method, *J. Clim.*, **15**, 1141–1158.

Grandpeix, J. Y., V. Phillips, and R. Tailleux, 2004: Improved mixing representation in Emanuel's convection scheme, *Quart. J. Roy. Meteor. Soc.*, **130**, 3207–3222.

Gregory, D., and P. R. Rowntree, 1990: A mass flux convection scheme with representation of cloud ensemble characteristics and stability dependent closure, *Mon. Wea. Rev.*, **118**, 1483–1506.

Gregory, D., R. Kershaw, and P. M. Inness, 1997: Parameterization of momentum transport by convection II: Tests in single column and general circulation models, *Quart. J. Roy. Meteor. Soc.*, **123**, 1153–1183.

Held, I. M., and B. J. Soden, 2006: Robust Responses of the Hydrological Cycle to Global Warming, *J. Clim.*, **19**, 5686-5699.

Hoerling, M., and A. Kumar, 2003: The Perfect Ocean for Drought, *Science*, **31**, 299(5607), 691-694.

Holton, J. R., 2004: *An Introduction to Dynamic Meteorology*, Elsevier Academic Press, Burlington, MA, USA.

Houghton, J.T., et al. (Eds.), 2001: *Climate Change 2001: The Scientific Basis*, Cambridge University Press, Cambridge, UK.

Hsu, P. C., T. Li, H. Murakami, and A. Kitoh, 2013: Future change of the global monsoon revealed from 19 CMIP5 models, *Journal of Geophysical Research: Atmospheres*, **118**, 1247–1260, doi:10.1002/jgrd.50145.

Huang, H.-P., R. Seager, and Y. Kushnir, 2005: The 1976/77 transition in precipitation over the Americas and the influence of tropical sea surface temperature, *Climate Dyn.*, **24**, 721–740.

Huang, H.-P., A. W. Robertson, Y. Kushnir, and S. Peng, 2009: Hindcasts of Tropical Atlantic SST Gradient and South American Precipitation: The Influences of the ENSO Forcing and the Atlantic Preconditioning, *J. Clim.*, **22**, 2405-2421.

Kalnay, E., and coauthors, 1996: The NCEP/NCAR 40-Year Reanalysis Project, *Bull. Amer. Meteor. Soc.*, **77**, 437–471.

Kanamitsu, M., W. Ebisuzaki, J. Woollen, S. K. Yang, J. J. Hnilo, M. Fiorino, and G. L. Potter, 2002: NCEP-DOE AMIP-II Reanalysis (R-2), *Bull. Amer. Meteo. Soc.*, **83**(11), 1631-1644.

Karl, T. R., J. M. Melillo, and T. C. Peterson (Eds.), 2009: *Global Climate Change Impacts in the United States*, Cambridge Univ. Press, Cambridge, UK.

Kelley, C., M. Ting, R. Seager, and Y. Kushnir, 2012: Mediterranean precipitation climatology, seasonal cycle, and trend as simulated by CMIP5, *Geophys. Res. Lett.*, **39**(21).

Kim, S. T. and J.-Y. Yu, 2012: The two types of ENSO in CMIP5 models, *Geophys. Res. Lett.*, **39**, L11704, doi:10.1029/2012GL052006.

Kitoh, A., 2012: Projections of Future Climate Change in the Asian Monsoon Region, Extended Abstract, International conference on "Opportunities and Challenges in Monsoon Prediction in a Changing Climate" (OCHAMP-2012), Pune, India, 21-25 February 2012.

Knutti, R., R. Furrer, C. Tebaldi, J. Cermak, and G. Meehl, 2010: Challenges in combining projections from multiple climate models, *J. Climate*, **23**, 2739–2758.

Knutti, R., 2010: The end of model democracy?, *Climatic Change*, **102**, S2, 395-404, doi: 10.1007/s10584-010-9800-2.

Knutti, R., D. Masson, and A. Gettelman, 2013: Climate model genealogy: Generation CMIP5 and how we got there, *Geophys. Res. Lett.*, 40, 1194–1199, doi:10.1002/grl.50256.

Kreyszig, E., 1993: *Advanced Engineering Mathematics*, John Wiley & Sons, Inc, New York, NY, USA.

Lau, W. K. M., H. T. Wu, and K. M. Kim, 2013: A canonical response of precipitation characteristics to Global Warming from CMIP5 models, *Geophys. Res. Lett.*

Le Treut, H., and Z.-X. Li, 1991: Sensitivity of an atmospheric general circulation model to prescribed SST changes: Feedback effects associated with the simulation of cloud optical properties, *Climate Dyn.*, **5**, 175–187.

Lee, J. Y., and B. Wang, 2012: Future change of global monsoon in the CMIP5, *Climate Dyn.*, doi:10.1007/s00382-012-1564-0.

Liepert, B. G. and M. Previdi, 2012: Inter-model variability and biases of the global water cycle in CMIP3 coupled climate models, *Environ. Res. Lett.*, **7**, doi:10.1088/1748-9326/7/1/014006.

Lin, J. L., 2007: The double-ITCZ problem in IPCC AR4 coupled GCMs: Ocean-atmosphere feedback analysis, *J. Clim.*, **20**, 4497-4525.

Lin, J. L., B. E. Mapes, K. M. Weickmann, G. N. Kiladis, S. D. Schubert, M. J. Suarez, J. T. Bacmeister, and M. I. Lee, 2008: North American monsoon and convectively coupled equatorial waves simulated by IPCC AR4 coupled GCMs, *J. Clim.*, **21**(12), 2919–2937, doi:10.1175/2007JCLI1815.1.

Lohmann, U., and E. Roeckner, 1996: Design and performance of a new cloud microphysics parameterization developed for the ECHAM4 general circulation model, *Climate Dyn.*, **12**, 557–572.

Mariotti, A., M. V. Struglia, N. Zeng, and K.-M. Lau, 2002: The hydrological Cycle in the Mediterranean Region and implication for the water budget of the Mediterranean Sea, *J. Clim.*, **15**, 1674 – 1690.

Mariotti, A., N. Zeng, J. H. Yoon, V. Artale, A. Navarra, P. Alpert, and LZX Li, 2008: Mediterranean water cycle changes: transition to drier 21st century conditions in observations and CMIP3 simulations, *Environ. Res. Lett.*, **3**: 044001. doi:10.1088/1748-9326/3/4/044001.

Meehl, G. A. and coauthors, 2005: Overview of the Coupled Model Intercomparison Project, *Bull. Amer. Meteor. Soc.*, **86**, 89-93.

Meehl, G. A. et al., 2007: The WCRP CMIP3 multimodel dataset: A new era in climate change research, *Bull. Amer. Meteor. Soc.,* **88,** 1383–1394.

Meehl, G. A. et al., 2012: WCRP Workshop on CMIP5 Climate Model Analysis, International Pacific Research Center (IPRC), University of Hawaii, USA, http://www.wcrp-climate.org/documents/ezine/WCRPnews_14032012.pdf.

Mestas-Nuñez, A., D. Enfield, and C. Zhang, 2007: Water vapor fluxes over the Intra-Americas Sea: Seasonal and interannual variability and associations with rainfall, *J. Clim.*, **20**(9), 1,910-1,922.

Mo, K. C., and R. W. Higgins, 1996: Large-scale atmospheric moisture transport as evaluated in the NCEP/NCAR and the NASA/DAO reanalyses, *J. Climate*, **9**, 1531–1545.

Moorthi, S., and M. J. Suarez, 1992: Relaxed Arakawa–Schubert: A parameterization of moist convection for general circulation models, *Mon. Wea. Rev.*, **120**, 978–1002.

Moss, R. H., and coauthors, 2008: Towards New Scenarios for Analysis of Emissions, Climate Change, Impacts, and Response Strategies, Intergovt. Panel on Clim. Change, Geneva.

Moss, R. H., and coauthors, 2010: The next generation of scenarios for climate change research and assessment, *Nature*, **463**, 747–756, doi:10.1038/nature08823.

Nakićenović, N., J. Alcamo, G. Davis, B. de Vries, J. Fenhann, S. Gaffin, K. Gregory, A. Grubler, T. Y. Jung, T. Kram, E. L. La Rovere, L. Michaelis, S. Mori, T. Morita, W. Pepper, H. Pitcher, L. Price, K. Raihi, A. Roehrl, H-H. Rogner, A. Sankovski, M. Schlesinger, P. Shukla, S. Smith, R. Swart, S. van Rooijen, N. Victor, and Z. Dadi, 2000: IPCC Special Report on Emissions Scenarios, Cambridge University Press, Cambridge, United Kingdom and New York, NY, USA, 599 pp.

Nordeng, T. E., 1994: Extended versions of the convective parameterization scheme at ECMWF and their impact on the mean and transient activity of the model in the tropics, *ECMWF Tech. Memo.* **206**.

O'Gorman, P. A. and T. Schneider, 2009: The physical basis for increases in precipitation extremes in simulations of 21st-century climate change, *PNAS 106*, **35**, 14773–14777.

Paek, H., 2013: *Climate Variability and Trend on Interannual-to-Centennial timescales from Global Observations and Atmosphere-Ocean Model Simulations*. (Doctoral dissertation).

Paek, H., and H.-P. Huang, 2013: AGCM Response to Sea Surface Temperature of CMIP5 multi-models under radiative forcing. (In preparation).

Pan, D. M., and D. A. Randall, 1998: A cumulus parametrization with a prognostic closure, *Quart. J. Roy. Meteor. Soc.*, **124**, 949–981.

Pan, H.-L., and Wan-Shu Wu, 1994: Implementing a mass flux convective parameterization package for the NMC medium-range forecast model, Preprints, 10th Conf. on Numerical Weather Prediction, Portland, OR, Amer. Meteor. Soc., 96-98.

Parrish, D. F., and J. C. Derber, 1992: The National Meteorological Center's spectral statistical interpolation analysis system. *Mon. Wea. Rev.*, **120**, 1747–1766.

Peixoto, J. P., and A. H. Oort, 1992: *Physics of Climate*, American Institute of Physics, New York, NY.

Räisänen, J., L. Ruokolainen, and J. Ylhaisi, 2010: Weighting of model results for improving best estimates of climate change, *Clim. Dyn.* **35**: 407-422.

Rasch, P. J., and coauthors, 2006: A characterization of tropical transient activity in the CAM3 atmospheric hydrologic cycle, *J. Climate*, **19**, 2222–2242.

Reichler, T., and J. Kim, 2008: How well do coupled models simulate today's climate?, *Bull. Amer. Meteor. Soc.*, **89**, 303–311.

Reifen, C., and R. Toumi, 2009: Climate projections: Past performance no guarantee of future skill?, *Geophys. Res. Lett.*, **36**, L13704, doi:10.1029/2009GL038082.

Reynolds, R., 2000: *Cambridge Guide to Weather*, Cambridge University Press, Cambridge, UK.

Ricard, J. L., and J. F. Royer, 1993: A statistical cloud scheme for use in an AGCM, *Ann. Geophys. Atmos. Hydrosph. Space Sci.*, **11**, 1095–1115.

Rotstayn, L. D., 2000: On the "tuning" of autoconversion parameterizations in climate models, *J. Geophys. Res.*, **105**, 15495–15507.

Ruff, T. W., Y. Kushnir, and R. Seager, 2012: Comparing Twentieth-and Twenty-First-Century Patterns of Interannual Precipitation Variability over the Western United States and Northern Mexico, *Journal of Hydrometeorology*, **13**(1), 366-378.

Schaller, N., I. Mahlstein, J. Cermak, and R. Knutti, 2011: Analyzing precipitation projections: a comparison of different approaches to climate model evaluation, *J. Geophys. Res*. **116**: D10118. doi:10.1029/2010JD014963.

Scheff, J., and D. M. Frierson, 2012: Robust future precipitation declines in CMIP5 largely reflect the poleward expansion of model subtropical dry zones, *Geophys. Res. Lett.*, **39**(18).

Schubert, S. D. and coauthors, 2009: A U.S. CLIVAR project to assess and compare the responses of global climate models to drought-related SST forcing patterns: Overview and results, *J. Climate*, **22**, 5251–5272.

Seager, R., M. Ting, I. M. Held, Y. Kushnir, J. Lu, G. Vecchi, H.-P. Huang, N. Harnik, A. Leetmaa, N. C. Lau, C. Li, J. Velez, and N. Naik, 2007: Model Projections of an Imminent Transition to a More Arid Climate in Southwestern North America, *Science* **316**: 1181-1184.

Seager, R., Ting, M., Li, C., Naik, N., Cook, B., Nakamura, J., and Liu, H., 2013: Projections of declining surface-water availability for the southwestern United States, *Nature Climate Change*, **3**, 482-486.

Smith, R. N. B., 1990: A scheme for predicting layer clouds and their water content in a general circulation model, *Quart. J. Roy. Meteor. Soc.*, **116**, 435–460.

Solomon, S. et al. (Eds.), 2007: *Climate Change 2007: The Scientific Basis. Contribution of Working Group 1 to the Fourth Assessment Report of the Intergovernmental Panel on Climate Change*, Cambridge Univ. Press, Cambridge.

Sperber, K. R., H. Annamalai, I. S. Kang, A. Kitoh, A. Moise, A. Turner, B. Wang, and T. Zhou, 2012: The Asian summer monsoon: an intercomparison of CMIP5 vs. CMIP3 simulations of the late 20th century, *Climate Dyn.*, doi:10.1007/s00382-012-1607-6.

Stephenson, D. B., and I. M. Held, 1993: GCM response of northern winter stationary waves and storm tracks to increasing amounts of carbon dioxide, *J. Clim.*, **6**, 1859-1870.

Taylor, K. E., 2001: Summarizing multiple aspects of model performance in a single diagram, *J. Geophys. Res.*, **106** (D7), 7183-7192, doi: 10.1029/2000JD900719.

Taylor, K. E., R. J. Stouffer, and G. A. Meehl, 2012: An overview of CMIP5 and the experiment design, *Bull. Amer. Meteor. Soc.*, doi:10.1175/BAMS-D-11-00094.1.

Tiedtke, M., 1989: A comprehensive mass flux scheme for cumulus parameterization in large-scale models, *Mon. Wea. Rev.*, **117**, 1779–1800.

Tiedtke, M., 1993: Representation of clouds in large-scale models, *Mon. Wea. Rev.*, **121**, 3040–3061.

Tokioka, T., K. Yamazaki, A. Kitoh and T. Ose, 1988: The equatorial 30-60 day oscillation and the Arakawa-Schubert penetrative cumulus parameterization, *J. Meteor. Soc. Japan*, **6666**, 883-901.

Trenberth, K. E., and C. J. Guillemot, 1995: Evaluation of the global atmospheric moisture budget as seen from analysis, *J. Clim.*, **8**, 2225–2272.

Trenberth, K. E. and coauthors, 2002: The need for a systems approach to climate observations, *Bull. Amer. Meteor. Soc.*, **83**, 1558–1559.

Trenberth, K. E., L. Smith, T. Qian, A. Dai, and J. Fasullo, 2007: Estimates of the global water budget and its annual cycle using observational and model data, *J. Hydrometeor.*, **8**, 758–769.

Turner, B. L., and coauthors, 2003: A framework for vulnerability analysis in sustainability science, Proceedings of the National Academy of Sciences of the United States of America 100(14) (8 July), 8074-8079.

van Oldenborgh, G. J., F J Doblas Reyes, S S Drijfhout, and E Hawkins, 2013: Reliability of regional climate model trends, *Environ. Res. Lett*. **8**, 014055.

Wallace, J. M. and P. V. Hobbs, 2006: *Atmospheric Science: An Introductory Survey*, Elsevier Academic Press, Burlington, MA, USA.

Washington, W. M. and C. L. Parkinson, 2005: *An Introduction to Three-Dimensional Climate Modeling*, University Science Books, Sausalito, CA, USA.

Weigel, A. P., R. Knutti, M. A. Liniger, and C. Appenzeller, 2010: Risks of Model Weighting in Multimodel Climate Projections, *J. Climate*, **15**, 4175-4191.

Wilson, D. R., and S. P. Ballard, 1999: A microphysically based precipitation scheme for the UK Meteorological Office Unified Model, *Quart. J. Roy. Meteor. Soc.*, **125**, 1607−1636.

Wu, P., and coauthors, 2005: Human influence on increasing Arctic river discharges, *Geophys. Res. Lett.*, **32**, L02703, doi:10.1029/2004GL021570.

Xie, P., and P. A. Arkin, 1997: Global precipitation: a 17-year monthly analysis based on gauge observations, satellite estimates, and numerical model outputs, *Bull. Amer. Meteor. Soc*. **78**: 2539-2558.

Xu, Y., X. Gao, and F. Giorgi, 2010: Upgrades to the reliability ensemble averaging method for producing probabilistic climate-change projections, *Climate research*, **41**(1), 61.

Zhang, M., W. Lin, C. B. Bretherton, J. J. Hack, and P. J. Rasch, 2003: A modified formulation of fractional stratiform condensation rate in the NCAR Community Atmosphere Model (CAM2), *J. Geophys. Res.*, **108**, 4035, doi:10.1029/2002JD002523.

Zhang, M., and N. A. McFarlane, 1995: Sensitivity of climate simulations to the parameterization of cumulus convection in the Canadian Climate Centre general circulation model, *Atmos.-Ocean*, **33**, 407−446.

Zhu, Y., and R. E. Newell, 1998: A proposed algorithm for moisture fluxes from atmospheric rivers, *Mon. Wea. Rev.*, **126**, 725−735.